SAPIENZA
UNIVERSITÀ DI ROMA

Carrier dynamics in semiconductor nanowires

Università di Roma "La Sapienza"
Dipartimento di Fisica
Dottorato di Ricerca in Fisica- XXXIII cycle

Candidate

Aswathi Kanjampurath Sivan
Matricola 1820387

Thesis Advisors

Dr. Faustino Martelli
Prof. Antonio Polimeni

A thesis submitted in partial fulfillment of the requirements for the degree of Doctor of Philisophy in Phyiscs

Academic year-2019/20

“പണ്ടു പണ്ടു് ഓന്തുകൾക്കും ദിനോസറുകൾക്കും മുൻപ് ഒരു സായാഹ്നത്തിൽ രണ്ടു ജീവബിന്ദുക്കൾ നടക്കാനിറങ്ങി. അസ്തമയത്തിലാറാടിനിന്ന ഒരു താഴ്‌വരയിലെത്തി. ഇതിന്റെ അപ്പുറം കാണണ്ടേ? ചെറിയ ബിന്ദു വലിയതിനോട് ചോദിച്ചു. പച്ചപിടിച്ച താഴ്‌വര, ഏട്ടത്തി പറഞ്ഞു. ഞാനിവിടെ തന്നെ നിൽക്കട്ടെ. എനിക്കു പോകണം, അനുജത്തി പറഞ്ഞു.”

- *ഖസാക്കിന്റെ ഇതിഹാസം*

Abstract

This Ph.D. thesis presents results on the ultrafast spectroscopy of semiconductor nanowires with the aim of studying the carrier dynamics in these quasi-one-dimensional nanostructures. Six different semiconductor nanowire systems were studied using optical measurement techniques in the span of the last three (2017-2020) years and their results are discussed here.

Fast transient absorption spectroscopy with a femtosecond laser source was the primary experimental technique used throughout this thesis. With the use of a femtosecond laser system, the time evolution of photoexcited carriers in the nanowire structures was probed, giving insights into several fundamental physical phenomena of the photoexcited carriers. Several other optical measurement techniques such as photoluminescence, cathodoluminescence, Raman spectroscopy and UV-Vis steady state spectroscopy were also used.

The first material investigated for this thesis was Si nanowires grown through plasma-enhanced chemical vapor deposition. These nanowires were grown on a transparent quartz substrate, and the as-grown samples were used for studying the optical response to light excitation using a femtosecond laser with energy less than the direct bandgap (3.3 eV) energy of Si. Even when excited below the direct bandgap energy, an absorption signal was observed at 3.3 eV in the transient absorption measurements. By comparing the results obtained in this thesis with those obtained by the excitation above the direct bandgap energy, this work enabled me to disentangle the electron and hole dynamics with respect to the direct bandgap transition in Si.

The second material under study was InP nanowires. InP nanowires of both zincblende and wurtzite structures were studied using ultrafast transient absorption spectroscopy. The samples were probed both in the visible and in the near infrared (NIR) spectral region. The changes in the band structure due to the changes in the crystal structure were observed in the form of different energy transitions in different crystal structures. The transient absorption response was systematically studied to understand both the spectral and the kinetic properties of these electronic transitions. Carrier temperature of photoexcited carriers as a function of delay times were also extracted for the highest energy transition in the wurtzite InP with the help of these measurements. The energy loss rate by the hot carriers were also calculated as a function of carrier temperature giving insights into the occurrence of a phonon-bottleneck.

The third material under study was GaAs nanowires. This short study investigated the photoinduced changes in the visible spectral region. This study was done with a high pump energy with the aim of observing the two critical points in the band structure of GaAs namely, E1 and E1 + Δ. The most common experimental technique to observe the critical points is ellipsometric studies, however, in this thesis their observation using ultrafast spectroscopic techniques are presented.

The NWs of ternary alloy semiconductor GaAsP, with about 20 % phosphide and 80% arsenide content were studied next. This study was aimed at investigating the rate of hot carrier cooling as a function of the diameter of the nanowires after photoexcitation using an ultrafast laser pulse. Carrier temperatures and energy loss rates were extracted from the analysis of the transient absorption spectra. The experimental data provided direct evidence that nanowires

with smaller diameter sustain higher carrier temperatures compared to nanowires with larger diameter for longer periods of time.

The fifth system under study was ZnSe nanowires decorated with Ag-nanoparticles. This study was aimed at understanding the modifications in the optical properties and carrier dynamics of ZnSe nanowires when Ag plasmonic nanoparticles were deposited on their sidewalls. Ag-nanoparticles were deposited on the sidewalls of ZnSe nanowires through thermal dewetting, creating a physical contact between the metal and the semiconductor. The energy of the local surface plasma resonance of these nanoparticles was very close to the optical bandgap of ZnSe nanowires. Low temperature photoluminescence measurements showed significant changes in the line shape of donor acceptor pair bands of ZnSe, with enhanced phonon replicas in the presence of Ag-nanoparticles. Ultrafast spectroscopic measurements showed changes in the rise time and decay time of transient absorption signal in the presence of Ag-nanoparticles. As a comparison, ZnSe nanowires were also decorated with Au-nanoparticles, in which case there was no overlap between the energy of local surface plasmon resonance of Au-nanoparticles and the optical bandgap of ZnSe nanowires. In this latter case there were no significant changes in the optical properties of ZnSe. This comparison enabled us to understand the importance of resonant interactions between plasmonic nanoparticles and semiconductor nanowires.

The final section of this thesis presents doping induced changes in the optoelectronic properties of ZnO nanorods. ZnO nanorods were synthesized using a cheap, and scalable seed mediated chemical bath deposition method. Doping with cobalt was done simultaneously by introducing Co^{2+} ions in the growth solution and the doping concentration was determined by the amount of Co^{2+} introduced in the growth solution. Co-doped ZnO nanorods were prepared in order to study their usability as a photoanode material for photoelectrochemical water splitting. Through cathodoluminescence and ultrafast spectroscopic measurements, the improvements in the optoelectronic properties of Co-doped ZnO nanorods were explored. All the measurements pointed to the formation of more surface defects in the presence of Co-doping and their role in the modification of the optoelectronic properties of the nanorods. These were then characterized using photoelectrochemical measurements such as incident photon to current efficiency and voltammetry measurements to quantify photogenerated current density. This allowed the determination of the ideal value of Co^{2+} in growth solution for photoelectrochemical applications, which was found to be 1%. These nanorods were further improved by functionalizing their surfaces with a metal organic framework, the zeolitic imidazolate framework – 8 (ZIF-8). Further optical characterization of these ZIF-8 coated Co-doped ZnO nanorods were also discussed, demonstrating further improvement in photoelectrochemical performance.

Acknowledgement

The last three years that constituted the duration of my Ph.D. have influenced my life in incredible ways, both academically and otherwise. And it was made possible only with the help of the exceptional people I met on the way. I take this opportunity to express my heartfelt gratitude to all of them. However, some of them deserve a special thank you for going that extra mile to help me.

My thesis would not have been possible if not for my advisor, Dr. Faustino Martelli, who is not only an outstanding scientist and scholar, but also an excellent mentor. He has been kind, tenacious and prompt in guiding my research, and above all showed me the importance of brevity and precision, though I still have a lot more to learn from him. He has shown me the need for excitement and optimism in the lab even after a long day of failed experiments, and the importance of Occam's razor in the life of an experimentalist. If not for his kind support during these testing times, the completion of thesis would not have been possible in a timely manner. He also helped me navigate the complicated bureaucracy in Italy when I first arrived, this alone requires a whole page of acknowledgement. For all this and more, I am extremely grateful.

I take this opportunity to thank all the members of the EuroFEL Support Laboratory for constantly helping and guiding me. I want to thank Dr. Lorenzo Di Mario for his patient guidance, and support during the initial year of my PhD. He taught me how to use several equipment in the lab and in the cleanroom. He has been an excellent partner in the lab, and a meticulous experimentalist. I am deeply indebted to Stefano Turchini for all the help he has provided me since the very first day I arrived in Rome. He has been a great source of emotional support during the good and the bad days. I also thank him and his family from the bottom of my heart for providing me a place to stay when I first arrived in Rome, and for helping me navigate this city. I thank Dr. Daniele Catone, Dr. Patrick O'Keef, Dr. Alessandra Paladini and Dr. Francesco Toschi for lending me their expertise in the field of femtosecond spectroscopy. I want to thank Dr. Lin Tian even though I have never had the opportunity to meet her in person. She finished her Ph.D. before me, but made sure that I had all the information required to start my research career in Italy as a non-European citizen. She gave me detailed explanations on how to apply for the residence permit, healthcare card, etc. The google document she shared with me about the documents I need in Italy still serves as a guidance to me. Also, she prepared and studied the Si NWs in detail so I could carry the work forward.

I also thank Prof. Antonio Polimeni for agreeing to be my supervisor at the Sapienza university for this PhD course, and for helping start the collaborative work on the InP nanowires. And a special thanks to Prof. Lara Benfatto for her resourceful lectures and for being my referente nel collegio docenti at Sapienza.

I have had the opportunity to work within a stimulating research network, thanks to the Horizon 2020 MSCA Innovative Training Network, INDEED. It provided me the opportunity to collaborate with several research groups. I want to thank Alejandro Galan for being an excellent collaborator, and a great friend. I hope to continue our friendship well beyond the timeframe of this network. I also want to thank Prof. Anna Fontcuberta I Morral for giving me the opportunity to carry out my research secondment in her laboratory at EPFL, this was a great

learning opportunity for me, I experienced the wonders of working within a large international group, that is diverse in so many ways. I hank Nicolas Tappy for patiently teaching me how to operate the Cathodoluminescence equipment, and the helium transfer lines. I take this moment to thank Dr. Silvia Rubini for sending me numerous nanowire samples over the last three years. I also want to extend my acknowledgement to my fellow ESRs at INDEED for the fun times. I thank Dr. Aruni Foneska for providing me InP NW samples, and for being readily available for discussions in person and by email. I also thank Dr Yunyan Zhang for the GaAsP NWs. and Dr. Alessia Irrera for sending me the ultrathin Si NWs.

I want to thank all the wonderful staff at IMM who made me feel welcome, and in particular, my wonderful officemates; Dr. Francesco Maita for answering my numerous questions and helping troubleshoot my technical woes, Dr. Sabrina Calvi for being a good friend and sharing her PhD wisdom and Dr. Alessandro Pecora for his optimism.

I am grateful for my wonderful family, who have been the wind at my back. I thank them for constantly supporting me despite being far away during these years, I miss them deeply. I want to take a moment to thank all the wonderful friends I have made during the last three years for being a source of constant support. I remember the first meeting at the university for the new PhD students, and thank you to Guilherme Raposo for starting the first conversation with me at Sapienza. I value our friendship and hope that it will survive the many years to come.

Last but not the least, I thank my partner, Juan Francisco for coming into my life unexpectedly, and for being a constant source of positivity, love, and encouragement. Thank you for being patient with me, and with my quirks. The last 8 months of this year have been extremely difficult, and stressful due to the ongoing global CoVid-19 pandemic, and the two months in lockdown far away from family and friends would have driven me insane if not for you. I hope you understand that it was the comfort you provided that made me feel at home here, and for this I am grateful.

Contents

Chapter 1 Introduction 4

1.1 Semiconductor nanowires 4

1.1.1 The global climate crisis and how nanowires can help us 6

1.2 Need for characterization 8

1.3 Types of characterizations 9

1.3.1 Structural characterization 9

1.3.2 Electrical characterization 9

1.3.3 Optical characterization 10

1.4 Ultrafast spectroscopy of semiconductors 12

1.4.1 Hot carriers 14

1.5 Systems under study 18

1.5.1 Silicon nanowires 18

1.5.2 Group III-V semiconductor nanowires 19

1.5.3 ZnSe nanowires decorated with metal nanoparticles 20

1.5.4 Cobalt-doped ZnO nanowires 20

Chapter 2 Experimental techniques 21

2.1 Fast Transient Absorption Spectroscopy 21

2.2 UV – Visible Spectroscopy 26

2.3 Steady state and time resolved photoluminescence 26

2.4 Cathodoluminescence 28

2.5 Raman Spectroscopy 29

2.6 Thermal Evaporation 30

2.7 Sample preparation 31

Chapter 3 Carrier dynamics in silicon nanowires 32

3.1 Introduction 32

3.2 Material 34

3.3 Optical characterization 35

3.4 Results...35

3.4.1 Ultrafast spectroscopy of In-seeded Si NWs 35

3.4.2 Optical characterization of ultrathin Si NWs..41

3.5 Conclusions..43

Chapter 4 Ultrafast spectroscopy of group III-V nanowires 45

4.1 Ultrafast spectroscopy of indium phosphide nanowires 45

4.1.1 Material...47

4.1.2 Optical characterization 48

4.1.2.1 Micro PL on InP NWs 48

4.1.2.2 Fast transient absorption spectroscopy in the NIR 49

4.1.2.3 Fast transient absorption in the visible region of the spectrum 54

4.1.3 Discussion...59

4.2 Ultrafast spectroscopy of GaAs using a visible probe...62

4.2.1 Material...63

4.2.2 Optical characterization 63

4.2.2.1 FTAS of ZB GaAs NWs using a visible probe..63

4.2.3 Discussion...66

4.3 Diameter dependent carrier cooling in GaAsP nanowires...67

4.3.1 Material...68

4.3.2 Optical characterization 68

4.3.2.1 Photoluminescence of the GaAsP NWs..68

4.3.2.2 Raman measurements 69

4.3.2.3 Fast transient absorption of GaAsP NWs at 77 K...70

4.3.3 Discussion 74
4.4 Conclusion 75
Chapter 5 Functionalized nanowires 77
5.1 ZnSe nanowires decorated with plasmonic nanoparticles 5.1.1 Introduction 77
5.1.2 Material 80
5.1.3 Optical characterization 81
5.1.4 Results 82
5.1.5 Discussion 95
5.2 Cobalt doped ZnO nanorods 97
5.2.1 Introduction 97
5.2.2 Material 98
5.2.3 Optical characterization 100
5.2.4 Results 100
5.2.5 Metal organic framework functionalized Co-doped ZnO nanorods 108
5.2.6 Discussion 113
5.3 Conclusions 116
Chapter 6 Conclusions and Outlook 117
List of Publications 119
Appendix A 120
Optical measurements 120
A.1 Optical parametric amplifier 120
A.2. Transmittance and Reflectance of Si NWs 122
Bibliography 123

Chapter 1 Introduction

Semiconductor nanowires (NWs) form a relatively new, yet well established, family of material structures. They are tiny rod-like structures with a high surface area to volume ratio, typically having few nanometers to few hundreds of nanometers in diameter and several hundreds of nanometers to several micrometers in length. In the first chapter of this thesis, a brief introduction to semiconductor NWs followed by a brief introduction to ultrafast carrier dynamics in semiconductors are given.

1.1 Semiconductor nanowires

The first form of semiconductor NW-like structure was observed by Wagner and Ellis in 1964 in the form of silicon whiskers through a new method of crystal growth from vapor precursors, which they called vapor-liquid-solid (VLS) growth mechanism.[1] In their novel work, the authors grew Si whiskers using a metal impurity(catalyst), gold in their particular case. Au droplets were heated at 950ºC on the surface of Si substrate forming an Au-Si alloy in liquid phase, then a precursor gas containing Si was introduced to this system. Si atoms in the precursor gas enter the alloy droplet, supersaturate the Au-Si alloy, and precipitate, displacing the liquid alloy from the substrate surface. This process continues and Si whiskers grow until all the Au is consumed or until the growth conditions are changed. In their paper, the VLS mechanism yielded Si whiskers with diameters in the micrometer range. VLS remains to this date a prominent technique for NW growth. Figure 1.1 shows the VLS growth schematic of semiconductor NWs using Au catalyst. In the following years, several strides have been made towards growing NWs of different sizes, crystal structures, and tunable properties.[2–7] The main push towards the development of NW-based research comes after the growth of III-V NWs by metal-organic vapor phase epitaxy in the early 1990s.[8–10] Finally, by the late 1990s, NWs became a hot topic of research within the material science and nanotechnology community.[11,12] NW growth techniques have also allowed the possibility of having semiconductor heterostructures with two or more materials growing on top of each other.[13,14] NWs form heterostructures either with the substrate, meaning the NW and substrate are two different materials or as axial or radial heterostructures. In axial NW heterostructures, different materials are inserted or grown along the direction of the growth axis[15], while radial heterostructures form core-shell like structures[16]. Heterostructures have an important application in bandgap tuning and surface passivation, as well as in the creation of axial and radial quantum dots in NWs.[17]

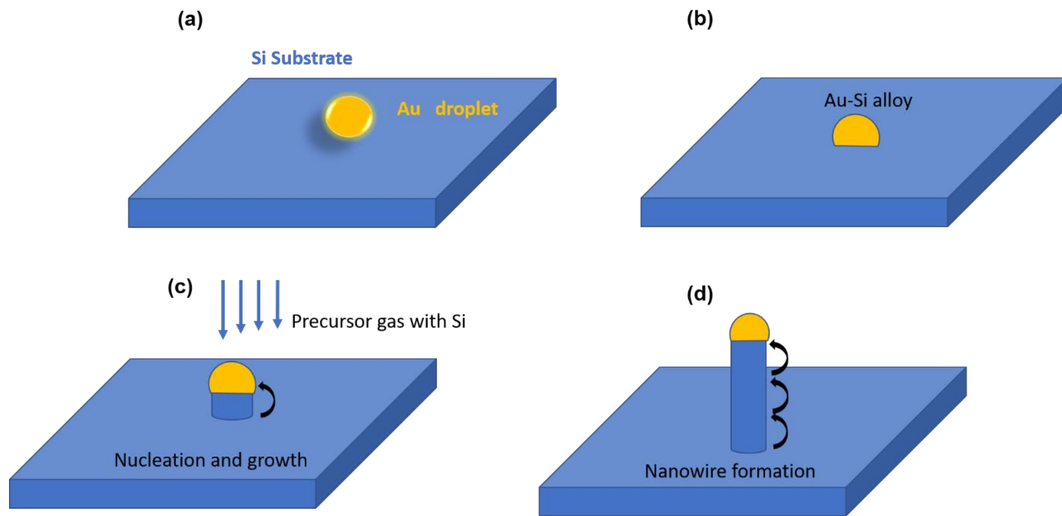

Figure 1. 1. The schematic corresponding to the VLS growth of a Si NW starting with (a) a clean Si substrate with gold droplet deposited on it (b) which forms Au-Si alloy upon application of heat, (c) followed by introduction of precursor gases containing Si, during which the Si in vapor phase enters the Au-Si alloy leading to nucleation and growth, displacing liquid alloy from the substate surface, and (d) finally forming the long NW structure.

An important aspect, with technological consequences, is that the small size of the NW in contact with the substrate allows for efficient strain relaxation enabling growth on lattice-mismatched substrates, which is difficult in the case of thin films.[18–20] Semiconductor NWs can also be doped using different impurities to control the minority (majority) carrier type, conductivity, and optical bandgap. In-situ doping of NWs can be done during the growth of the NWs by introducing impurities during the growth.[21] A thorough study on the doping of semiconductor NWs can be found in the doctoral thesis of J Wallentin.[22] All these interesting properties make NWs an important topic of research both in the field of technological applications as well as to study new physics concerning the 1D structure. Figure 1.2 shows the data obtained from the ISI web of science search engine using the keyword “nanowires”; it shows the tremendous growth in NW research in the last couple of decades.

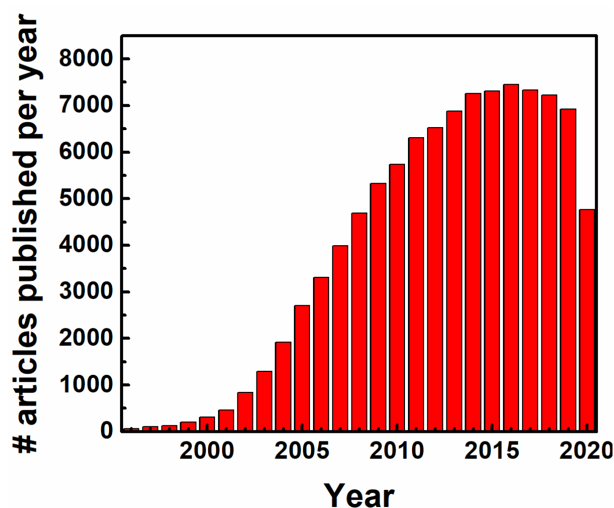

Figure 1. 2.Number of publications on NW topics from 1995-2020 (Source of data: ISI web of science, keyword-"nanowires").

Another characteristic feature of semiconductor NWs is the existence of crystal structure polytypism.[23] Polytypism is defined as " *a variant of polymorphism in which only periodicity along growth axis varies from one polytype to another leading to different crystal structures due to different unit cell extensions in the direction perpendicular to growth plane in which the periodicity (unit cell extension) is the same for all polytypes."*[24] Semiconductors, belonging to group III-V, except nitrides, crystalize in the zinc blende (ZB) structure in bulk. However, when grown as NWs, they offer the possibility to exist also in the wurtzite crystal phase (WZ). Achieving different crystal phases is possible by changing the growth conditions. Polytypism has significant implications on the electronic and optoelectronic properties of the material.

To truly understand the motivation behind studying NWs, a few problems faced by the current society and how NWs may be of help are discussed below:

1.1.1 The global climate crisis and how nanowires can help us

On the walls of the Metronome in Manhattan, USA there was a 15-digit electronic clock that showed the critical window for action to prevent the irreversible effects of global warming. This was installed by two artists Gan Golan and Andrew Boyd between the 19th to the 27th of September 2020. The time of this clock was updated based on calculations by the Mercator Research Institute on Global Commons and Climate Change at Berlin.[25] As of 19th September 2020, there are about 7 years and 103 days remaining on this clock for us to take some solid actions against global warming. This Institute in Berlin also showcases the carbon clock on their website showing the time left until the CO_2 budget is depleted. The carbon budget refers to the amount of CO_2 the atmosphere can absorb if we want to limit global warming by 1.5 ^{0}C or 2 ^{0}C. As of 2018, the carbon budget we have in order to remain within the 1.5 ^{0}C limit was 9 years, and to remain within the 2^{0}C rise was 26 years.[26] So, it seems like the right time,

perhaps even a bit late, to find solutions to avoid the exhaustion of the carbon budget. And to do so, both political and technological strides must be made in the right direction. As scientists, we can work on improving the energy efficiency of existing technologies, as well as bring out new energy sources. This is where NWs might help us; in photovoltaics, hydrogen fuel economy, and energy storage.

Nanowire based solar cells

Solar energy is one of the most abundant and versatile forms of energy that is available on earth. However, due to limitations in the technology, only a small fraction of it is being used. As of 2018, around 505 GW of electricity was produced by solar photovoltaics, fulfilling a little more than 2% of the global electricity consumption. Figure 1.3 shows the renewable energy generation in the world as a function of time, obtained from *Our world in data*.[27] Si solar cells based on a single p-n junction supply to the major solar energy demands in the world currently. Si solar panels can be expensive due to large material demands and can have energy losses due to fast carrier thermalization, and the inability to absorb all the photons, reflection, and non-radiative recombination of energetic carriers. This is where NWs could be of help.

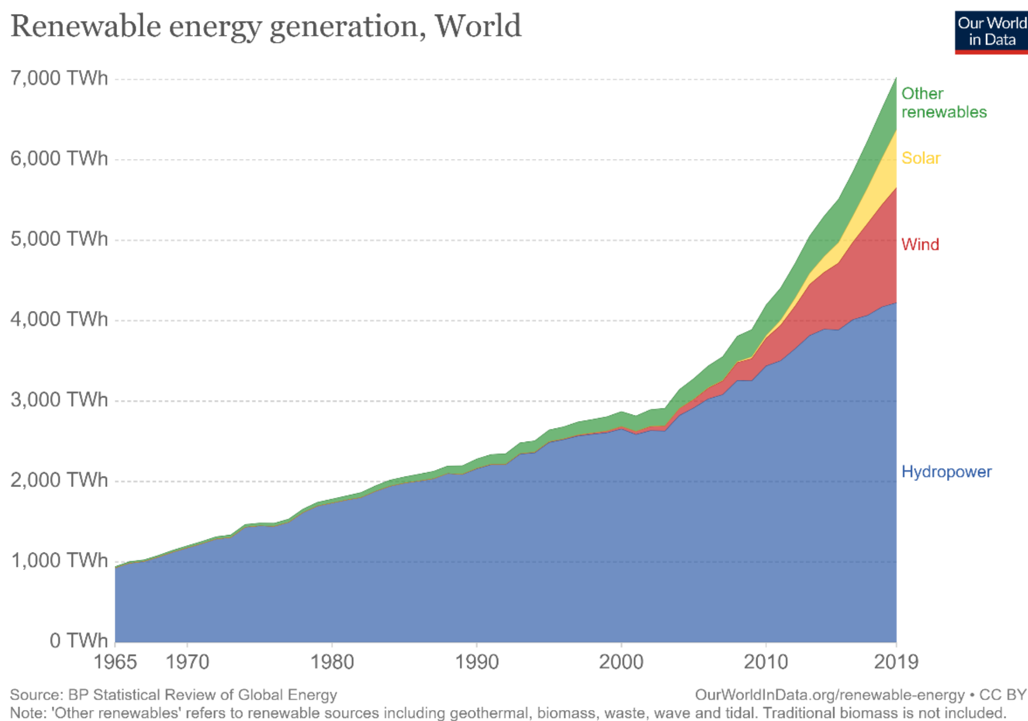

Figure 1. 3. Chart showing breakdown of the renewable energy sources by their individual components over the years until 2019. As of 2019, Solar energy produced a total of 724.09 TWh.

The high surface area to volume ratio of NWs provides more photosensitive area for the same amount of material as compared to the thin film geometry. The versatile nature of NWs also helps to tune the bandgap and control the light absorption and scattering depending upon the dimension of the NWs.[28–30]Solar cell devices based on GaAs NWs have shown promising results in work done by Krogstrup *et al.*[31] Similarly, InP NW based solar cells have also shown promising improvements.[32]

A more efficient type of solar cell is called Tandem solar cells, in which different materials with a range of bandgaps are stacked on top of each other. This helps efficient light absorption in different parts of the solar spectrum with the help of different bandgap materials. Such multijunction solar cells have shown efficiencies of about 38.8%.[33] A problem in building tandem solar cells lies with the difficulty in growing materials on lattice-mismatched substrates. NW arrays can provide a solution here because of the ease with which NW based heterostructures can be grown.[34]

Photoelectrochemical water splitting for hydrogen fuel production

Hydrogen fuel created by splitting water using solar energy is a zero-carbon energy source. Though this will provide a great opportunity to help reduce greenhouse gas emissions, the efficiency of hydrogen production from solar energy has been quite low. Recently, some promising results have been displayed by nanowire-based photoelectrochemical water splitting electrodes. The large surface area to volume ratio provides more photon absorption as well as benefits through better carrier separation. Erik Bakker's group at Eindhoven University have developed GaP NW based photocathodes.[35] Photocathodes utilizing InP NWs with an efficiency of 6.4% have been demonstrated by Lu Gao *et al.*[36] Similarly, several photoanodes with encouraging results based on NW structures have been developed recently. The main materials used in this case are TiO_2 and ZnO. A detailed study of the optical properties of ZnO nanorods for photoanode applications is presented in chapter 5 of this thesis.

1.2 Need for characterization

NWs are becoming an important component in nanoelectronics device fabrication. Their unique structure allows NWs to exhibit several novel electronic, magnetic, optical, and thermal properties.[31,37,38] For example, as the diameter of the NW reduces, the thermal conductivity of the NW decreases.[39,40] NWs are being heavily researched for applications in solar cells,[31,32,41,42] photoelectrochemical water splitting for hydrogen fuel,[43–45] biosensors,[46] field-effect transistors[47] and several other nano-electronic devices. Perhaps one of the most interesting applications of NWs is their integration into nanophotonic devices. To integrate NWs into devices reliably, their properties must be thoroughly studied and understood. It is important not only to grow NWs efficiently but also to learn the basic physics that govern their fundamental properties. Carrier confinement, carrier concentration, the density of states, electronic band structure, carrier dynamics, optical absorption, light emission, etc. are some of the basic

properties that must be experimentally and theoretically studied before designing devices with the NWs. Apart from being a technologically versatile material system, NWs also provide an interesting setting to study several new and interesting physics. They are an ideal system to study how fundamental physics changes with size and dimensionality. Reliable characterization is therefore necessary for understanding the fundamental properties of these quasi-one-dimensional structures.

In this thesis, the optical properties of different semiconductor NWs are studied to understand their fundamental properties and to optimize them for device fabrication.

1.3 Types of characterizations

Various characterization techniques are required to optimize the growth of NWs and to control their properties. Characterization techniques also help to find out any possible defects as well as problems with the produced NWs. The following sections show some of the characterization techniques for NWs.

1.3.1 Structural characterization

To assess the quality of the NWs grown, two aspects must be characterized: electronic properties and structural properties. These two are closely connected to the growth parameters used. Out of the two, the structural properties are usually investigated first. As mentioned above, NW structures can show crystal structures different from the bulk depending upon the growth parameters. Another important aspect to be investigated through structural characterization is the presence of defects. Defect densities play an important role in determining the crystal quality, carrier concentration, and bandgap modification. Electron microscopies and X-ray diffraction techniques are commonly used to characterize the structural properties of NWs. The two common forms of electron microscopies are scanning electron microscopy (SEM) and transmission electron microscopy (TEM). SEM scans provide a resolution of about 1-10 nm while TEM scans can provide atomic resolution. Raman scattering is another very powerful tool to carry out the structural characterization of NWs. It is a non-destructive characterization technique that can give information on lattice strain, structural composition, phonon dispersion, etc.

1.3.2 Electrical characterization

The electronic properties of the NWs can be studied either through electrical characterizations or through optical studies. For electrical characterization, electrical contacts are required for the measurements. The most common method to perform this measurement is to remove the NW from the substrate, place it horizontally on an insulating substrate, and then connect

contacts on both ends of the NW. The contacts can be made using electron beam lithography. The conductivity is then measured by monitoring the current produced by sweeping with a source-drain voltage. Just as an example, Cui *et al.* have performed electrical transport in Si NWs using this method.[48] However, preparing ideal contacts for these kinds of measurements can be challenging at times, and the contact resistance will have to be decoupled from the measurements.[39] A way to reduce this problem is by using a 4-probe measurement in place of the 2-probe set-ups. For example, C. Thelander *et al.* have used a 4-probe method to accurately measure the resistivity of InAs NWs.[49] Figure 1.4 adapted from C. Thelander *et al.* shows a 4-probe measurement setup on an electrically contacted InAs NW.

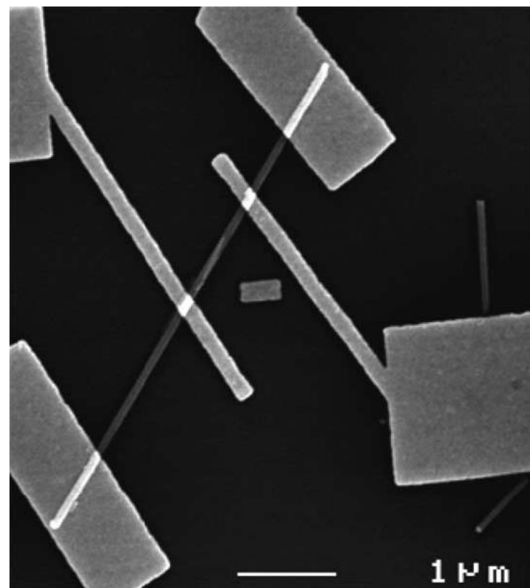

Figure 1. 4. A 4-probe electrical measurement setup on an InAs NW. Reprinted from C. Thelander et al [49], Copyright (2004) with permission from the Elsevier.

1.3.3 Optical characterization

Optical measurements constitute the non-destructive characterization techniques requiring comparatively less sample preparation. Since NW based solar cells and photonic devices are at the centre of NW research, it is necessary to understand their response to light excitation. The most common method of optical characterization is photoluminescence (PL).

1.3.3.1 Photoluminescence measurements

Steady-state and time-resolved (TR) PL can provide information about optical bandgap as well as carrier recombination times of materials. In PL the NWs are excited using a laser source

leading to the optical absorption of the photons by the carriers in the NW sample. The light emitted by the sample when the photoexcited carriers recombine is collected and analyzed. This gives information about the bandgap, the recombination mechanism, the presence of defects, etc. Through PL measurements, the steady-state of the semiconductor system is studied while TRPL measurements give information about the recombination rates. Depending on the band structure of the material, the PL efficiency varies. In a direct bandgap semiconductor, the valence band maxima and conduction band minima are at k= 0, while this is not the case in an indirect bandgap material. Therefore, in an indirect bandgap material the photon absorption leading to excitation of the electron to conduction band and recombination back to valence band are mediated by phonons because of momentum conservation rules. Hence, a direct bandgap material produces stronger and more efficient PL compared to an indirect bandgap semiconductor. Figure 1.5 shows the recombination process of carriers in the two cases.

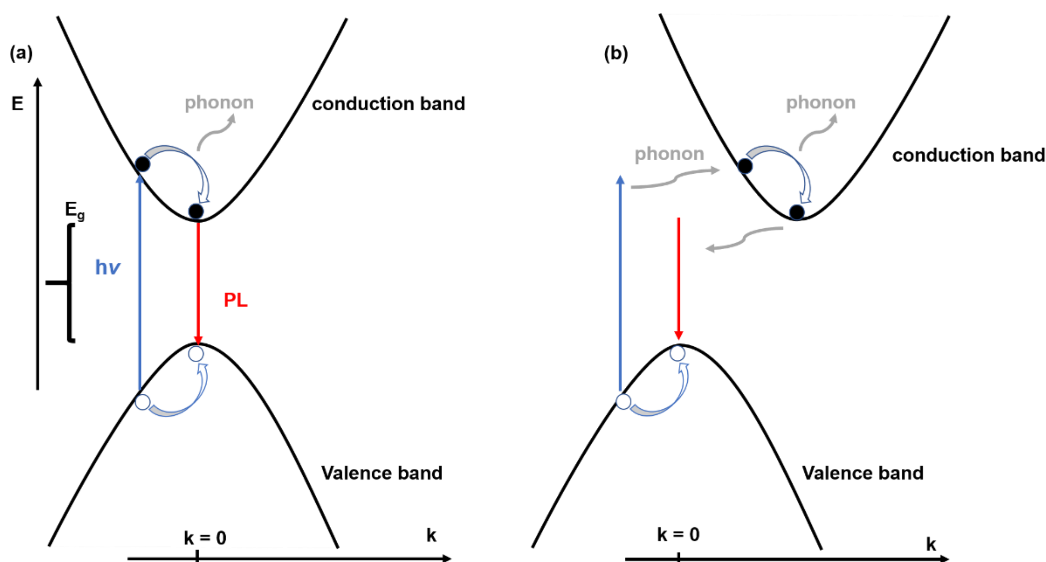

Figure 1. 5. Schematic diagram showing (a) direct bandgap and (b) indirect bandgap semiconductor with parabolic band structures. After absorption of a photon with energy greater than bandgap energy (blue arrow), excited carriers are created which thermalize to band edge by phonon emission (grey curly arrows). The red arrow shows the radiative recombination. For indirect bandgap, the absorption and emission are assisted by phonons.

The lifetime of a carrier is defined as the average time taken by the minority charge carriers to recombine after excitation. This quantity is dependent on the crystalline quality of the material, doping levels present, and other defects. The recombination process can be either radiative or non-radiative. The carrier lifetime can be expressed as,

$$\frac{1}{\tau} = \frac{1}{\tau_r} + \frac{1}{\tau_{nr}} \qquad (1.1)$$

where τ, τ_r, τ_{nr} are the average, radiative and non-radiative recombination lifetimes, respectively.

Depending on which component is the shortest, the most probable recombination method is determined. Non-radiative recombination can be further divided into (i) Auger recombination; (ii) defect mediated recombination, and (iii) surface recombination. Through TRPL measurements one can study the recombination lifetime of carriers in a material. This quantity is important in the functioning of light emitting devices, and hence it is crucial to know this value while choosing materials to design these devices.

Other common methods of optical characterizations include absorption, transmission, and reflection spectroscopies. With the advances in ultrafast laser systems, it has been possible to excite the NWs using ultrashort laser pulses and to probe the photoexcited sample with a precision of tens of femtoseconds or in some cases even attoseconds. Ultrafast spectroscopy of semiconductor NWs involves exciting the NWs using a pump laser with energy near or above the bandgap of the semiconductor. This photoexcited sample is then probed with a probe pulse at different time delays from pump excitation.

This thesis mainly focuses on the ultrafast spectroscopy of different semiconductor NW systems such as Si, InP, GaAs, and GaAsP NWs. ZnSe NWs functionalized with plasmonic nanoparticles (NPs) and cobalt doped ZnO nanorods (NRs) are also studied in detail. The motivations for studying those materials and material systems are given below.

1.4 Ultrafast spectroscopy of semiconductors

The development of ultrashort laser systems in the 7'0s began a paradigm shift in the optical characterization of materials. With the onset of ultrafast spectroscopic techniques, a whole regime of previously unexplored photoexcited carrier interactions came to the spotlight. Information regarding carrier dynamics, such as carrier-carrier interaction and carrier-phonon interaction is of extreme importance in device designing using NWs. This thesis deals with the ultrafast transient absorption (TA) spectroscopy in the pump-probe configuration. The detailed experimental setup is explained in Chapter 2. In TA spectroscopy, a pump pulse is incident on a small area on the sample. The interaction of the sample with pump pulse causes absorption, emission, transmission, reflection, and scattering of the photons. In the TA measurements, the significant processes are absorption, thermalization, and emission. After pump excitation, the probe light is incident on the same spot of the sample at different time delays, and by monitoring the pump induced changes in the absorption of the probe by the sample, information about photoexcited carriers is gathered. In this experiment, a quantity called differential absorbance of the probe light by the sample, ΔA is measured in milli OD. OD stands for optical density and is defined as the logarithmic ratio of the intensity of light incident on a material to the intensity of light transmitted by that material. It is a common unit used to measure the absorbance of a material. ΔA is obtained by measuring the intensity of the probe light transmitted through the sample with and without pump excitation. The absorbance A and the differential absorbance ΔA are defined as,

$$A = -\log(T) = -\log\left(\frac{I}{I_0}\right) \qquad (1.2)$$

$$\Delta A = -\log\left(\frac{\Delta T}{T} + 1\right) \qquad (1.3)$$

where I and I_0 are transmitted probe intensity with and without pump excitation, respectively.

In an unperturbed semiconductor system, carriers and phonons remain in thermal equilibrium, with their average momentum equaling zero and average energy corresponding to the thermal energy of their common temperature. When an external force (field) is applied to the system, the carriers and phonons are perturbed. These perturbations lead to the excitation of carriers to higher energy states. The carriers at this stage can have energies much higher than the energy corresponding to the temperature of the lattice. Then through various scattering processes, the system relaxes to the equilibrium. In fast transient absorption spectroscopy (FTAS), after pump excitation, the electrons are excited from the valence band to the conduction band and the carrier dynamics of the photoexcited sample can be approximately divided into four temporally overlapping regimes:[50]

1. **Coherent regime**: This takes place within the first ~200 fs of the pump excitation. Several interesting phenomena such as carrier-carrier scattering, momentum scattering, and hole-optical phonon scattering take place in the coherent regime. The coherent phase follows immediately after pump excitation, where the carriers are still in phase with the electromagnetic wave that perturbed the system. This regime is of fundamental importance in the relaxation process of photoexcited carriers and manifests several quantum mechanical phenomena. As examples of work done on bulk semiconductor in this regime, I would like to point out the work of Q. T. Vu *et al.*[51]who have predicted an electron-plasmon quantum kinetics in bulk GaAs with 13 fs pulses at 300 K in this regime, and R. Huber *et al.*[52] who have used pump-probe terahertz spectroscopy to measure buildup time for phonon-plasmon coupling.

2. **Non-thermal regime**: This regime is within the first picosecond after the photoexcitation by the short pump pulse. Here the dephasing of the coherent regime takes place leading to a non-thermal distribution of photoexcited carriers. In this phase various scattering processes like carrier-carrier and carrier-phonon scatterings take place, taking the system to a thermal distribution of the carrier energy, that can be defined by a carrier temperature. This regime is governed mainly by Coulomb interactions.

3. **Hot-carrier regime**: This regime is between 1 ps – 100 ps. After the scattering processes in the non-thermal regime, the carriers redistribute their energies and form a thermal distribution that is defined by a carrier temperature (T_c). This temperature is usually higher than lattice temperature (T_L), and in the hot carrier regime, the carriers interact with phonons to cool down to the T_L. This process can lead to a buildup of a large non-equilibrium distribution of phonons. This regime concerns with the hot carrier-phonon interaction, decay of the optical phonons leading to the creation of acoustic phonons, carrier-acoustic phonon scattering, and intersubband scattering. Studying the hot carrier

regime is of extreme importance while designing devices such as solar cells where there is a need to sustain hot carriers for longer times.

4. **Isothermal regime**: This regime is after about 100 ps from pump excitation. At the end of the hot carrier regime, thermal equilibrium is established between carriers and phonons, and with the same temperature as the lattice temperature. At this stage, there is an excess of electron-hole pairs, which then recombines radiatively or non-radiatively. The recombination times can be studied using TRPL measurements. Recombination can also take place involving electrons or holes trapped by defect states. At high carrier densities, another kind of recombination is possible called Auger recombination. It involves two conduction band electrons such that when an electron in the conduction band and a hole in the valence band recombine, the energy of the recombination is transferred to another electron in the conduction band, and that electron gets excited to a higher energy state in the conduction band.

It is important to understand that many of these processes can temporally overlap. This work is mainly concerned with the hot carrier regime, and the isothermal regime. The hot carrier regime is of particular interest while studying NWs because depending on the kind of device one must design, the prolonged sustainability of hot carriers or faster cooling of them is desired. For example, in a photovoltaic device, some of the energy absorbed is lost through cooling of the hot carriers, and in this case, it is preferred to collect the hot carriers prior to their cooling.[53]

1.4.1 Hot carriers

After the non-thermal regime, various carrier-carrier scattering processes allow the energetic non-thermal carriers to achieve a common temperature T_c in few picoseconds after photoexcitation. These carriers are called hot carriers because their distribution function is defined by T_c, where $T_c>T_L$. In the hot carrier regime, the carrier-phonon and further carrier-carrier scatterings lead to the cooling down of hot carriers to the lattice temperature. By exciting the semiconductor with ultrashort pulses, and probing with a pulse at different time delays, cooling curves as a function of the time delay can be obtained. Throughout this thesis, in order to calculate the carrier temperature, a few assumptions are made: (i) parabolic band structure, (ii) Maxwell Boltzmann distribution for carriers whose $T_c>T_L$, and (iii) the density of states does not vary substantially within the analyzed region of the spectra. In order to give an example of what I am writing about, I report the work by M. B. Price *et al.,* who have shown carrier cooling in perovskites using TA measurements. Figure 1.6 taken from this work shows the determination of cooling curves through TA measurements.[54]

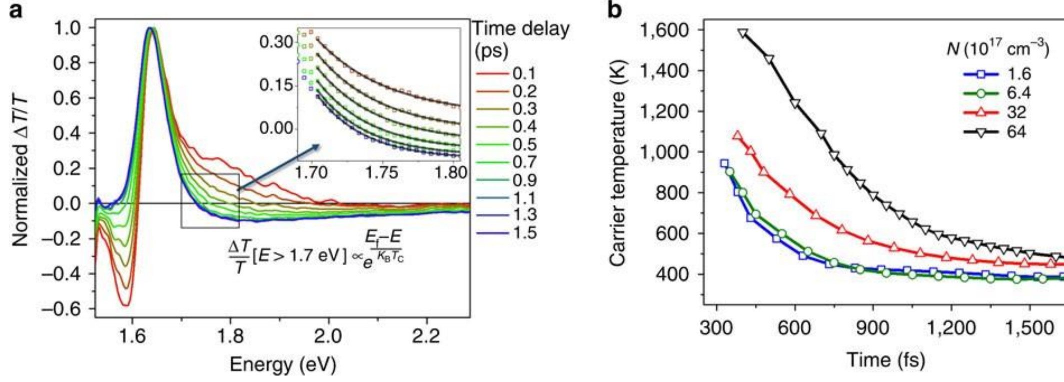

Figure 1. 6 Normalized TA spectra at different time delays for lead iodide perovskite, with inset showing fits to determine carrier temperature of the hot-carrier distribution; (b) Carrier temperature as a function of delay time for different carrier densities. Figure adapted from M. B. Price et al. [54] with permission from the publisher.

By fitting the high energy tail of the TA spectra with a Maxwell-Boltzmann distribution, one can find T_c at different delay times. In this way, the cooling curves as a function of time can be determined, and hence the rate of loss of energy in the hot-carrier regime can also be evaluated. For polar semiconductors, the energy loss is mainly due to interaction with optical phonons. The average rate of loss of energy is given by,[47]

$$< \frac{dE}{dt} > = (\frac{\hbar\omega_{LO}}{\tau_{LO}})\exp(\frac{-\hbar\omega_{LO}}{k_B T_C}) \tag{1.4}$$

where $\hbar\omega_{LO}$ is the LO phonon energy, τ_{LO} is the LO phonon scattering time and k_B is Boltzmann constant. $\frac{1}{\tau_{LO}}$ gives the scattering rate for the polar optical phonon. The value of this scattering rate for bulk semiconductors is given by,

$$\frac{1}{\tau_{LO}} = \frac{e^2\sqrt{2m\hbar\omega_{LO}}}{4\pi\hbar^2}(\frac{1}{\varepsilon_\infty} - \frac{1}{\varepsilon_0}) \tag{1.5}$$

where ε_∞ and ε_0 are the optical and static dielectric permittivity, respectively. By calculating carrier cooling rates in semiconductor NWs, we can have an idea about the phonon scattering times in different materials, as well as in NWs of same material with different sizes. This study has been carried out in this thesis for InP NWs and GaAsP NWs of two different diameters, as reported in Chapter 4.

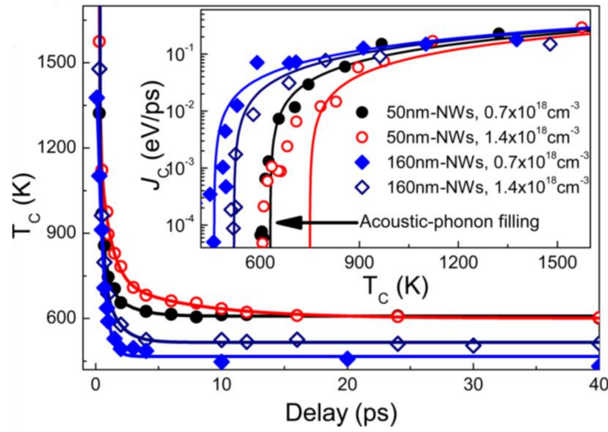

Figure 1. 7.T_C as a function of delay time for InP NWs of diameters 50 nm and 160 nm. Inset shows the rate of energy loss as a function of TC. The measurements are done for two different initial carrier densities. Adapted with permission from Yong et al. [55] Copyright (2013) American Chemical Society.

Carrier-phonon interactions are crucial for semiconductor-based devices. Several works have been carried out to measure carrier cooling rates in bulk and thin-film semiconductors. However, only a few reports have been made on the carrier cooling rates in semiconductor NWs. Yong *et al.*[55] have investigated the dynamics of hot carriers in InP NWs of WZ crystal structure with heavy ZB inclusions using transient luminescence and photoconductivity measurements. By approximating the high energy tail of transient PL of InP NWs with a Maxwell-Boltzmann distribution of the form proportional to $\exp(-E/(k_B T_c))$ they obtained T_c at different time delays for NWs of diameter 50 nm and 160 nm. It is worth mentioning that Yong et al [55] discuss their results in terms of stacking faults whose density depends on the NW diameter. They do not relate T_c and cooling rate directly to the diameter values. They find that T_c is greater for 50 nm NWs compared to 160 nm NWs. They conclude that the NWs with higher stacking defect density can sustain carriers at a higher temperature. Figure 1.7 adapted from their work shows T_c as a function of delay time, and the rate of energy loss as a function of T_c in the inset.

In Figure 1.7 the carrier cooling rates slow down on crossing 750 K. This is due to a phenomenon called phonon-bottleneck. Phonon bottleneck can be of two types, optical phonon bottleneck or acoustic phonon bottleneck. Photoexcited carriers in polar semiconductors lose energy through interaction with optical phonon modes. At high excitation intensities, the cooling rate of hot carriers can decrease due to the buildup of a non-equilibrium population of hot longitudinal optical (LO)-phonon modes in the Brillouin zone center. These hot phonons cannot equilibrate effectively fast, leading the carriers to reabsorb the phonons and reheat. This is called the LO-phonon bottleneck.[56] The LO-phonons that are produced in the initial part of carrier cooling further cools down by decaying into two counter-propagating longitudinal acoustic (LA)-phonons. At longer time delays, the cooling rates decrease significantly due to a non-equilibrium buildup of acoustic phonon modes by the decay of LO-phonons in the zone

center, called acoustic phonon-bottleneck.[57] The strong decrease after 750 K in Figure 1.7 is due to the acoustic-phonon bottleneck.

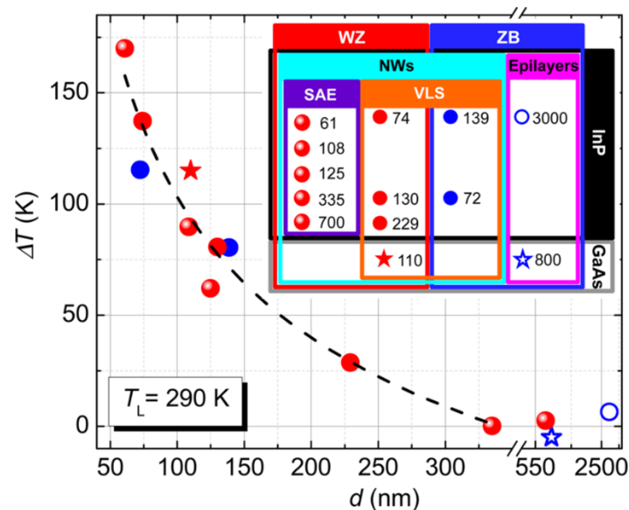

Figure 1. 8. $\Delta T = T_c - T_L$ as a function of diameter for InP and GaAs NWs grown by different mechanisms, as well as having different crystal structures. The inset shows diameters in nm for different samples. Adapted with permission from Tedeschi et al. [58]. Copyright (2016) American Chemical Society.

Tedeschi *et al.*[58] present another interesting work on the nature of long-lived hot carriers in III-V NWs. In their work, which has motivated my work on GaAsP NWs of different diameters, the authors have studied InP and GaAs NWs of ZB, WZ, and a mix of ZB and WZ crystal structure, with diameters varying from 61 nm to 700 nm. In that work, the authors use continuous-wave PL measurements to detect hot carriers, that thermalize at a higher temperature than the lattice temperature (T_L). They defined a quantity ΔT, where $\Delta T = T_C - T_L$, which increased with decreasing diameter independent of material, and morphology. Another observation was that in NWs with smaller diameters the hot carriers did not efficiently thermalize within few picoseconds. The peculiar aspect of their results was that the hot carriers were detected by steady-state PL measurements. The inefficient cooling down of hot carriers in thin NWs was attributed to the large-surface-to-volume ratio that prevents the cooling down of carriers to T_L via the emission of phonons. The sustained presence of hot carriers in thin NWs have significance for photovoltaics and thermoelectric applications. Figure 1.8 adapted from Tedeschi *et al.*[58] shows the difference of T_C extracted from PL spectra and T_L as a function of sample diameter.

Another important field where carrier-phonon interactions play a crucial role is in thermoelectric devices. So far, I have discussed optical measurements to study the scattering events involving phonons. Phonon scattering plays an important role also in the thermal

conductivity of NWs. Li and co-workers[40] have investigated the diameter dependent thermal transport in Si NWs. They have carried out experiments on Si NWs of varying diameters from 22 nm to 115 nm and observed that the thermal conductivity was about 2 order of magnitude lower than that of bulk Si and the thermal conductivity reduced as the NW diameter decreased. The changes are assigned to possible changes in the phonon-dispersion relation as well as due to increased phonon-confinement due to the small diameter of NWs leading to different boundary conditions for the phonon scattering events. Similarly, Swinkels *et al.*[39] report the diameter dependence of thermal conductivity of InAs NWs. They studied NWs with a range of diameters between 40-1500nm and found that the thermal conductivity reduced by 80% with respect to the bulk for a NW of 40 nm diameter.

In the following section of this chapter, a brief introduction to different materials studied in this thesis is given along with the motivation for their study.

1.5 Systems under study

NWs of different semiconductors were studied in this thesis with the common aim of understanding their response to light excitation. The first material under study is Si NWs, which is an indirect bandgap material. This is followed by ultrafast spectroscopy of NWs of group III-V, particularly InP, GaAs, and GaAsP. In the final chapter, two kinds of functionalization of semiconductor NWs are studied: (i) the effect of metal plasmonic NPs deposited on the sidewalls of ZnSe NWs, and (ii) Co-doped ZnO NWs.

1.5.1 Silicon nanowires

Si is an indirect bandgap semiconductor, with a bandgap value of about 1.1 eV and a direct bandgap of 3.3. eV. Si NWs were the first ones grown by VLS growth in 1964.[1] Si is a robust material for technological applications due to its abundance and low cost. To date, Si is the most widely used semiconductor in the world. The entire world of information technology revolves around the developments in the miniaturization of Si-based integrated circuits (ICs). These ICs pack several Si-based transistors in them. Following Moore's law[59], the number of transistors in an IC has been doubling roughly every two years. The size of the Si components has shrunk so much that now the technology is transitioning to the quantum realm. Hence, it is imperative to study Si in its quantum regime. Si is currently the leader in solar cell production in the world.[60] This demands a comprehensive study of the carrier dynamics in Si structures after photoexcitation.

The NWs used in this thesis are grown by plasma-enhanced chemical vapor deposition (PECVD). Chapter 3 deals with the ultrafast spectroscopy of Si NWs with a pump (2.34 eV) whose energy is lower than the direct bandgap energy of Si. After pump excitation, a white light supercontinuum probe in the visible region is used to study the changes induced by pump excitation near the direct bandgap transition. By comparing with the results of FTAS on Si NWs with pump energies above the direct bandgap energy, this thesis aims to disentangle the electron dynamics and hole dynamics. The diameters of the NWs grown by PECVD are too

large to observe any quantum effects. To study the effects of quantum confinement in NWs, experiments were planned on ultrathin Si NWs. However, due to the ongoing CoVid-19 crisis, this study has not been brought to its completion. Preliminary results on the ultrafast spectroscopy of ultrathin Si NWs with diameters less than 10 nm are presented. This final part is done as an introduction to the world of quantum confinement and related processes in ultrathin Si NWs.

1.5.2 Group III-V semiconductor nanowires

Chapter 4 deals with the ultrafast spectroscopy of group III-V semiconductor NWs. The first two materials: InP and GaAs are two widely studied direct bandgap semiconductors. Their thermodynamically stable crystal phase is ZB in the bulk state. However, in NW form they also crystallize in WZ state, impacting the optoelectronic properties. InP and GaAs are highly sought-after materials for photovoltaic materials. According to the efficiency curve calculated by Shockley and Queisser in1961 for the maximum light to electronic conversion efficiency for a single p-n junction solar cell, the bandgap of GaAs and InP falls in the energy range for maximum efficiency. Figure 1.9 taken from the work of Sven Rühle[61] shows the maximum efficiency according to Shockley-Queisser curve[62] as a function of bandgap energy, and one can see that InP and GaAs are ideal materials for photovoltaic applications. Figure 1.9 has a correction according to new data, where perovskites now show efficiencies > 25%.[33]

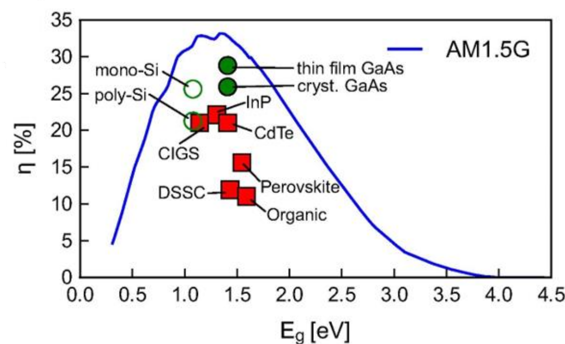

Figure 1. 9. Light to electric power conversion efficiency for a single p-n junction solar cell, when illuminated with 1.5 G irradiance as a function of bandgap. Reprinted from [61] Copyright (2016), with permission from Elsevier.

The final part of this chapter on III-V semiconductors deals with the study of hot carrier cooling in GaAsP NWs of different diameters. In this section, the rate of loss of energy by hot carriers in GaAsP NWs of different diameters is also deduced. This work is of particular interest because through ultrafast TA measurements, direct evidence for the diameter dependence of carrier cooling in NWs is observed. The novelty of this work is that it is done on NWs using an ultrafast TA spectroscopy that allows the determination of the scattering rates in NWs of

different materials and diameters. To obtain the results, the III-V NWs were transferred onto a transparent substrate, both by mechanical rubbing and by drop-casting with an organic solvent.

1.5.3 ZnSe nanowires decorated with metal nanoparticles

Chapter 5 is divided into two parts that deal with two different kinds of NW functionalization. The first part of the chapter studies the changes induced by Ag metal NPs on the optical properties and carrier dynamics of ZnSe NWs when deposited on its sidewalls. The local surface plasmon resonance (LSPR) of Ag NPs and the optical bandgap of ZnSe NWs overlap spectrally leading to resonant electronic interactions between the two. Low-temperature luminescence measurements and ultrafast spectroscopy are carried out on the Ag-decorated and pristine ZnSe NWs to study the plasmon-induced changes in optical properties. To understand the importance of the resonant condition between metal NP LSPR and semiconductor bandgap, ZnSe NWs were also decorated with Au NPs. The Au NP LSPR does not overlap with the bandgap of ZnSe NWs. By contrasting the results of Ag-decorated ZnSe NWs with Au-decorated ZnSe NWs, the importance of the resonant condition can be understood.

1.5.4 Cobalt-doped ZnO nanowires

ZnO is an abundant, thermodynamically stable, and wide bandgap material that is very promising in applications for photoelectrochemical (PEC) water splitting. The final part of Chapter 5 presents the controlled modification of the optical properties of ZnO NRs as a function of Co-doping. The samples with different doping levels were studied using cathodoluminescence and ultrafast spectroscopic techniques. PEC measurements are also presented to show the efficiencies as a function of doping levels. This allows for studying the correlation between changes in optical properties due to doping and the corresponding changes in the efficiency as a photoanode material. The application driver for this study is the usability of Co-doped ZnO NRs as PEC water splitting photoanodes. Once the optimal Co-doping concentration is determined, these NRs are further functionalized with the help of a metal-organic framework (MOF) around them forming a core-shell structure. These core-shell NRs are then characterized using the same techniques.

Chapter 2 Experimental techniques

During this thesis work, I have used several optical characterization techniques to study the steady-state and transient optical properties of semiconductor NWs. This chapter provides a brief review of the experimental techniques and set-ups used in this thesis. Although several techniques are used, the ultrafast pump-probe technique is the main experimental method used throughout this thesis.

2.1 Fast Transient Absorption Spectroscopy

Ultrafast spectroscopic techniques make use of an ultra-short, strong pulse of the laser, usually in the femto- to attosecond time range, to perturb the carrier distribution in a sample. This sample is then investigated by a probe pulse to study the photoinduced processes due to the pump excitation. Using a pump-probe setup (sketched in Figure 2.1), we can systematically study the temporal evolution of the photoinduced changes by varying the time delay between the pump and the probe using an optical delay line. In this way, one can investigate the temporal evolution of the spectra as well as the wavelength dependence of the characteristic times of the processes involved in the carrier dynamics.

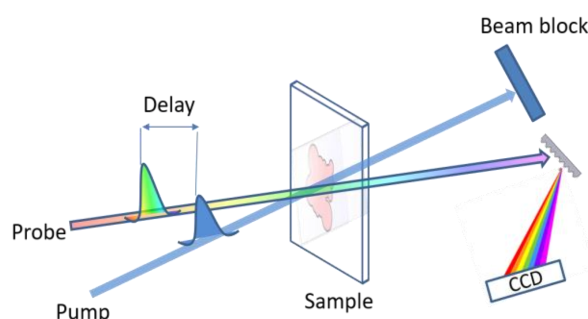

Figure 2. 1. Schematic representation of a pump-probe experiment.

Developments in ultra-short laser pulse generation have significantly improved the field of ultrafast spectroscopy.[63,64] The two common sources of ultrashort laser pulses are Ti-Sapphire laser and the Yb doped crystal fiber laser.[65] The Ti- Sapphire lasers provide lasing around 800 nm with pulse durations as short as ~20 fs. In this work, we have used a mode locked Ti-

Sapphire laser, based on the Coherent Vitara-T oscillator system, with a frequency of 80 MHz, 20 fs short pulses and a power of 550 mW. This pulse is then amplified using a regenerative amplifier to produce output at 800 nm with a pulse length of ~ 35 fs at 1 kHz, and pulse energy of 4 mJ. The output of the regenerative amplifier is divided into two: a major part of the output goes into an Optical Parametric Amplifier (OPA). The OPA allows us to tune the pump wavelength from 240 nm to 20000 nm, with a pulse length of 35 -40 fs with a repetition rate of 1 kHz. A very small part (3μJ) of the output of the regenerative amplifier is used to produce the probe. The probe is usually kept at a very low power to prevent sizeable perturbations in the sample.

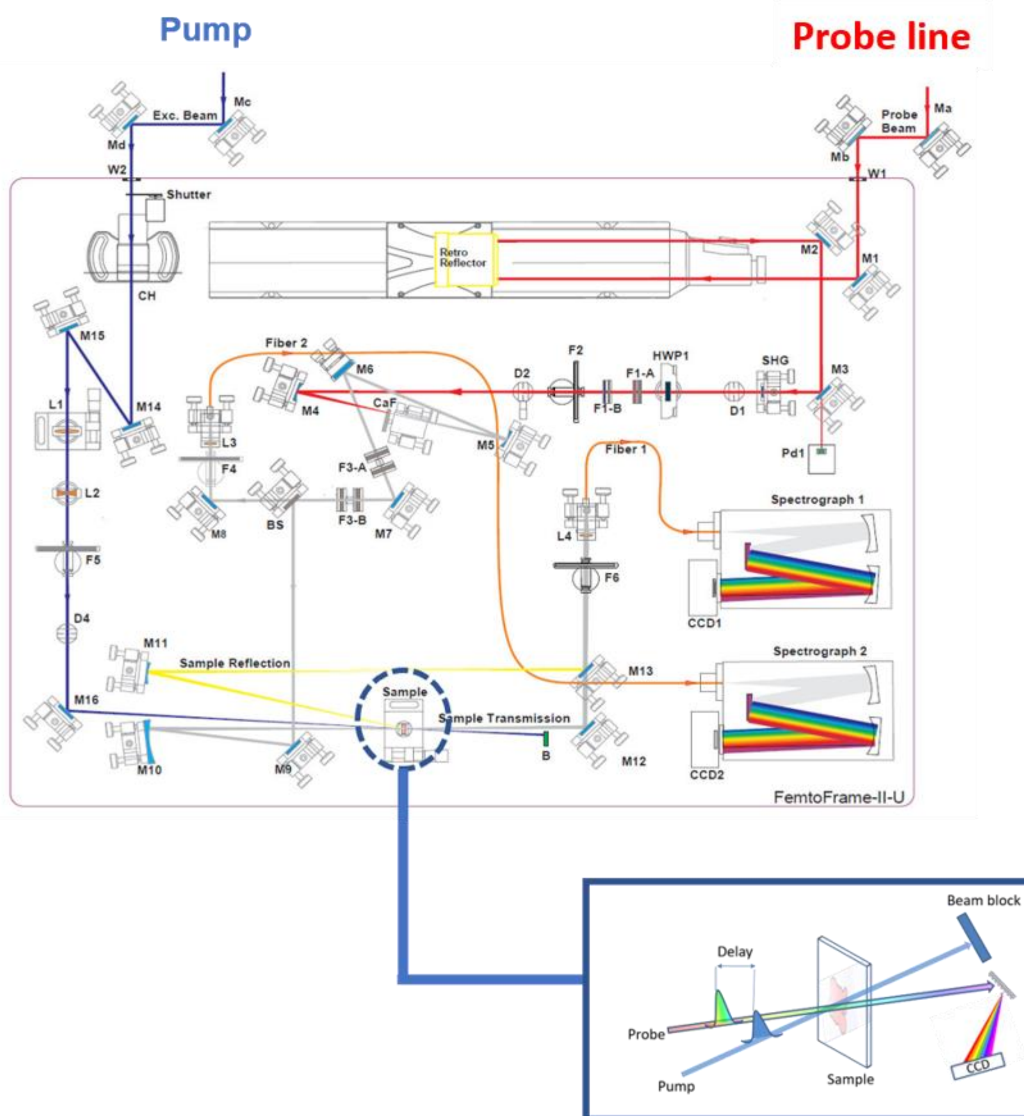

Figure 2. 2. Schematic representation of FTAS set up.

Figure 2.2 presents the schematic of the FTAS setup. The pump-probe experiments are performed using a commercial femtosecond transient absorption spectrometer (FemtoFrame II, IB Photonics). The tunable output from the OPA acts as the pump and is depicted by the blue ray in Figure 2.2. The tunable output from OPA allows the user to choose the pump energy according to the system that is being measured. The functioning of the OPA is described in Appendix A.1. The pump enters the spectrometer through the optical port W2 and after entering the spectrometer it first passes through a chopper (CH), and then into a telescope composed of two lenses that help focus the spot size of the pump on the sample. The M16 mirror helps to move the pump spot such that it can be aligned with the probe spot on the sample. The red ray shown in Figure 2.2, entering the spectrometer through the port W1 is the low power portion of the 800 nm laser. Immediately after entering the spectrometer, the 800 nm light is reflected from a flat mirror M1, and passes through a delay line, that helps to control the time delay in the pump-probe experiments. After this step, the 800 nm beam is directed using M2 and M3. A small portion of the light is passed through M3 to a photodiode for synchronization. F2 is a neutral density filter that helps to control the amount of the 800 nm light that goes into the white light generation. The beam is then focused using the M4 concave mirror into a rotating CaF_2 crystal which produces a supercontinuum in the spectral range of 350 - 800 nm. The white light supercontinuum is focused using another concave mirror M5. After this, using a beam splitter (BS), the white light probe is split into two, in which 50 % of the white light passes through the BS and is used as a reference to account for pulse-to-pulse variations to give better signal to noise ratio, and the reflected half is directed to mirror M9 that reflects it to a collimating mirror M10, which focuses the probe on the sample. The reference beam reflects through flat mirror M8 and is collimated using L3 into an optical fiber that takes it to spectrograph 2 for detection. The intensity that enters the fiber is controlled by neutral density filter F4. An IR supercontinuum probe (800-1600 nm), obtained using a YAG crystal, is also available for TA experiments. After passing through the sample, the pump beam is blocked from entering the spectrograph by a beam blocker shown in Figure 2.2 as B, while the probe beam can be recorded either in transmission or reflection. Probe reflection from the sample is focused by concave mirror M11, while probe transmitted through the sample is reflected by mirror M12. Mirror M13 is a flip mirror to be used while measuring in reflection. F6 is a neutral density filter that helps to control the intensity of reflected/transmitted probe entering the fiber after being focused by L4 and taken to spectrograph 1 for detection.

During the measurement, the pump and the probe are focused on the same spot on the sample. The pump is chopped off at a reference frequency with a controlled time delay after pump pulse. In the visible range, two spectrometers simultaneously measure the reference probe and the probe that passes through the sample. Because of this dual probe beam setup, signals are collected through a two-step process. The probe and reference probe are recorded at each step with the chopper or shutter on and off, hence giving probe values with pump on and pump off. The two probe beams simultaneously pass through two different spectrographs and get dispersed by monochromators before being detected by CCDs. Since we measure the probe transmitted through the sample, the absorbance, A is defined in terms of transmittance, T as follows:[64,66]

$$A = -\log(T) \qquad (2.1)$$

The measured quantity is the difference in absorbance (ΔA) of the probe transmitted through the excited sample and that transmitted through the unperturbed sample as a function of the delay time between pump and probe, and probe wavelength (energy), given by:

$$\Delta A = A_P - A_0 \qquad (2.2)$$

where A_p is the absorption with pump and A_0 is absorption without pump excitation. Therefore,

$$\Delta A = \log\left(\frac{T_0}{T_P}\right) \qquad (2.3)$$

where T_0 is the transmittance of probe pulse without pump excitation and T_P is the time-dependent transmittance with pump excitation. This can be defined in terms of probe intensities as,

$$\Delta A = \log\left(\frac{T_0}{T_P}\right) = \log\left(\frac{I_{Pr}^{0}/I_{Ref}^{0}}{I_{Pr}^{exc}/I_{Ref}^{exc}}\right) \qquad (2.4)$$

where the lower index shows if it is probe (pr) or reference (ref), and upper index denotes if with pump excitation, i.e., with chopper open (exc) or without pump excitation i.e., with chopper closed (0).

An important aspect to keep in mind while acquiring TA spectra is something called chirp. This feature is introduced in the probe because of the temporal dispersion experienced by different spectral components of the white light continuum. For this reason, different spectral components enter the sample at slightly different time delays (<1 ps). A chirp correction must be made on all acquisitions to bring the data to a common zero before analysing the data. The figure below shows the TA spectra before and after chirp correction.

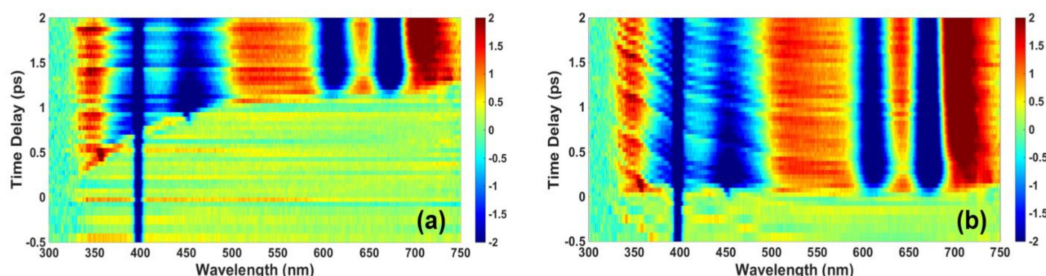

Figure 2. 3 2D false colourmap of FTAS spectra of a sample with wavelength along x-axis and time delay along y-axis, (a) shows the spectra with chirp, and (b) shows the spectra after chirp correction. After chirp correction, the zero is the same for all wavelengths.

The TA spectra can have either positive or negative values for the ΔA depending on absorption of probe light by the photoexcited sample. A negative ΔA is indicating that the probe light can pass through the sample being less absorbed by the photoexcited sample compared to unexcited sample. This happens because the pump excitation causes the depopulation of the valence band in the semiconductor. A negative ΔA due to photoexcitation of carriers due to pump from the valence band to the conduction band is called an absorption bleaching. A positive ΔA corresponds to the increase in absorption of the probe. Figure 2.4 shows the schematic of different pump induced processes in a direct bandgap semiconductor. One of the examples where the ΔA is positive is the intraband free carrier absorption.

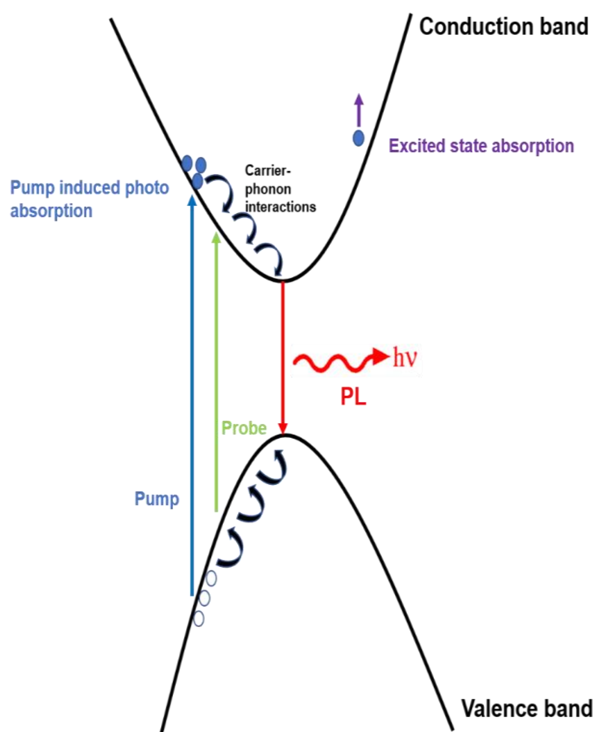

Figure 2. 4. Schematic of different pump induced processes in a direct bandgap semiconductor.

In this work, I have used different pump energies depending on the material system under study. The samples have been probed using the IR and visible probe as needed. The measurements in this work are done in transmission mode. The samples have been measured both at room temperature and some samples also at 77 K using a liquid nitrogen cooled cryostat.

2.2 UV – Visible Spectroscopy

UV-Vis spectroscopy is one of the most widely used tool for the optical characterization of different materials. Using an UV-Vis spectrometer one can measure the intensities of absorbed, transmitted, or reflected light as a function of wavelength from UV to near IR. In this thesis, I have used a Perkin-Elmer Lambda 35 spectrometer for measuring the static absorption of different NW samples. The instrument has a working range from 190 nm to 1100 nm with a double beam configuration allowing reference to be measured and corrected in real time.

2.3 Steady state and time resolved photoluminescence

PL is an optical property of materials in which light is emitted after the absorption of photons. PL spectroscopy is an important tool for studying the optoelectronic property of materials because of its non-destructive nature. During optical absorption in semiconductors, typically involving incident photons with energy greater than the bandgap energy, the electrons get excited from the valence band to the conduction band, leaving a hole in the valence band, thus creating a non-equilibrium distribution of electron-hole pairs. The excited carriers cool down to the respective band edge and finally recombine, radiatively or non-radiatively. In the radiative case, the recombination energy is emitted as a photon. For direct gap semiconductors, in momentum space, the transition occurs at k=0. In this case, the probability of radiative recombination is high, with important applications in light emitting devices.[67,68] In the case of indirect bandgap semiconductors, the transition is not vertical in the energy versus momentum dispersion relationship. Hence, it involves phonons as a momentum conserving agent. In this case, the radiative recombination is less efficient. Si is an example for such a material.[69]

In this work, PL spectroscopy is carried out both at room temperature and at low temperatures down to 10 K with the help of a closed cycle He cryostat. The cryostat operates in vacuum with the help of a turbo pump. A PID temperature controller is also connected to the cryostat to measure PL at all intermediate temperatures between room temperature and 10K. The samples are excited using a continuous wave (CW) laser at 405 nm supplied by the *Matchbox 2 laser series* or pulsed laser from the second harmonic generation (SHG) from the mode locked Ti-Sapphire laser (800nm, 80 MHz) at 405 nm. The laser is focused on the sample, and the luminescence from the excited sample is collected and sent to the monochromator. The monochromator is the *HORIBA Jobin Yvon – iHR320.* The monochromator has a focal length of 320 mm, and a spectral range of 350 nm -1100 nm with 1200 gr/mm grating.

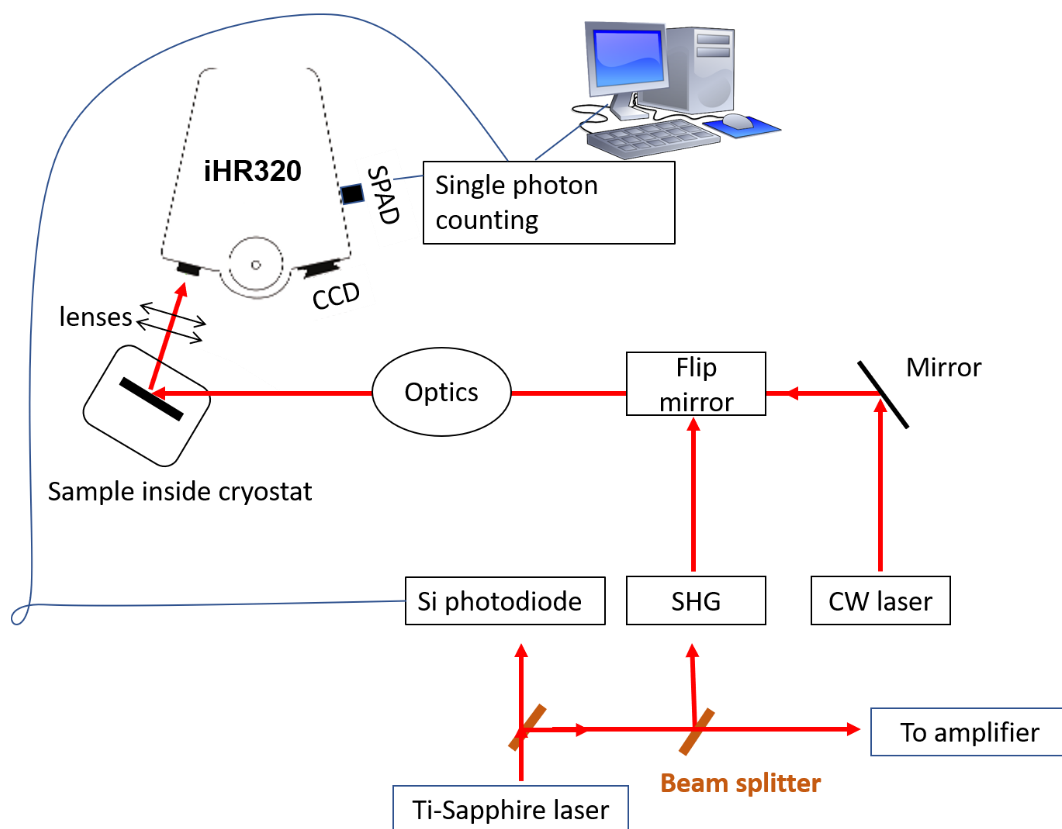

Figure 2. 5. Schematic of the PL and TRPL setup.

The monochromator consists of the entrance slit with a height limiter through which the collected light is sent to a collimating mirror. From the collimating mirror the light is incident on the diffraction grating turret which sends the signal to a focusing mirror. The focused signal is then sent to either to the charge coupled device (CCD) detector or to the single photon counting detector. The CCD collects the emitted signal and produces the PL spectra while the single photon detector based on a silicon single photon avalanche photodiode (SPAD) helps in time correlated single photon counting (TCSPC). The start time for time resolved measurements are triggered by a Si photodiode. Figure 2.5 shows the schematic of the PL setup.

To measure high bandgap materials like ZnO, a pump greater than 3.1 eV was required. So, they were studied on a different system which used the OPA tuneable output as a pump. These measurements were done in a *Halcyone* ultrafast system. *Halcyone* also provided time-resolved PL measurements performed at room temperature with a time-correlated single photon counting (TCSPC) system with a photomultiplier as the detector with an instrumental response function (IRF) of 0.5 ns.

2.4 Cathodoluminescence

Cathodoluminescence (CL), like PL, is an emission spectroscopy. In CL, we capture the luminescence from a material under electron radiation in an electron microscope. When the beam of energetic electrons impinges on the sample, it leads to emission of photons during the recombination of the exited carriers. The wavelength of the emitted photon is characteristic of the material under study and is generally identical to the PL. Of course, CL provides a much better spatial resolution and the possibility to link spectral features to structural aspects. CL microscopy involves the combination of SEM and CL spectrometer. In this thesis I have used CL measurements to study the optical properties of Co-doped ZnO nanorods. CL measurement on delicate nanostructures can be disruptive due to the melting of the nanostructures by the electron beam.

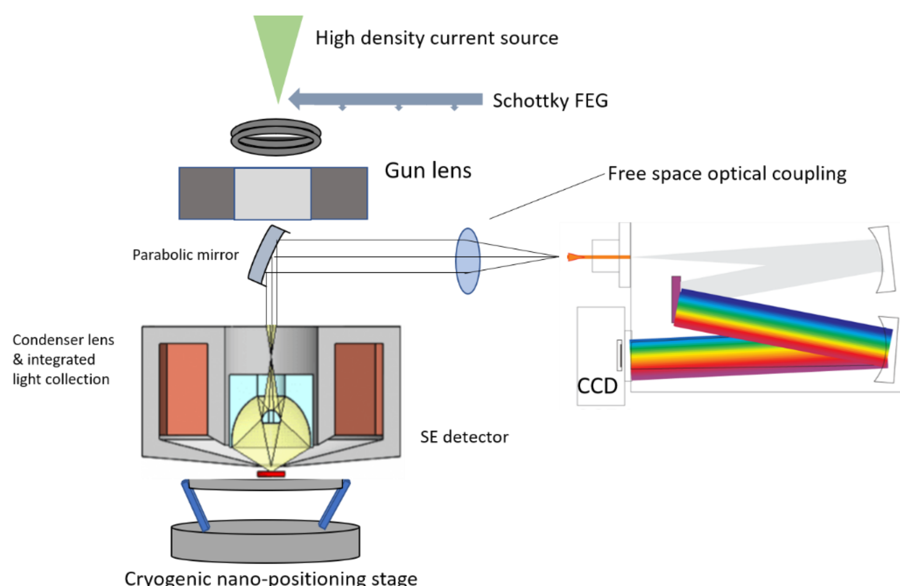

Figure 2. 6. Schematic representation of CL set up.

All the CL measurements were done at the Centre Interdisciplinaire de Microscopie Electronique (CIME), Ecole Polytechnique Fédérale de Lausanne (EPFL) during a 2-month long research secondment in the Laboratory of Semiconductor Materials (LMSC). The CL measurements were done using the *Attolight Allalin*, which is a quantitative CL spectroscopy instrument that integrates electron microscopy and optical microscopy. It produces both SEM images and panchromatic CL maps simultaneously. In the Allalin spectrometer the light microscope and the objective lens of the SEM are integrated in a way that their focal planes match each other. Measurements can be done both in the UV-Vis and in the NIR region using Si and InGaAs detectors, respectively. Measurements are possible both at room temperature and at liquid He temperatures, under high vacuum. This instrument allows one to register

complete emission spectrum at each pixel. The numerical aperture is 0.72, and the field of view is 300 µm. The electron beam spot size used is about 10 nm. Figure 2.6 shows the schematic of the CL setup used for the measurements.

2.5 Raman Spectroscopy

Raman spectroscopy is a powerful characterization tool that helps us study the structural properties of materials. It is a non-destructive measurement technique. In Raman spectroscopy, the sample is illuminated by a laser source, it interacts with the incident light, and we study the light scattered from the sample. The scattering events are because of the interaction of light with the vibrational or rotational states of the material. Depending on the type of scattering, the frequency of the scattered light may be the same as that of the incident light called Rayleigh scattering, or slightly different from the incident light called Raman scattering. If scattered photons have lower energy than incident light it is called a Stokes Raman scattering and if they have higher energy it is called anti-Stokes Raman scattering. Depending on the population of the different energy states at any given temperature, the probability of the scattering being Stokes or anti-Stokes is determined. The intensity of anti-Stokes line is strictly temperature dependent in a system at thermal equilibrium because these processes occur when the system is not in its ground state.[70] Figure 2.7 shows different scattering phenomena when light interacts with a sample.

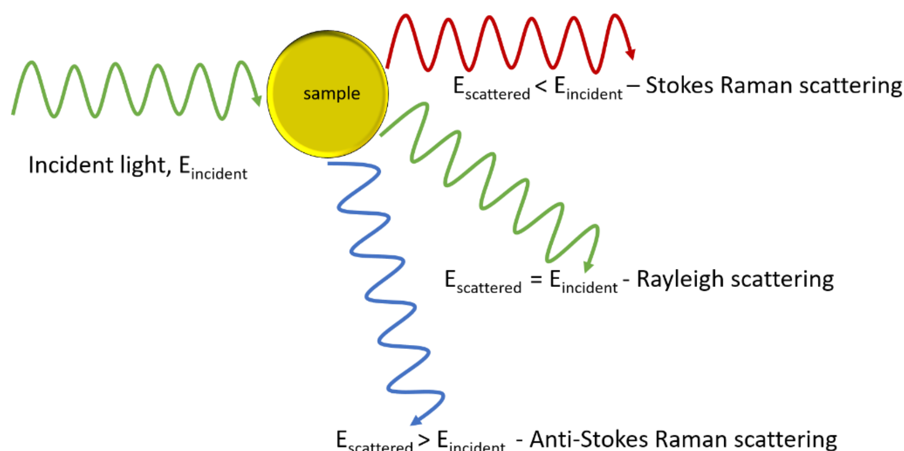

Figure 2. 7. Diagram showing different types of scattering when light is incident on a sample.

The frequency of the scattered photon, $\omega_{scattered}$ is given by,

$$\omega_{scattered} = \omega_{incident} \pm \frac{E_{initial} - E_{final}}{\hbar} \quad (2.5)$$

$$\omega_{scattered} = \omega_{incident} \pm \omega_{if} \qquad (2.6)$$

where the incident photon has a frequency of $\omega_{incident}$ and $E_{initial}$ and E_{final} are the initial and final energy states of the system, and $\omega_{if} = \frac{E_{initial} - E_{final}}{\hbar}$. For Rayleigh scattering, the $\omega_{scattered} = \omega_{incident}$, meaning the system returns to the initial state after the scattering event. Because of momentum conservation rules,

$$\boldsymbol{k}_{scattered} = \boldsymbol{k}_{incident} \pm \boldsymbol{k}_{if} \qquad (2.7)$$

$$\boldsymbol{k}_{if} = \boldsymbol{k}_{incident} - \boldsymbol{k}_{scattered} \qquad (2.8)$$

where $\mathbf{k}$ is the corresponding wavevector, and the subscript indicates the process. Now the frequency and momentum difference after scattering is given by ω_{if} and k_{if}, respectively. The energy and momentum conservation are satisfied in the Stokes and anti-Stokes scattering with the help of phonons.

The minimum and maximum values of $\boldsymbol{k}_{if}$ are obtained in the forward and backscattering geometries of incident and scattered light, i.e., when the angle between $\boldsymbol{k}_{scattered}$ and $\boldsymbol{k}_{incident}$ are 0^0 and 180^0, respectively. When illuminated by vis-IR the wavelength is much larger than the crystal lattice parameters, hence the corresponding wave vector is much smaller than the first Brillouin zone, hence the one-phonon scattering involves only phonons at the center of the Brillouin zone. In multi-phonon scattering mode, more than one phonon is involved in the momentum conservation. In this mode information regarding the whole Brillouin zone can be obtained.

Raman spectroscopy was used to study the GaAsP NWs and Ag decorated ZnSe NWs. The ZnSe samples were excited using the emission line from an Ar+ laser at 457 nm. The measurements were done in a Renishaw micro-Raman spectrometer while the GaAsP samples were done with a DXR Thermo Fisher Scientific Raman Microscope, by exciting the samples at 532 nm with a power of 2 mW.

2.6 Thermal Evaporation

Thermal evaporation of ultrathin films of Ag and Au were carried out on the sidewalls of ZnSe NWs to study the effects of plasmonic resonance on the optical properties of the semiconductor NW system.[9] A *Blazer 510 Evaporation system* was used to deposit the metals by thermal evaporation under ultra-high vacuum obtained by cryopump APD Cryogenics. The thickness was monitored by an *Inficon* quartz microbalance.

2.7 Sample preparation

The NW samples were measured as-grown mode if the sample transmitted enough light to produce successful TA spectra. Si NWs were measured this way. Another way of sample preparation was by mechanical rubbing of the as-grown samples on a transparent substrate like quartz. This was done, for example, for measurements on InP NWs. Yet another way of transfer was drop casting the NWs on a transparent substrate after dissolving NWs in a volatile solvent like isopropanol. A problem with transferred NWs is that, because of their tiny mass, the comparatively large momentum transferred by pulsed laser pump can easily displace them from the support making measurements on the same transferred wires over a long period of time difficult. The Figure 2.8 below shows a photographed image of GaAs NW sample as-grown as well as transferred mechanically onto a transparent quartz substrate.

Figure 2. 8. The photographed images of (a) as-grown GaAs NW sample and (b) Mechanically transferred GaAs NWs onto a transparent quartz substrate for FTAS measurements.

Chapter 3 Carrier dynamics in silicon nanowires

3.1 Introduction

Crystalline Si is single-handedly responsible for transforming the face of computation and information technology. Si is the second most abundant element after oxygen on earth.[71] Si is responsible for almost 90% of the world's photovoltaic cell production and currently has about 26.7% efficiency when used in Si single junction crystalline solar cells and a staggering 35.9% when used in multijunction solar cells.[33] Si also has several applications in photonics,[72] biosensing,[73] photodetectors,[74] and thermoelectric devices [75]. However, one of the most important and notable uses of Si is in the transistors that form the basis of almost all the fundamental computing devices. The Si-based transistors, after being introduced in 1954 by Bell Labs, revolutionized electronics. The size of these transistors kept shrinking and the number of these transistors on a microchip has been doubling every two years, and currently, we are reaching the limits of the miniaturization of this technology. This makes the study of lower dimensions of the material necessary.

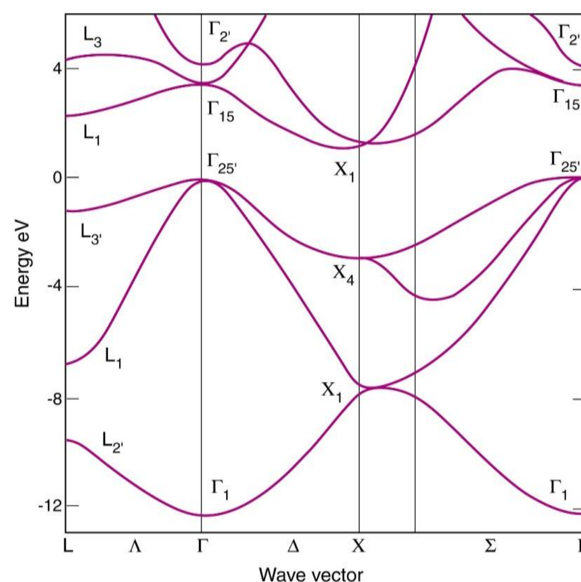

Figure 3. 1. Schematic of the band structure of Si, taken from Fauchet, 2005 [78].

Si NWs are important because of the ease of incorporation into different device structures. Apart from the familiarity of the technological world with Si, the NW structure increases surface area to volume ratio providing better photonic response.[76] Si is an indirect bandgap semiconductor with fundamental bandgap at 1.1 eV.[77] The direct transition in Si is at around 3.3 eV at room temperature. Figure 3.1 shows the schematic of band structure of Si taken from Fauchet, 2005.[78] In this thesis, ultrafast spectroscopy of Si NWs is studied in detail with emphasis on the observation of the direct ($\Gamma_{25} \rightarrow \Gamma_{15}$) transition using pump energies below the direct bandgap transition energy. This work is done as a final part of a more general study[79] on the ultrafast spectroscopy of Si NWs, which includes the study of the carrier dynamics in the visible and NIR regions with pump energy equal or above the direct bandgap energy, contained in Lin Tian's doctoral dissertation.[80]

The diameter of the Si NWs studied above is too large to observe confinement effects, which becomes important for very thin NWs. Since Si is an indirect bandgap semiconductor, there are limitations to its use as a light emitting material. However, with decreasing diameter to about 10 nm, a blue shift of the bandgap is observed.[38,81–83] As size becomes smaller and comparable with the exciton Bohr radius of the material, the motion of carriers and phonons becomes highly confined. The quantum regime of the material is reached and this confinement effect leads to modifications in the band structure and several other fundamental carrier interactions.[84] The exciton Bohr diameter of Si is 8.6 nm.[85] The last part of this chapter shows preliminary results on the ultrafast spectroscopy of ultrathin Si NWs with diameters around 9 $\pm$ 2 nm.[38]

3.2 Material

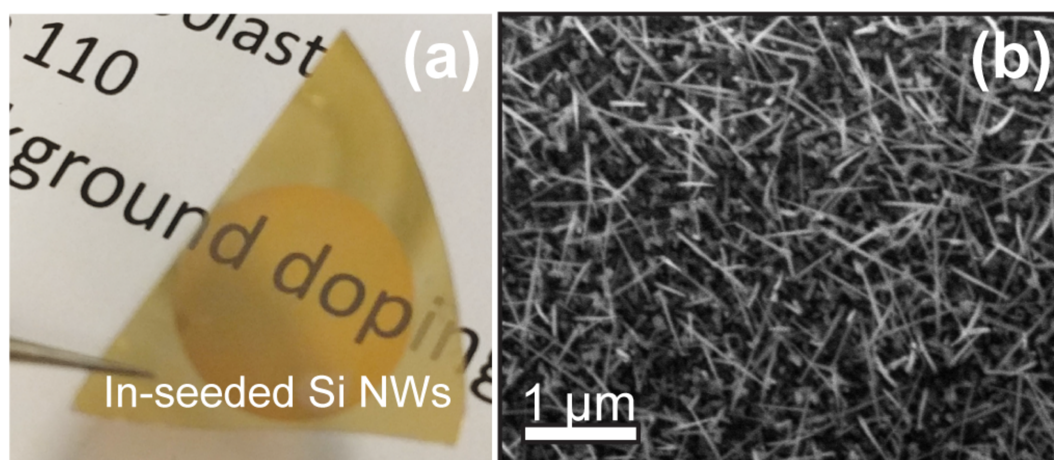

Figure 3. 2. (a) Picture of In-seeded as grown Si NWs on quartz substrate showing transparency; (b) SEM image of the same NW sample.

The In-seeded Si NWs used in the first part of this chapter were grown on transparent quartz substrate by plasma-enhanced chemical vapor deposition. The NWs were grown by Dr. Lin Tian in our laboratory.[79,80] Figure 3.2 (b) shows the SEM image of the Si NW sample. The NWs are randomly oriented, and highly dense, with about 80 nm in diameter and 1 μm long. The transparent nature of the as-grown samples (Figure 3.2 (a)) makes the ultrafast spectroscopy in transmission mode possible on the as-grown samples.

The quantum Si NWs were grown by the group of Dr. Alessia Irrera at the IPCF, CNR, Messina, Italy.[38] These NWs are grown by a metal-assisted wet etching process, creating NWs with a diameter of about 9 ± 2 nm and few micrometers in length. The two samples are named A179 and A137 with lengths 2.3 μm and 4 μm, respectively. Figure 3.3 shows the SEM image of the ultrathin Si NWs of different lengths.

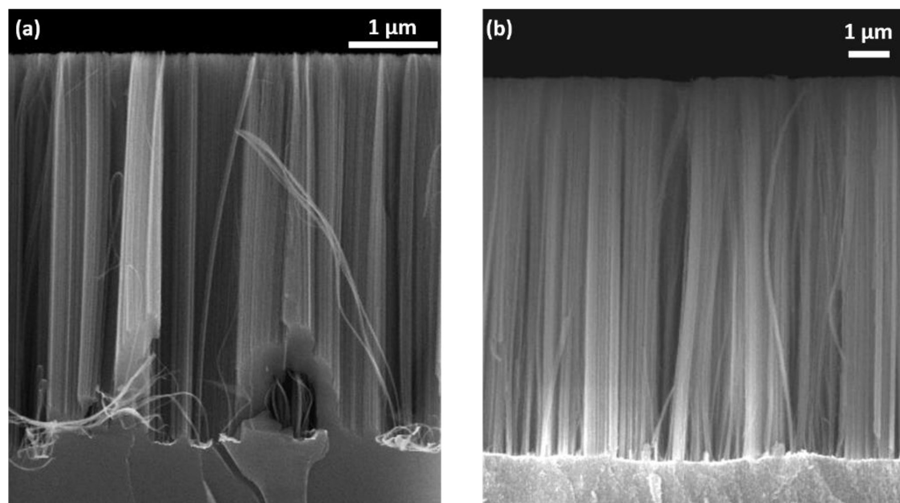

Figure 3. 3. SEM images of ultrathin Si NWs of lengths (a) 2.3 µm (A179) and (b) 4 µm (A137).

3.3 Optical characterization

The FTAS measurements were performed at room temperature with the help of different pump energies to excite the samples. The details of the excitation conditions will be given in the appropriate sections of the results. The TA signals were probed using a white light supercontinuum in the visible region of the spectra between 1.5 eV and 3.5 eV. The excitation pulses were 50 fs long with a repetition rate of 1 kHz. More details of the setup are explained in chapter 2.

3.4 Results

3.4.1 Ultrafast spectroscopy of In-seeded Si NWs

The Si NWs were excited with a pump laser of energy 2.34 eV, which is well below the direct bandgap (~3.3 eV) transition energy. Figure 3.4 below shows the results of FTAS on as-grown Si NWs when excited with a pump fluence of 318 μJcm^{-2}. The ΔA variation with probe energy and the time delay between the pump and probe pulses are studied.

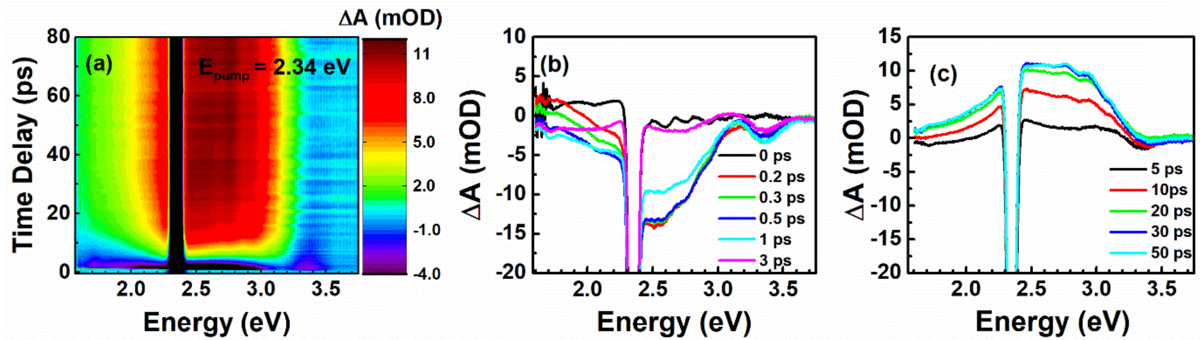

Figure 3. 4. (a) 2D false colourmap of results of FTAS measurement of Si NWs with the probe energy on the x-axis, and time delay between pump and probe on the y-axis; (b) and (c) show the TA spectra at different time delays between pump and probe. The NWs were excited using a pump at 2.34 eV with a fluence 318 μJ cm^{-2}.

The 2D false colourmap of the FTAS measurements in Figure 3.4. (a) shows a clear absorption bleaching at 3.3 eV even when the NWs were excited with a pump that is 1 eV lower than the direct bandgap energy. The bleaching signal at 3.3 eV reaches the maximum value within 1 ps and lasts for longer time delays up to ~100 ps. Another prominent feature in the FTAS spectra was the broad negative signal for energies above 2 eV. This signal is negative for short time delays, and between 3 ps and 5 ps, the signal turns positive, indicating photoinduced absorption.

Since the absorption bleaching at 3.3. eV is occurring with pump excitation 1 eV lower than the value required for this transition, this is attributed to the pump-induced depletion of electrons or creation of holes at top of valence band at Γ point rather than due to Γ_{25}-Γ_{15} transition of electrons.[86] 2.34 eV is greater than the indirect bandgap of Si, hence, it is absorbed because of indirect transitions (Γ-Δ) which deplete the electrons at the top of valence band, making them unavailable for absorption by the probe pulse leading to a negative signal. Hence by studying the dynamics of the TA signal at this energy, more information on hole dynamics can be studied. Comparing these results with the results obtained by excitation above the bandgap, the hole and electron dynamics can be disentangled.

Similarly, the observation of the broad signal below 3 eV with a bleaching maximum at around 2.5 eV is usually attributed to the creation of free holes at the top of the valence band and free electrons along Γ–L and Γ–X lines. However, its observation with pump excitation at 2.34 eV attributes this also to the depletion of electrons at top of valence band at Γ point, leaving fewer carriers available for the transitions along the Γ–L or the Γ–X lines. This signal reaches a maximum between 300 fs and 500 fs, which is in close agreement with the 660 fs [87], which is the time scale for electrons to relax from the Γ point to the L and X valleys in bulk Si.

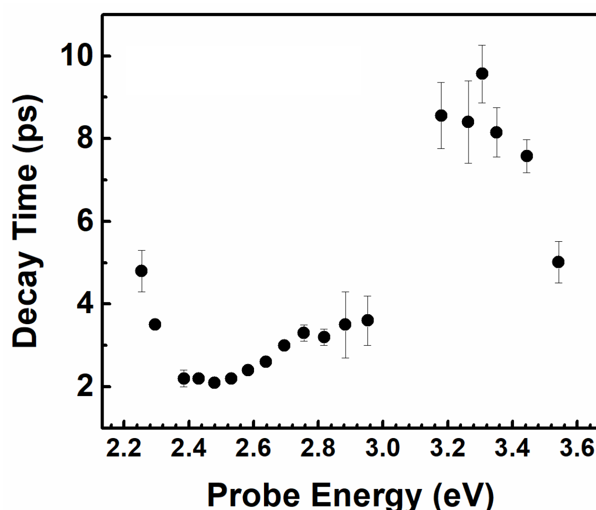

Figure 3. 5. The decay times at different probe energies when Si NWs were pumped at 2.34 eV, with a fluence of 318 μJ cm^{-2}.

A detailed analysis of the kinetics of the TA spectra at different probe energies are given below in Figure 3.5. The TA spectra at different probe energies were fit with a single exponential decay function. For energies between 2 eV and 3 eV, the fitting was intentionally limited to 5 ps to avoid the influence from the positive photoinduced absorption signals. The decay times between 2 eV and 3 eV, are between 2 and 4 ps, with a minimum value around a probe energy of about 2.5 eV, and then the decay times tend to increase as energies decrease until 2 eV. Above 3 eV, the decay time becomes 8 ± 2 ps. Since the bleaching at 3.3. eV is assigned to creation of holes in valence band because of indirect transitions, but not to the excitation of electrons in the Γ_{15} conduction band, the decay time in this energy region corresponds to the hole population dynamics.

From a previous work done in our lab, the TA spectra when Si NWs were pumped at 3.06 eV and 4.51 eV were studied. Those results along with the results in this thesis are published in Tian *et al.*[79] In the Figure 3.6 below, the TA dynamics when Si NWs were pumped at 3.06 eV and 4.51 eV are shown. For pump energies above and close to the direct bandgap values, the decay time of the bleaching signal around 3.3. eV was around 4-5 ps, which is shorter than what we observe when they were pumped at 2.34 eV. This difference could either be assigned to a reduced carrier-carrier scattering and/or to a reduced Auger recombination, due to a lower carrier density when excited with a pump of 2.34 eV. The decay dynamics when pumped at 2.34 eV is assumed to be that of the holes in the valence band because the electrons excited to the top of Γ_{15} are assumed to be negligible at this pump energy. This difference in decay times also suggests that the electron dynamics around and above Γ_{15} point in conduction band minimum is faster than the hole dynamics in the valence band.

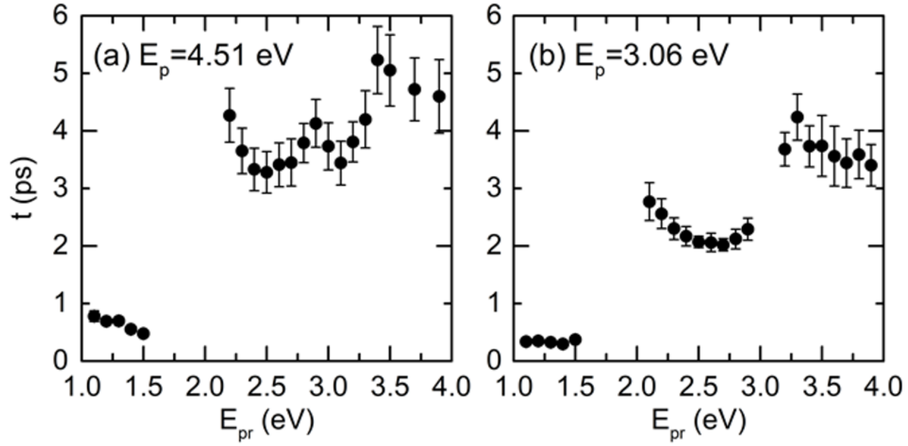

Figure 3. 6. Decay times at different probe energies when pumped at (a) 4.51 eV; (b) 3.06 eV. Taken from Tian et al. [79].

FTAS measurements were also performed using a lower fluence of 159 µJ cm^{-2} for the 2.34 eV pump. The results are summarized in the Figure 3.7 below. As expected intuitively, the intensity of the TA signal is weaker compared to the intensity of signal obtained with an excitation fluence of 318 µJ cm^{-2}. However, the spectrum is similar, and the TA spectra consist of a weak negative bleaching signal centered around 3.3. eV, and a broad negative signal centered around 2.5eV, which goes to positive after 4 ps. The change of the signal from negative to positive indicates the possibility of photoinduced absorption, due to reabsorption of the photons by the excited carriers in the presence of the probe. It might be due to the combined contribution of free carriers generated below the 3.3 eV, along the Γ-X transition for energies above 1.12 eV and Γ-L transition for energies above 2 eV.

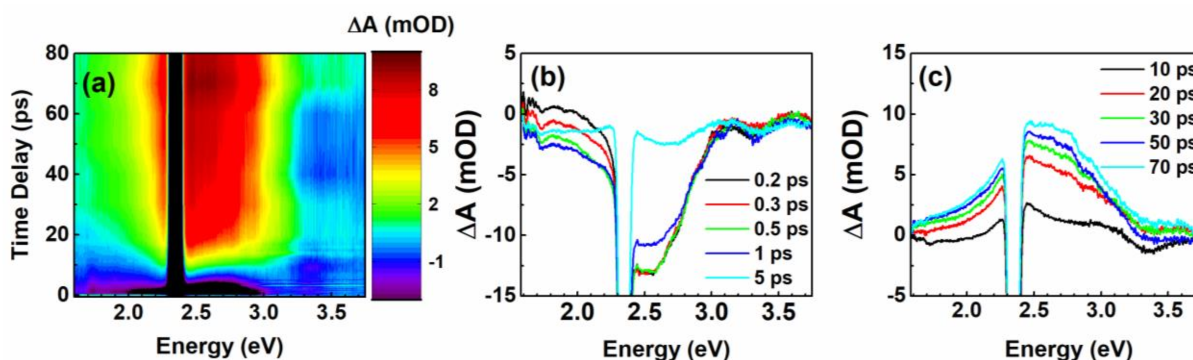

Figure 3. 7. (a) 2D false colourmap of results of the FTAS measurement of Si NWs with the probe energy on the x-axis, and time delay between pump and probe on the y-axis; (b) and (c) show the TA spectra at different time delays between pump and probe. The NWs were excited using a pump at 2.34 eV with a fluence 159 μJ cm^{-2}.

Figure 3.8 (a) below shows the normalized ΔA intensity at 3.3. eV as a function of delay time for two fluences. The normalization is done within [0,1], with the highest negative value of ΔA going to 0. The signal to noise ratio for 159 μJ cm^{2} is low, hence an accurate fit for decay time was not plausible at the direct bandgap energy. However, within this limit, the normalized ΔA shows that there is no significant change in decay time with fluence. Figure 3.8 (b) shows the decay time as a function of probe energy between 2 eV and 3 eV for two different fluences. The lowest decay time was at 2.5 eV for both fluences and all the decay times are between 2 and 5 ps, the higher fluence having slightly smaller decay time values probably because of increased carrier-carrier scattering because of a higher carrier density.

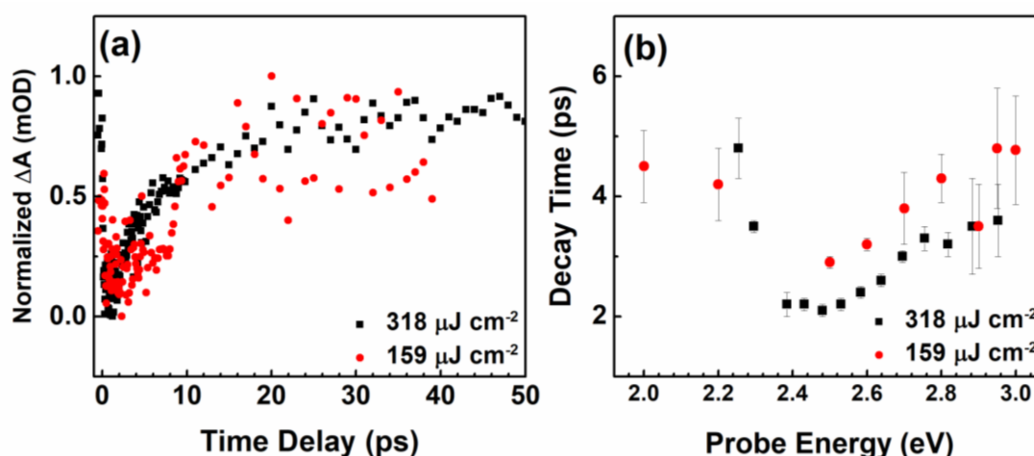

Figure 3. 8. (a) Normalized ΔA at 3.3 eV as a function of delay time for two different excitation fluences; (b) Decay time as a function of probe energy for two different fluences. The red and black points correspond to 159 μJ cm^{-2} and 318 μJ cm^{-2} respectively.

Another important feature of the excitation below the direct bandgap is the lack of bandgap renormalization (BGR) compared to the excitations using pump energies above the direct bandgap. For pumps at 4.51 eV and 3.06 eV as demonstrated in Tian *et al*. there is a significant blue shift with increasing time delay. This blueshift has been assigned to the relaxation of the bandgap energies after BGR. The results of bandgap shift for pump energies higher than or close to the direct bandgap is shown in Figure 3.9.[79] The BGR occurs when carriers created during the excitation is above a critical carrier density, whose value is around $6x10^{18}$ cm^{-3} for Si.[88] Initially at high carrier densities, the bandgap shrinks due to strong Coulomb interaction between the carriers, and then relaxes when the photoexcited carrier density reduces, appearing as a blueshift. The initial shrinking of the bandgap cannot be observed with the time resolution (50 fs) of our experimental setup. Thus, only the recovery from the BGR is observed, appearing as a blue shift. The bandgap shrinkage or the BGR is assigned a temporal upper limit of 450 attoseconds by Schultze and coworkers.[88] However, for 2.34 eV pump, no significant shift in bandgap is observed, because the excited carrier density is less than the critical carrier density. The carrier densities calculated for pumps at 3.06 eV and 4.51 eV are 6.96 x 10^{19} cm^{-3} and 9.12 x 10^{20} cm^{-3}, respectively. The values are obtained using the relationship[89]:

$$N_0=(1-R)\ I_0\alpha\eta/h\nu \qquad (3.1)$$

where I_0 is the excitation intensity (J cm^{-2}), R is the reflectance (see Appendix A. 2), α is the absorption coefficient and the value of α is taken at each energy value from the work of Aspnes and Studna,[90] and η is the carrier generation efficiency which is assumed to be unity. Similar calculation was performed for the pump at 2.34 eV, where the α value is about 10 times smaller than at 3.01 eV and about 200 times smaller than at 4.51 eV. The carrier density is found to be $3x10^{17}$ cm^3, which is well below the critical carrier density and is not enough to cause the BGR.

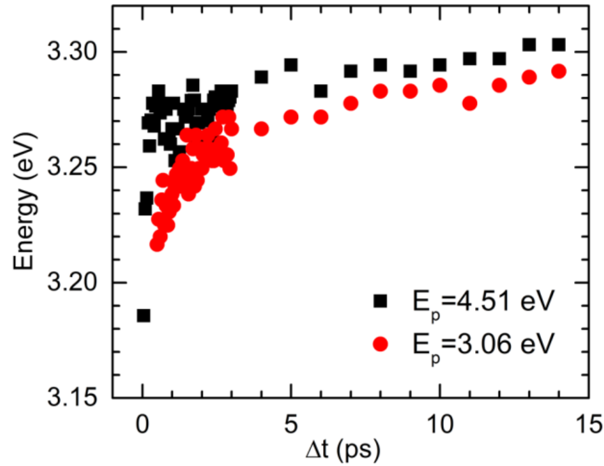

Figure 3. 9. Peak position of ΔA relative to direct bandgap energy as a function of time delay for pump energies at 3.06 eV and 4.51 eV.

In FTAS measurements with a pump at 3.06 eV, which is slightly smaller than direct bandgap transition energy, the dynamics of the bleaching signal reported is similar to that observed at 4.51 eV. This is probably because of combination of the thermal energy of carriers and effects due to strong optical field[91] leading to the population of Γ_{15} even with a pump of 3.06 eV.

3.4.2 Optical characterization of ultrathin Si NWs

The final section of this chapter presents introductory results on the carrier dynamics in ultrathin Si NWs. This work is aimed at probing the effects of quantum confinement on the carrier-carrier and carrier-phonon interactions in ultrathin Si NWs. This study is very preliminary and is presented to demonstrate that TA measurements can be done on ultrathin Si NWs to explore a plethora of exciting physics. However, due to the ongoing CoVid-19 global pandemic crisis, research on this topic is currently paused.

As mentioned in the initial section of this chapter, the A179 and A137 samples were grown at IPCF-CNR, and there the PL was carried out to characterize the emission. Figure 3.10 shows the PL emission of both NW samples. Both the ultrathin Si NWs show emission at around 1.8 eV at room temperature. The PL emission from A137 is narrower compared to that from A179, as well as more intense. FTAS measurements at room temperature were carried out on these two NW samples, after mechanically transferring them onto a transparent quartz substrate.

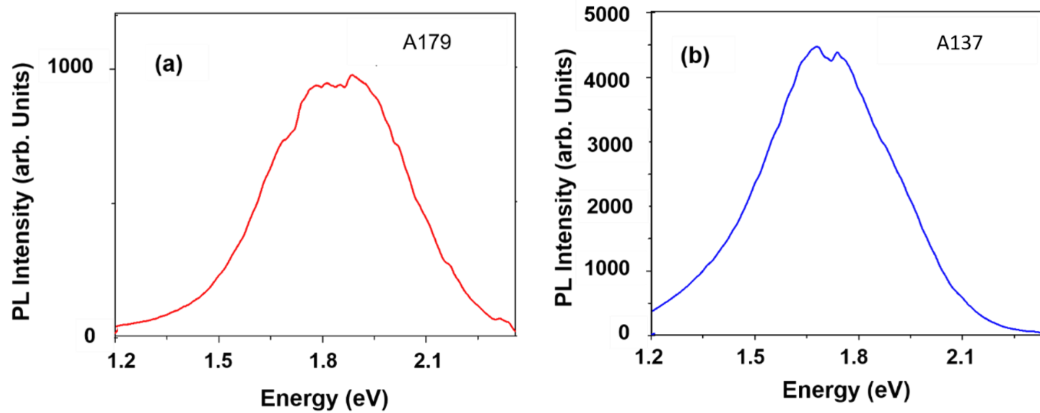

Figure 3. 10. Room temperature PL intensity of (a) A179 and (b) A137 ultrathin Si NWs.

3.4.2.1 Ultrafast spectroscopy of ultrathin Si NWs

After analyzing the PL spectra an appropriate pump energy was chosen. The NWs were excited with a pump at 3.02 eV with a fluence of 318 μJ cm^{-2}. The results of FTAS measurements are given in Figure 3.11. The sample A179 shows a prominent absorption bleaching around 1.75 eV, with the high energy tail extending to 2.2 eV. Similarly, for A137 there is a peak at 1.75 eV, with the high energy tail extending further into the visible part of the spectrum. For A137, which consists of longer NWs, the measurements showed a lot of scattered light in the signal collected during the measurement, while A179 provided a cleaner spectrum. For sample A179, the PL FWHM was about 0.49 eV, while that of the FTAS appears to be ~0.39 eV.

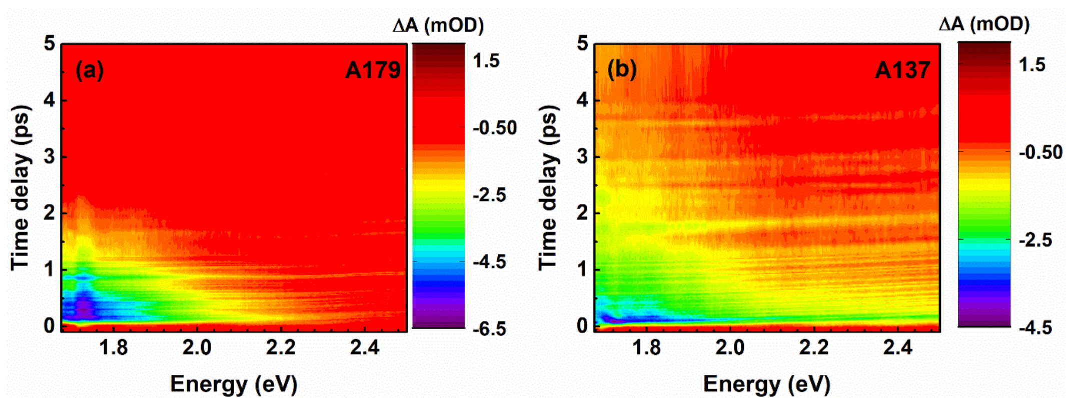

Figure 3. 11. 2D false colourmap of FTAS measurements at room temperature with a pump of 3.02 eV, and fluence of 318 μJ cm-2 for (a) A179 and (b) A139.

The dynamics of the TA signal for both the samples are shown below in Figure 3.12. For A179 and A137, the decay times were in the range of 1 -2 ps. There were no significant changes in the decay time values between the two samples. Towards the high energy tail of the absorption bleaching A137 tends to have slightly higher decay times compared to A179. It is important to note that for Si NWS of diameter 9 nm, we do not observe any of the signals observed for the 80 nm In-seeded Si NWs discussed in the first part of this chapter.

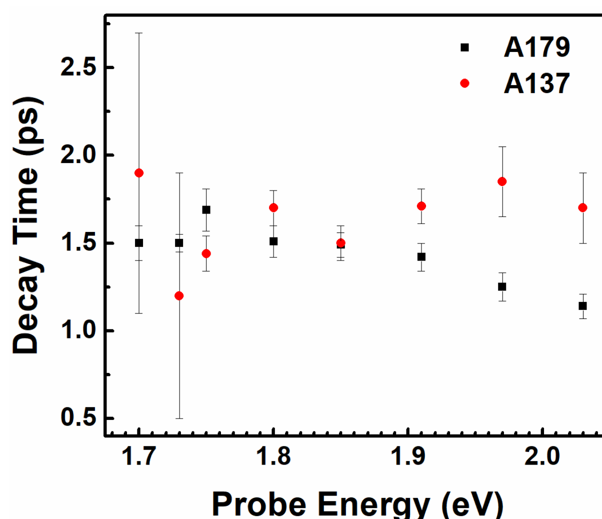

Figure 3. 12. The decay time of the ΔA signal as a function of probe energy for A179(black) and A137 (red), when excited with a fluence of 318 μJ cm^{-2} and pump at 3.02 eV.

3.5 Conclusions

In this chapter the ultrafast carrier dynamics in Si NWs when excited using a pump below the direct bandgap energy is studied using a visible probe. There are two prominent features in the probe range between 1.6 eV and 3.5 eV: a broad negative signal spanning 2 -3 eV, and a negative absorption bleaching at energy corresponding to that of the Γ_{25}-Γ_{15} transition at 3.3 eV. The broad negative signal undergoes a change from negative to positive in about 4 ps, indicating photoinduced absorption of free carriers. The presence of the bleaching signal at 3.3 eV, even when pumped at 1eV smaller than the required energy for the direct transition shows that the bleaching is observed due to the creation of holes at the Γ point at valence band maxima because of the excitation of indirect transitions. By comparing with pump excitation above the bandgap from literature, it was hence possible to distinguish between hole and electron dynamics. The hole dynamics around Γ point on valence band were found to be slower than that of electron dynamics. Another important observation is that the dynamics of the TA signals are pump energy dependent. This points to decay mechanisms dependent on carrier density,

such as exciton-exciton or Auger recombination processes. The short lifetime values obtained also points to possible surface trap mediated recombination processes.

For ultrathin Si NWs, preliminary TA measurements showed a bleaching absorption signal around 1.72 eV with the high energy tail extending up to 2.2 eV. The signals were short lived with about 1-2 ps of decay time constants throughout the bleaching signal. More measurements are to be carried out on these samples to extract useful information regarding changes in the optical properties due to quantum confinement in ultrathin Si NWs. This project is currently underway.

Chapter 4 Ultrafast spectroscopy of group III-V nanowires

This chapter discusses the results of ultrafast transient absorption spectroscopy on different nanowires of the III-V family. I have studied the transient absorption of InP, GaAs, and GaAsP. The chapter consists of three sections:

- Ultrafast spectroscopy of InP NWs:
    - In the first part of this chapter, micro-PL and FTAS of InP NWs of wurtzite and zincblende crystal structures are studied with the aim of identifying different electronic transitions in the two crystal phases and their corresponding carrier dynamics. A systematic study of the TA spectra using different pump energies and pump fluences are carried out.
- Ultrafast spectroscopy of GaAs NWs in the visible region
    - In the second part of the chapter, which is rather brief, the visible TA spectra of GaAs NWs are carried out to identify higher critical interband transitions.
- Diameter dependent cooling rate in GaAsP nanowires
    - In the last part of the chapter, GaAsP NWs of two different diameters are studied using ultrafast spectroscopy. T_C are extracted as a function of delay time.

4.1 Ultrafast spectroscopy of indium phosphide nanowires

The first material studied in this chapter is InP NWs. InP is a semiconductor with bandgap of about 1.4 eV and hence absorbs light in the near infrared (NIR) and in the visible regions of the spectra. The thermodynamically stable crystal phase of bulk InP is zincblende (ZB). However, depending upon NW growth conditions, wurtzite (WZ) crystal phase can also be achieved. The presence of two crystal phases offers more diverse optical and electronic properties due to differences in the band structure.[7,92–96] In certain cases, it is also possible to grow InP NWs containing both crystal phases.[97–102] Since it is now possible to intentionally create ZB/WZ homostructures during growth, as well as whole NW arrays of either ZB or WZ structures, it is important to know the characteristics of each of these structures to design devices using these NWs. Figure 4.1 shows the schematic band structure corresponding to the two crystal phases.

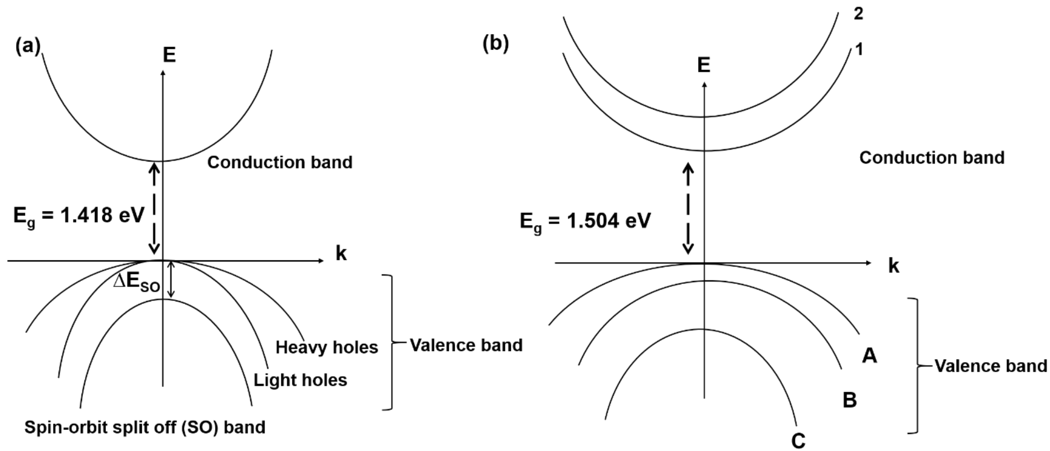

Figure 4. 1. Schematic diagram of (a)Zincblende and (b) Wurtzite InP.

Figure 4.1 (a) shows the band structure of ZB InP. The fundamental bandgap of ZB InP is about 1.418 eV at low temperature.[103,104] The ZB crystal structure, with a cubic symmetry, at k=0 the light and heavy holes are degenerate with a Γ_8 symmetry. The valence band further splits into a third band due to spin-orbit interaction and splits off to form another band with Γ_6 symmetry, called the spin-orbit split off band or SO band.[104,105] The energy difference between the valence band maxima and the maximum of the SO band is denoted by ΔE_{SO}, whose value is reported as 0.108 eV or as 0.11 eV.[106,107] The conduction band in ZB phase is of Γ_6 symmetry. In the case of WZ crystal phase, the symmetry of the structure is lower than that of ZB phase. In this case, apart from the spin-orbit interaction, the crystal field splitting also plays an important role. The light and heavy hole bands lose their degeneracy, and the valence band splits into three bands named as A, B and C with symmetries Γ_9, Γ_7 and Γ_7, respectively. According to calculations done by De and Pryor, the conduction band in WZ InP presents two conduction band minima of Γ_7 (CB1) and Γ_8 (CB2) symmetries.[108] This happens due to the zone folding of ZB L valley point in the Brillouin zone to the Γ point. De and Pryor predicted the energy difference between these two conduction bands to be 238 meV.[108] This was experimentally verified to be 228 meV and 230 meV by Wallentin *et al.*[109], and Saranga Perera *et al.*[95], respectively. The lowest energy transition in WZ is ~1.5 eV[7,104] or 1.504 eV[94] at low temperature. At room temperature these values are lowered by about 80 meV.[105] Table 4.1 shows the consolidated values of different electronic transitions associated with WZ InP in literature.

Table 4. 1. Different energy transitions in the WZ InP in literature at low temperature. I

Transition	Energy (eV)	Source	Temperature (K)
A to CB1	1.504	Perera *et al.*[94]	10
A to CB1	1.49	Hadj Alouane *et al.*[110]	14
A to CB1	1.493	Tuin *et al.* [111]	4
B to CB1	1.534	Perera *et al.*[94]	10
B to CB1	1.53	Hadj Alouane *et al.*[110]	14
B to CB1	1.533	Tuin *et al.* [111]	4
C to CB1	1.665	Perera *et al.*[94]	10
C to CB1	1.669	Hadj Alouane *et al.*[110]	14
A to CB2	1.731	Saranga Perera, Teng Shi *et al.*[95]	Not available
B to CB2	1.774	Saranga Perera, Teng Shi *et al.*[95]	Not available
C to CB2	1.897	Saranga Perera, Teng Shi *et al.*[95]	Not available

4.1.1 Material

The InP NWs were grown by Dr. Aruni Foneska at Canberra University by Au-seeded metal-organic vapor phase epitaxy (MOVPE) on a semi-insulating (100) InP substrate. Gold nanoparticles with diameter of 30 nm that acted as seeds for the VLS growth of the NWs were dispersed on the substrate. The samples were annealed under PH_3 flow for 10 min at 450℃ before carrying out the growth at the temperature and V/III ratio of 450 °C and 350, respectively. The growth was carried out for 60 min and the corresponding TMIn and PH_3 flows used were 2.0×10^{-6} and 7.0×10^{-4} mol/min. The samples contain vertical short wires of ZB crystal structure (some ZB wires also grow horizontally) and horizontal, longer wires of WZ crystal phase. Figure 4.2 shows both the top view and 45^0 tilted view of the sample, showing both WZ and ZB NWs. The NWs have an average diameter of 130 nm.

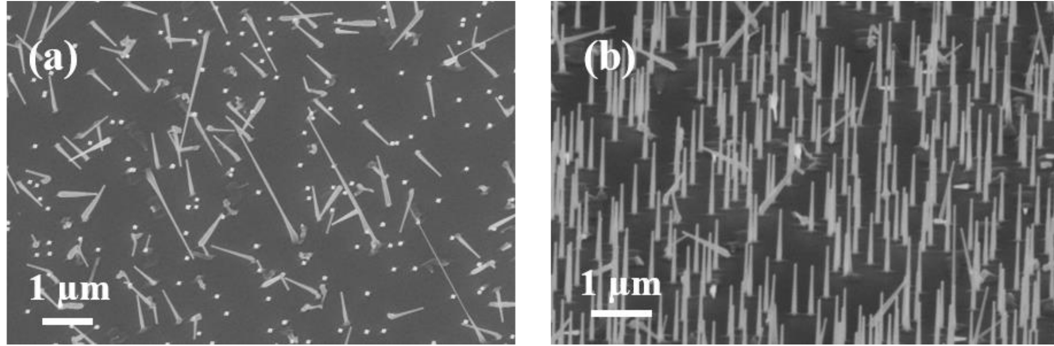

Figure 4. 2. SEM images of InP NWs: (a) Top view of the sample; (b) View at 45 ^{0} tilt. The longer horizontal wires are in WZ phase, while the shorter horizontal, and all vertical wires are of ZB phase.

4.1.2 Optical characterization

The InP NWs were characterized by micro (µ)- PL measurements at 10 K to verify the presence of both WZ and ZB homostructures under an optical excitation provided by the 632.8 nm line of a He-Ne laser. FTAS measurements were done at room temperature with different pump energies and excitation fluences. The NWs were probed using a white light supercontinuum in the visible part of the spectrum as well as the NIR part of the spectrum.

4.1.2.1 Micro PL on InP NWs

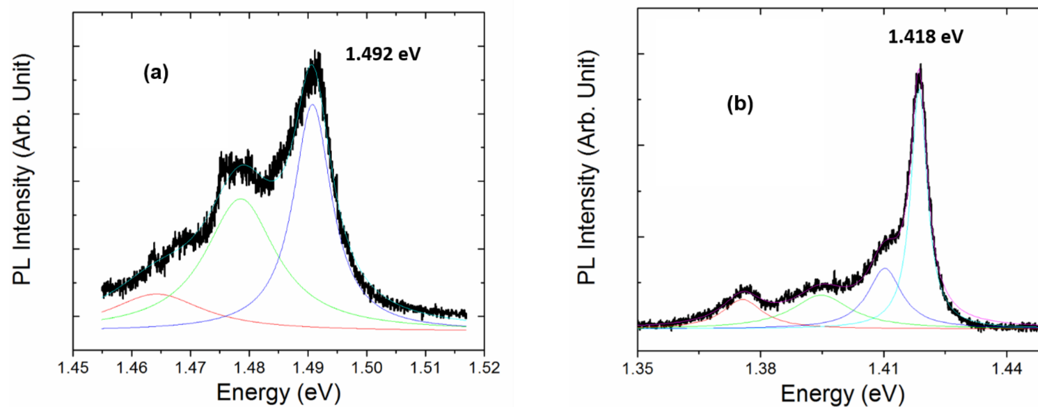

Figure 4. 3. µ-PL at 10 K for (a) WZ NW; and (b) ZB NW along with peak fits.

As a preliminary test, µ-PL measurements were done on transferred NWs, the results of which are shown above. The µ-PL allows one to measure the PL from both the long and short NWs and to distinguish them based on their PL. Figure 4.3 shows the WZ and ZB bandgap related PL emission at 1.492 eV and 1.418 eV, respectively at 10 K. The peaks were fit using a multipeak fit function consisting of the Lorentzian function. The peaks at lower energies are assigned to defect related emissions.

4.1.2.2 Fast transient absorption spectroscopy in the NIR

The room temperature TA measurements were done using two different pump energies: 1.9 eV and 2.25 eV. The TA signals were probed both in the visible and near infrared (NIR) region of the spectrum. Our setup puts a limitation on finding the energy of each transition accurately for InP because the white light super continuum used as the probe is generated by an 800 nm laser, which creates disturbances in the spectral window where the signals of InP transitions are present. Also, two different spectrometers are used for visible and NIR measurements, with the visible spectrometer measuring from 1.55 eV to 3.54 eV, while in the IR region it is between 1.49 eV and 0.78 eV. Hence, we are blind in a small region between 1.55 eV and 1.49 eV, which is however important while investigating InP.

Figure 4.4 shows the room temperature TA spectra of InP NWs measured after transferring them on to a transparent quartz substrate by mechanical rubbing. The 2D colourmap shows the TA in the NIR region. In this case, the samples were excited using a 1.9 eV laser with different excitation intensities varying from 318 μJcm^{-2} to 31.8 μJcm^{-2}. Figure 4.4 (a) shows the 2D colourmap when InP NWs are excited with a fluence of 318 μJcm^{-2}. Figure 4.4 (b) shows the TA spectra at 1 ps for the map shown in Figure 4.4 (a). The TA at 1 ps shows 4 different peaks named peak 1, peak 2, peak 3 and peak 4 with energies 1.37 eV, 1.418 eV, 1.464 eV and 1.472 eV, respectively. The peak energies were obtained after fitting the curve with a multi-peak function using Gaussian function.

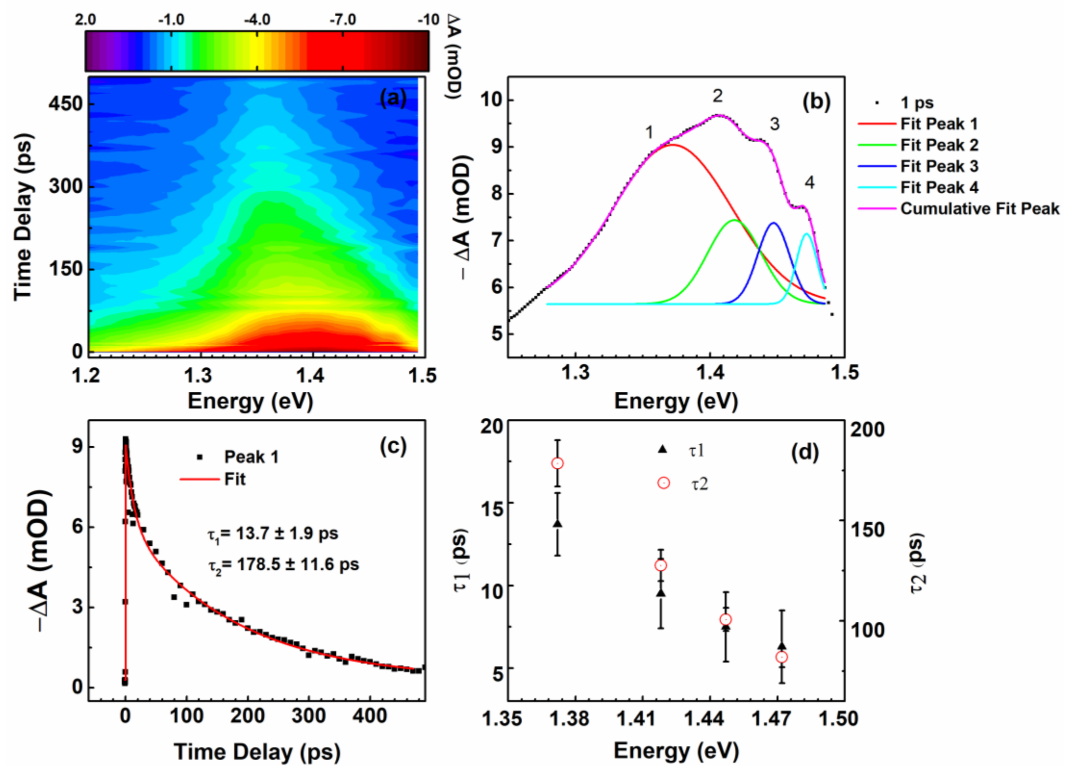

Figure 4. 4. (a) 2D false colourmap of ΔA of InP NWs with probe energy on the x axis, and time delay on the y axis; (b) Time cut at 1 ps time delay between the pump and the probe, along with the fits of 4 different peaks in the NIR region; (c) The time dependence of ΔA signal for peak 1 along with the double decay fit, and corresponding decay times;(d) Double-y plot of two decay times (τ_1 (black triangles) and τ_2 (red open circles)) for the 4 peaks in the NIR region. The samples were excited with a pump at 1.9 eV with 318 μJcm^{-2} fluence. Measurements were done at room temperature.

The dynamics of the decay signal for each of the peaks were fitted using a double exponential function considering the instrument response function (IRF) which is 50 fs. The fit for peak 1 along with the ΔA time dependence is shown in Figure 4.4 (c). Similar fits were done for all the 4 peaks. The decay shows 2 components, a fast one with decay constant τ_1 and a slower component with decay constant τ_2. For peak 1, it is τ_1 =13.7 ± 1.9 ps and τ_2 = 179 ± 12 ps. A double *y* plot shows the two decay time constants for the 4 peaks. The decay times decrease with increasing probe energy as it can be seen from Figure 4.4 (d). Similarly, the rise times of these peaks were fitted with a single exponential growth function. The results are summarized in Figure 4.4 below. Figure 4.5 (a) shows the rise time of ΔA signal for peak 1 along with the best fit function. The rise time of peak 1 is found to be, τ_r = 61 ± 16 fs. Figure 4.5 (b) shows the rise time of all 4 peaks in the NIR spectral region. The rise time of the bleaching signal increases with energy.

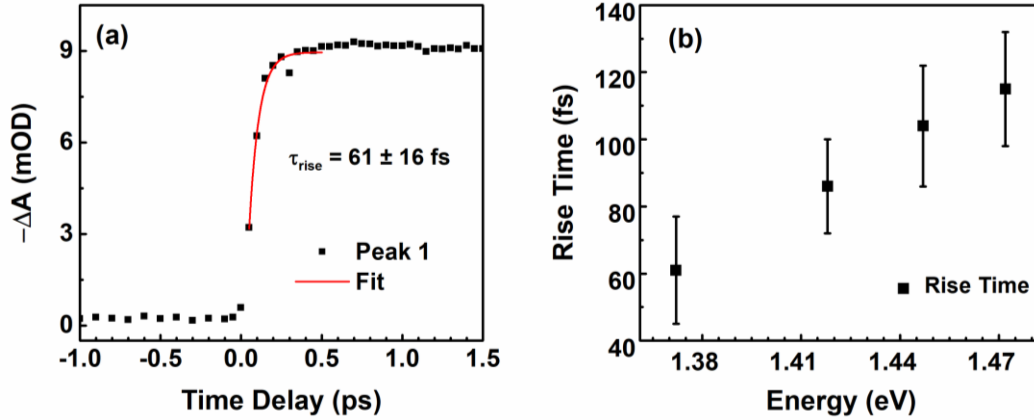

Figure 4. 5. (a) Time dependence of ΔA showing the rise time for peak 1 along with the best fit; (b) The rise time for all the four peaks in the NIR region of the spectra. The NWs were excited at 1.9 eV with a fluence of 318 µJcm^{-2}.

FTAS measurements were also done using lower excitation fluences such as 31.8 µJcm^{-2}, 79.5 µJcm^{-2} and 159 µJcm^{-2}. The temporal and spectral analyses were done for all these measurements as well. The intensity of ΔA signal increases with increasing fluence, this is due to increased carrier injection to the conduction band at higher fluences. The peak positions did not show any significant change with the changes in the excitation intensity. However, the dynamics of the bleaching signals changed significantly with the excitation intensity. The details of the temporal analysis as a function of the excitation fluence are shown in Figure 4.6. For the lowest excitation intensity (31.8 µJcm$^{-2)}$, the decay time was fit better with a single exponential decay function instead of the double decay function. Figure 4.6 (a) shows the dependence of the faster decay component, τ_1 on the excitation fluence. The decay time tends to decrease with increasing fluence, this is true for both τ_1 and τ_2. The decay times of peaks at higher energies were shorter than their corresponding values for lower energy peaks for all the excitation fluences. Another major difference is in the risetime of the bleaching signal. For the lowest excitation fluence (31.8 µJcm^{-2}), the risetime was fit with a double exponential growth function. For all higher excitation intensities, risetimes were fit with a single exponential growth function. Figure 4.6 (c) shows the double exponential fit for extracting the risetime for peak 1 for measurements with a fluence of 31.8 µJcm^{-2}. The risetime has two components, a fast component of $\tau1_{rise} = 80 \pm 30$ fs, and a slow component of $\tau2_{rise} = 687 \pm 135$ fs. Figure 4.6 (d) shows the dependence of the risetime for all the 4 peaks on the excitation fluence. At all fluences, the risetime was longest for peak 4 (highest energy) and shortest for peak 1(lowest energy). There was no significant trend in the risetime with fluence.

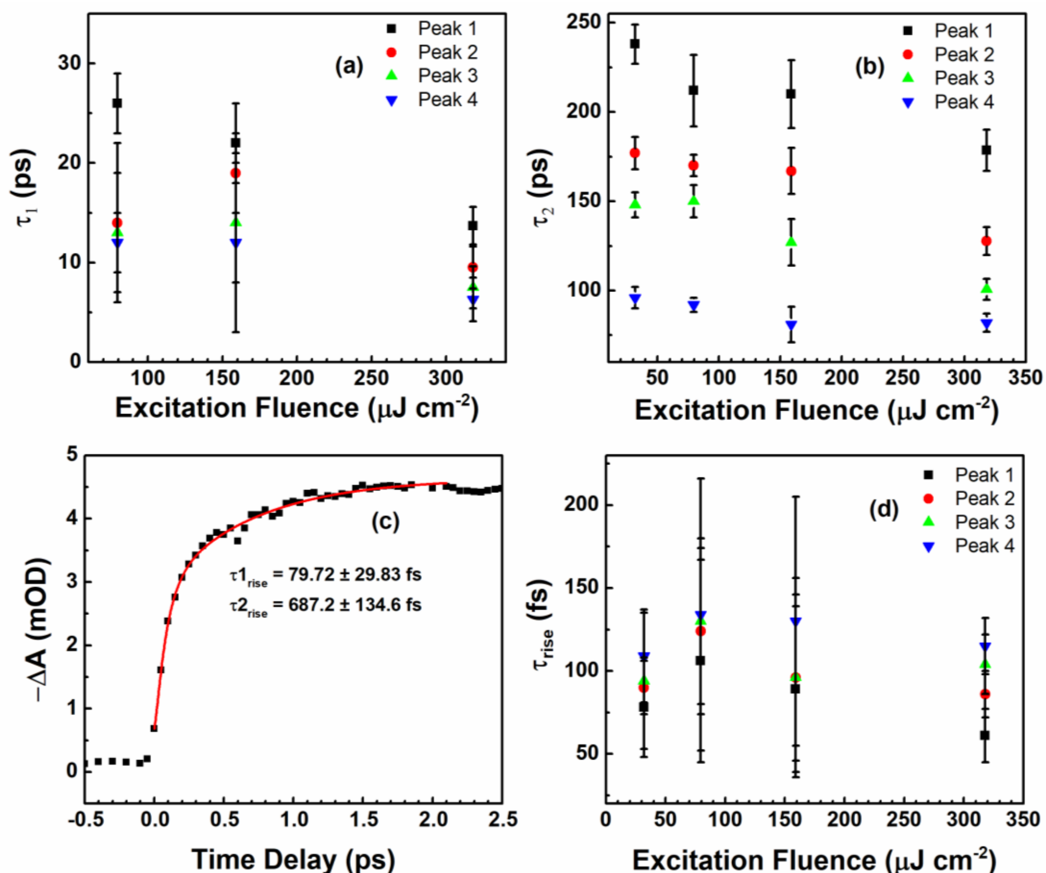

Figure 4. 6.(a)Fast and, (b) slow decay time constants of the four peaks as a function of excitation fluence; (c) The plot of ΔA as a function of delay time along with best fit to show the rise time of the bleaching signal, for peak 1 at excitation fluence of 31.8 μJ cm^{-2}; (d) Risetime of the bleaching signal for the four peaks as a function of the excitation fluence.

Figure 4.7 shows the normalized ΔA as a function of delay time for all the 4 peaks measured at all fluences. Black, red, green, and blue data points represent the fluences of 31.8 μJ cm^{-2}, 79.5 μJ cm^{-2}, 159 μJ cm^{-2} and 318 μJ cm^{-2} respectively. With increased fluence the decay time is reduced in general, and the curves are closer together meaning the difference in decay times is smaller at higher excitation fluences. For risetime however, the values remain similar except for 31.8 μJ cm^{-2}, where the bleaching signal has a two-step growth for all the 4 peaks.

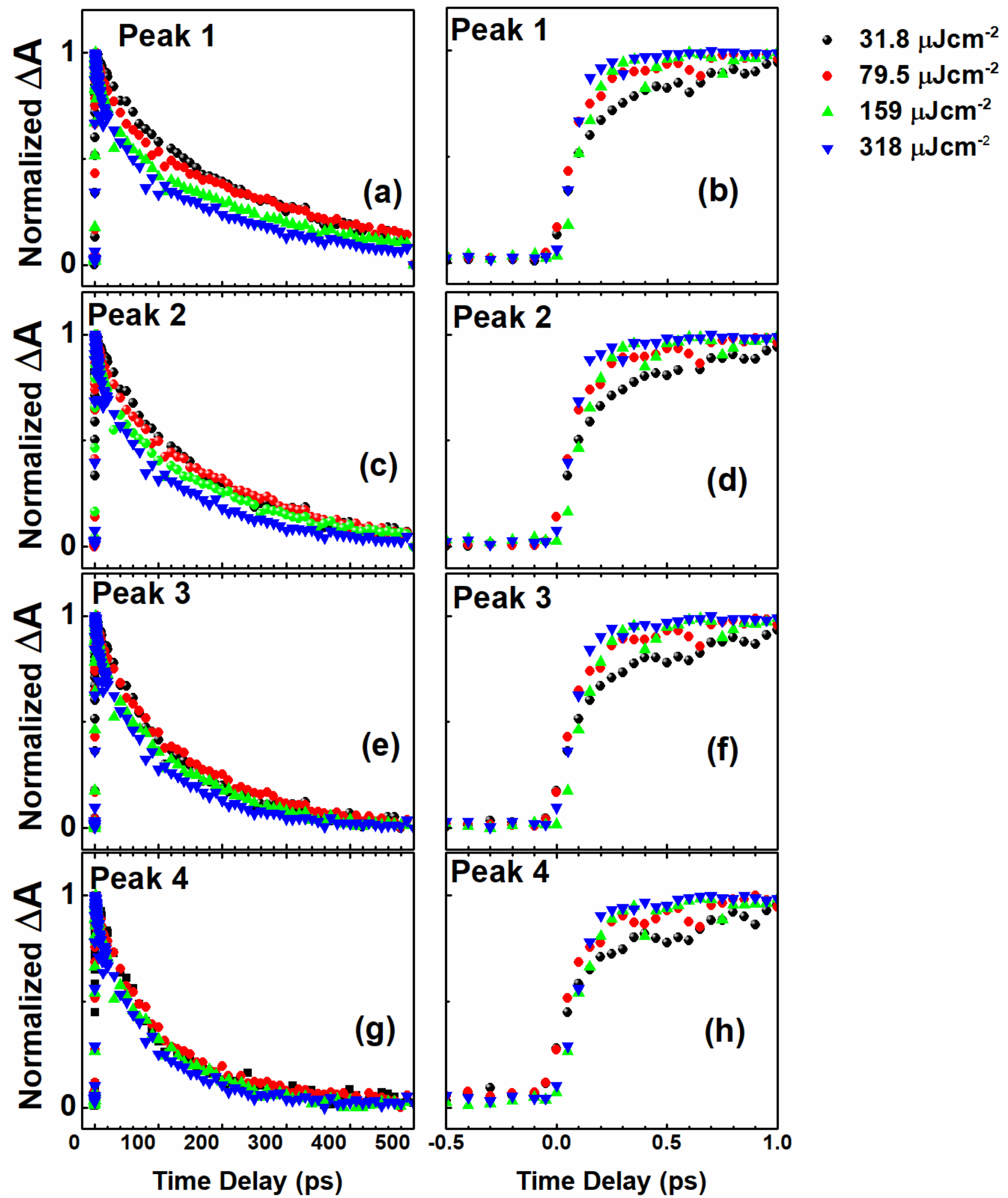

Figure 4. 7. Normalized ΔA as a function of delay time for (a) and (b) for peak 1; (c) and (d) for peak 2; (e) and (f) for peak 3; (g) and (h) for peak 4; Black, red, green and blue colours represent the different fluences 31.8 μJ cm^{-2}, 79.5 μJ cm^{-2}, 159 μJ cm^{-2} and 318 μJ cm^{-2}, respectively.

4.1.2.3 Fast transient absorption in the visible region of the spectrum

To study the excitonic transition C, i.e., the transition from C valence band to the first conduction band, in WZ InP, room temperature FTAS measurements were carried out using a visible probe. To excite the NWs, a pump with energy 2.25 eV was used. Choosing a pump with sufficiently high energy allows one to study the dynamics of the high energy tail of the TA signal. Information regarding the hot carriers and their cooling rates can be extracted by carefully studying the high energy tail of the TA bleaching signal. The results of the FTAS at room temperature using a fluence of 318 μJ cm^{-2} are shown in Figure 4.8. A bleaching peak is observed at ~ 1.6 eV, corresponding to the transition C energy in the false colourmap shown in Figure 4.8 (a). The TA map consists of negative bleaching signal around the gap energy (~1.6 eV) and becomes increasingly positive at higher energies. Figure 4.8 (b) shows the dynamics of the TA signal at 1.6 eV along with best fitting function. The decay signal was fit with a single exponential function. A decay time constant of $\tau_{decay} = 16 \pm 1$ ps was extracted from the fit. The bleaching signal moves from negative to positive after 50 ps, so the fitting is done only up to 50 ps to determine the decay time constant of the absorption bleaching. Figure 4.8 (c) shows the TA at different time delays. Also, the TA signal goes from negative to positive at higher energies with increasing time delay. ΔA becomes positive at 50 ps for 1.6 eV, and at 0.2 fs for 2 eV.

After pump excitation with 2.25 eV, 1.6 eV of this absorbed energy is used for the transition C of the WZ structure, creating energetic carriers in the conduction band. After the initial dephasing from the pump excitation, in the next few hundreds of femtoseconds, through carrier-carrier scattering, the carriers form a thermal distribution defined by a $T_C > T_L$. In this hot-carrier regime, using the TA spectra at different time delays as shown in Figure 4.8 (c), we can extract the T_C at different time delays. To ensure that the carriers have achieved a thermal distribution, only the TA spectra after a time delay of 300 fs are used for the T_C extraction. The high energy tail of the bleaching signal centered around 1.6 eV is fit with a Boltzmann distribution at each delay time, and the temperature at each of these delay times is extracted from the fits. The evaluated T_c values at different time delays are shown in Figure 4.8 (d).

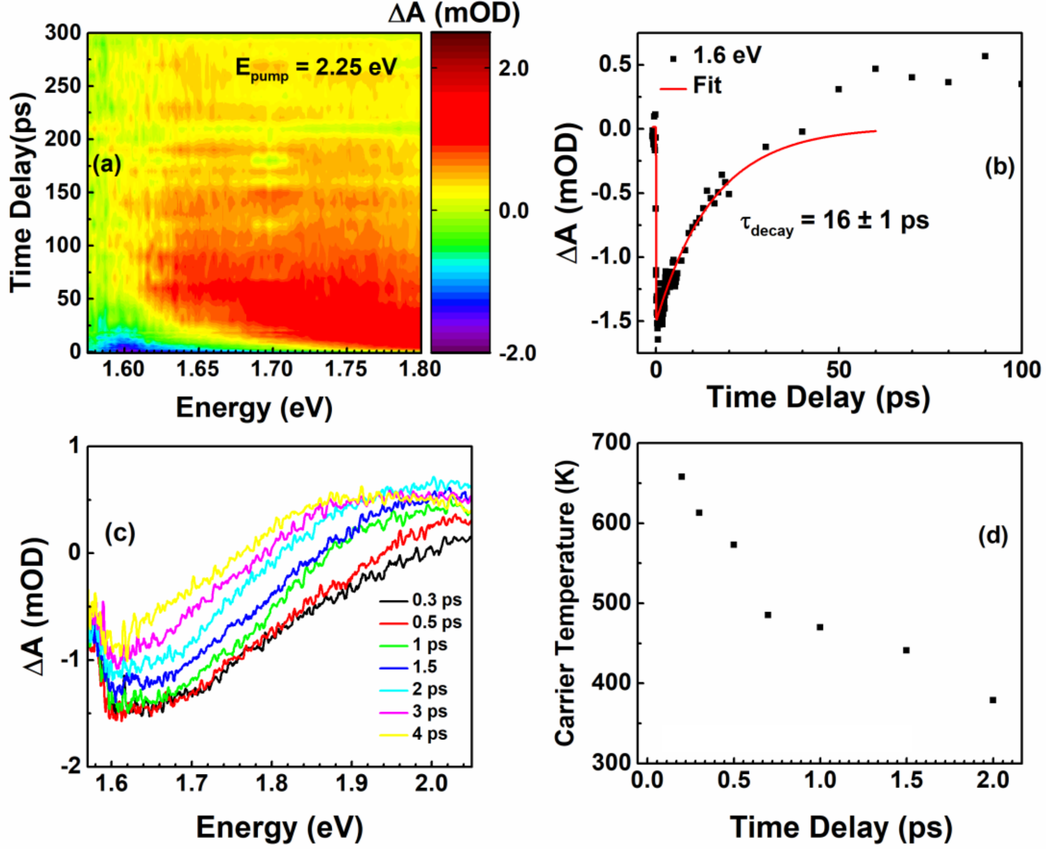

Figure 4. 8. (a) 2D false colourmap of FTAS measurements at room temperature where the x axis represents the probe energy and the y axis represents the time delay between the pump and the probe; (b) Dynamics of bleaching signal at 1.6 eV, along with the best fitting function to determine the decay time constant; (c) TA signals at different delay times; (d) T_C extracted from TA signal at different delay times. All measurements were done using a pump at 2.25 eV and a fluence of 318 $\mu J\ cm^{-2}$.

When the T_C values at different time delays are extracted one can calculate the rate of loss of hot carrier energy, J_C as,

$$\frac{dE}{dt} = J_C = \frac{3}{2} k_B \frac{dT_C}{dt} \qquad (4.1)$$

Using numerical differentiation on the different T_C values obtained at different time delays, J_C is plotted as a function of T_C in the Figure 4.9 below. Initially, the carriers lose their energy at a steady and fast rate, and once the T_C approaches 460 K there is a decrease in the magnitude of hot carrier energy loss rate. Yong *et al.*[55] have observed similar behavior while evaluating carrier cooling in WZ-ZB InP NW heterojunctions for NWs of diameters 50 nm and 160 nm. The NWs used in this thesis have a mean diameter of about 130 nm. They observed a reduction

in cooling rate around 600 K for 50 nm InP NWs and at about 450 K for 160 nm -InP NWs. In this case, for NWs of about 130 nm in diameter, the decrease in cooling rate is observed around 460 K. the initial fast cooling of the carriers is attributed to the coupling between carriers and LO-phonons. This cooling creates a thermal equilibrium between the LO-phonons and the carriers. Subsequently, the LO-phonons must then decay into acoustic phonons. If the temperature of the acoustic phonon bath is much higher than the T_L, then the carrier cooling rate is hampered. Here for 130 nm InP NWs this temperature appears to correspond to ~460 K, at which the phonon bottleneck takes place, leading to slower cooling of the hot carriers. At room temperature J_C = 0.05 eV/ps at 400 fs for InP, it drops two orders of magnitude at 1.5 ps (T_C ~460K) and then several orders of magnitude after 4 ps (T_C ~ 380 K).

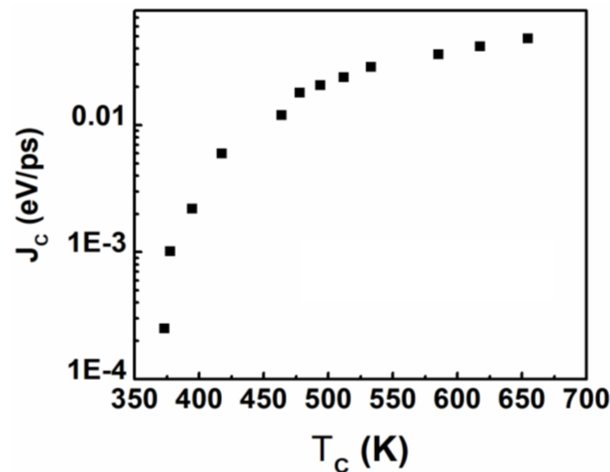

Figure 4. 9. Energy loss rate of hot carriers (J_C) plotted as a function of carrier temperature T_C, for InP NWs with respect to the WZ C-transition band when excited with a pump at 2.25 eV with a fluence of 318 μJ cm^{-2}.

To verify if the slowdown of energy rate is due to heating of the acoustic phonon bath temperature to a temperature much higher than T_L, the FTAS measurements were done at 77 K. Figure 4.10 below shows the 2D false colourmap of the FTAS measurements at 77 K using a pump of 2.25 eV and 318 μJ cm^{-2}. When the T_L is lowered to 77 K, the energy loss rate is decreased after 460 K. For 77 K the decrease is steeper than in room temperature measurements. At 77 K, J_C = 0.3 eV/ps initially for InP NWs at 300 fs and falls drastically after about 2.5 ps (T_C ~ 460 K). Using equations 1.4 and 4.1 for estimating the average rate of loss of energy, and using the value of LO phonon energy as 42.39 meV[112], the parameter τ_{LO} is estimated to be 0.35 ps when T_C =744 K. τ_{LO} is the characteristic time for carrier-LO phonon interaction.

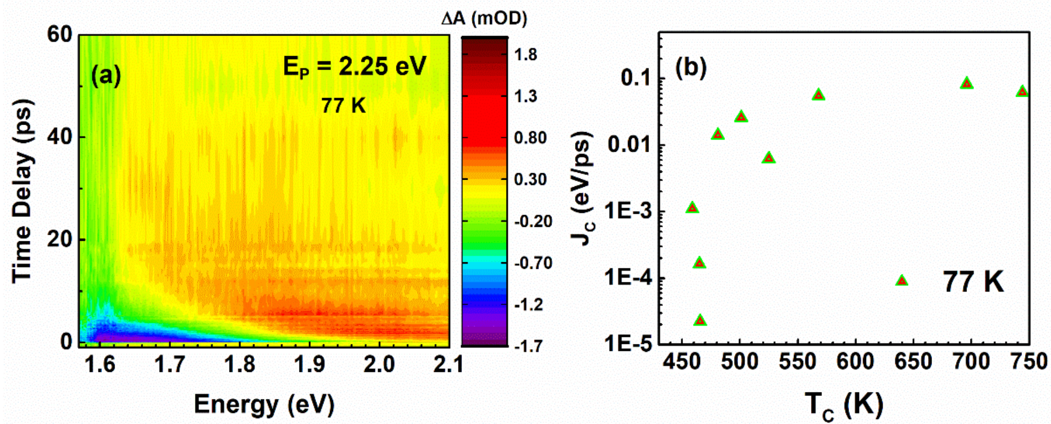

Figure 4. 10.(a) 2D false colourmap of FTAS at 77K for InP using a visible probe with energy on x -axis, and time delay on y-axis; (b) the energy loss rate of hot carriers extracted from the TA measurements as a function of T_C. The sample was excited using a pump at 2.25 eV with a fluence of 318 µJ cm^{-2}.

The FTAS measurements in the visible region of the spectra were also done using different excitation fluences. The results are summarized in Figure 4.11. As the excitation fluence decreased, the negative signal crossed to positive signal much faster and hence, the decay time is much shorter. The decay times were found to be τ_{decay} = 2.7 ± 0.4 ps and τ_{decay} = 0.85 ± 0.23 ps for 159 µJcm^{-2}and 79.5 µJcm^{-2}, respectively, for the bleaching signal at 1.6 eV. For 79. 5 µJcm^{-2}, the zero crossing of ΔA where the bandgap bleaching changes from negative to positive takes place at about 4 ps. For a fluence of 159 µJcm^{-2}, the zero crossing takes place at about 10 ps. Hence, from power dependent measurements using same pump energy, one can see that the ΔA goes from negative to positive at a faster rate for lower excitation fluences.

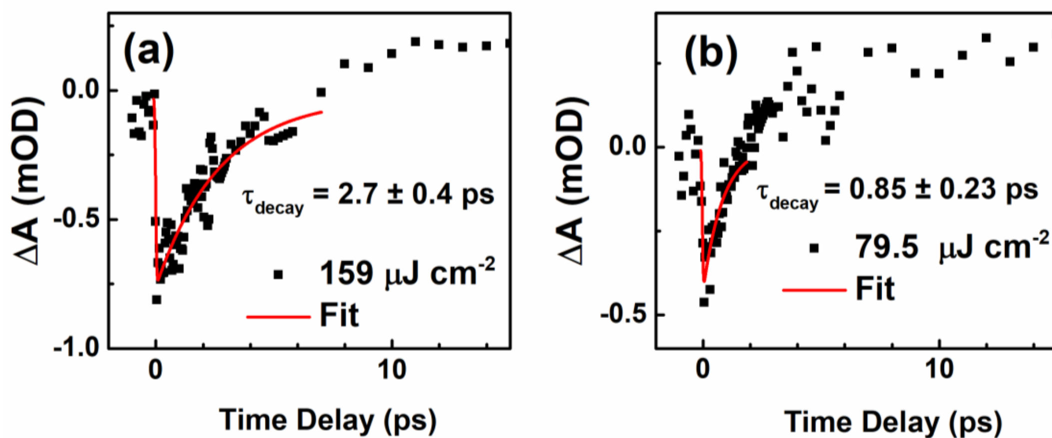

Figure 4. 11. Dynamics of the absorption bleaching at 1.6 eV when excited by a 2.25 eV pump with an excitation fluence of (a) 159 µJcm^{-2} and (b) 79.5 µJcm^{-2}. The red curves represent the best fit function.

To better compare the measurements in the visible spectral region with the measurements in the NIR, FTAS measurements in the visible were also done using a pump at 1.9 eV. Figure 4.12 shows the TA measurements performed using a 1.9 eV pump with two different fluences. Figure 4.12 (a) and (c) show the 2D colourmap of the TA with fluences of 318 μJ cm^{-2} and 159μJ cm^{-2}, respectively. Both measurements show a negative bleaching centered around 1.6 eV, followed by a high energy tail. The signal becomes positive at longer delay times in both cases. The respective decay times are extracted by fitting with a single exponential curve. The decay constants are τ_{decay} = 26 ± 4 ps and τ_{decay} = 30 ± 3 for 318 μJ cm^{-2} and 159 μJ cm^{-2}, respectively.

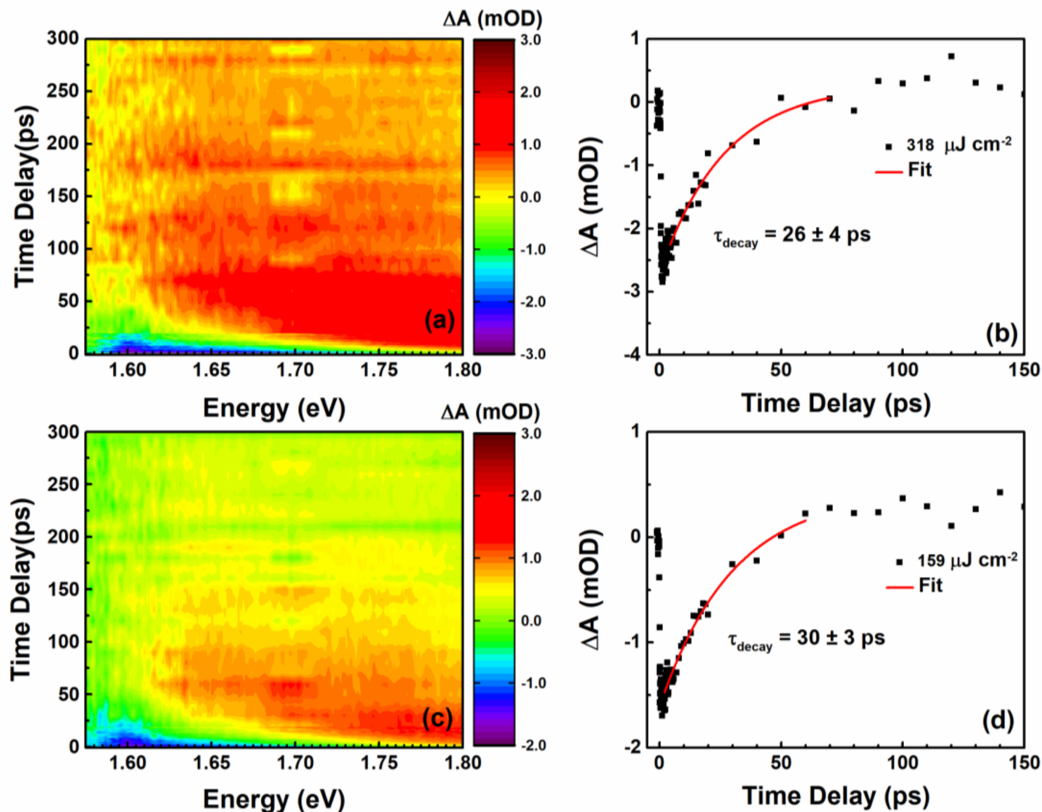

Figure 4. 12. Room temperature FTAS measurements of InP NWs using visible probe, and pump of 1.9 eV. (a) The 2D false colourmap of TA signal when excited with a fluence of 318 μJ cm^{-2} and (b) shows the corresponding dynamics of bleaching signal at 1.6 eV. (c) The 2D false colourmap of TA signal when excited with a fluence of 159μJ cm^{-2} and (d) shows the corresponding dynamics of bleaching signal at 1.6 eV

Here too, the value of ΔA changes from negative to positive as a function of time delay. The time delay at which the ΔA crosses zero is also a function of the probe energy. When pumped

at 1.9 eV with a fluence of 318 μJ cm^{-2} the ΔA goes from negative to positive at 1.6 eV in 80 ps and at 1.8 eV in 2 ps. Similarly, for the same pump, with a fluence of 159μJ cm^{-2} ΔA goes from negative to positive at 1.6 eV in 50 ps and at 1.8 eV in 0.3 ps.

4.1.3 Discussion

Through the optical measurements of InP NWs, different photoinduced processes in InP were studied. The presence of both WZ and ZB structures in the InP NWs are first observed using μ-PL measurements. Luminescence corresponding to both ZB fundamental bandgap energy, and WZ- A transition, i.e., from valence band A to the first conduction band, energy are identified at 1.418 eV and 1.492 eV, respectively, and these values agree with the literature.[100,111,112] Through FTAS, the temporal and spectral behavior of the InP NWs in both NIR and visible spectral region were probed. For the TA absorption spectra at room temperature, 5 different peaks are observed. By comparing these values with literature, one can try to assign these values to their corresponding electronic transitions. Zilli *et al.* have performed temperature dependent PL excitation (PLE) and PL measurements of WZ InP NWs as well as ZB InP NWs.[105] In *Table 4. 2*, given below, a comparison is drawn between the peak energies obtained by the fit of the FTAS results in this work with the energies observed at 250 K and at 310 K for the PLE and PL peaks. This comparison with Zilli *et al*. is drawn because the samples used for measurements are from the same growth and also Zilli et al. presents temperature dependent measurements which is easier for comparison with our room temperature data.

Table 4. 2. Assigning the observed peaks by comparing values with the literature.

Peak	**Our data**	**Peak position in literature for PLE at 250 K**	**Peak position in literature for PLE at 310 K** [105]
A to CB1	1.418 eV	1.44 eV [105]	1.42 eV
B to CB1	1.464 eV	1.48 eV [105]	1.46 eV
C to CB1	1.6 eV	1.62 eV [105]	1.58 eV
ZB	1.37 eV	1.36 eV [105] (PL)	~1.35 eV (PL)
ZB + SO	1.472 eV	~ 1.47 eV[113] (TRS measurements)	

The peak at the lowest energy (peak1) in the NIR is assigned to the ZB fundamental bandgap. The value I have observed is 1.37 eV which is larger than 1.35 eV observed by Zilli *et al.*[105] at 310 K. Apart from a possible error in the determination of the peak position, the difference between the FTAS and the PL values could be related to the Stokes shift because of the presence of some disorder in the NWs. The presence of a Stokes shift is supported by the observation that the position of the higher energy transitions agrees very well with those determined by Zilli *et al.* using PLE, which reflects the absorption of the material. Moreover, Mishra *et al.* have observed that at high temperature the PL values of ZB InP NWs are slightly higher and deviates from calculated temperature dependence of bandgap energy using Varshni equation.[104] The value observed in that case is close to 1.37 eV. The reason for this deviation is not clear yet. From the comparison with the PLE data found by Zilli *et al.*, we can assign Peak 2 to the WZ A transition and peak 3 to the WZ B transition. Similarly, the fourth peak observed in the NIR region and the peak at 1.6 eV can be assigned to the ZB+SO and to the WZ C transition, respectively.

The ΔA is negative for most of the probe energies due to the filling of states in the conduction band by electrons upon pump excitation, leading to depopulation of the valence band and hence resulting in reduced absorption of the probe by the carriers. In the visible part of the spectra, however, there is a positive ΔA signal, which becomes more significant at higher energies. This may be assigned to the excited state absorption when the carriers in excited state reabsorbs the probe pulse and move to states with higher energy. The nature of the positive signal is dependent on both the pump energy as well as pump intensity or fluence. The positive signal is very long temporally, and since it is dependent both on the pump intensity and pump energy, the free carrier intraband absorption might have also contributed to its presence.

The temporal analysis of the TA spectra helped to study the dynamics of different electronic transitions in ZB as well as WZ InP NWs. The decay time for the ZB fundamental bandgap bleaching was found to be the longest of all the transitions. The bandgap bleaching signal decay in the NIR spectral region was fitted with a double exponential function. The decay times for all the peaks were dependent on the pump fluence: the decay times became shorter with increasing pump fluence. For the highest pump fluence (318 $\mu J\ cm^{-2}$), the fast component of the double exponential decay function gave a decay time constant, τ_1, in the range of 10 ps. And a slower decay time constant, τ_2, in the range of 50 ps – 200 ps. The initial fast component may be assigned to the carrier cooling due to interaction with the optical phonons. The LO phonons then decay by the production of acoustic phonons. However, in the case of InP, due to a large gap in the phonon dispersion curve, the LO phonon cannot directly decay into the LA phonon.[114] Therefore, it decays into a TO and an acoustic phonon mode, which further decays into two LA modes,[113] thus increasing the effective time in which the carriers can further cool down. During this time the carriers could even re-absorb the hot phonons and further slowdown the decay process as mentioned in Chapter 1.

The temporal analyses of the bleaching signal in the visible spectral region showed that the decay of the WZ C transition signal was best fit using a single exponential decay curve, unlike the signals in the NIR. In this case, after about 50 ps the bleaching signal becomes positive. Hence, fitting was only done where ΔA is negative. For a pump at 2.25 eV, the decay constants for WZ C signal were found to be 16 ps, 2.7 ps and 0.85 ps for fluences of 318 $\mu J\ cm^{-2}$, 159 $\mu J\ cm^{-2}$ and 79.5 $\mu J\ cm^{-2}$, respectively. When the same samples were excited using a pump at 1.9 eV, the decay times were found to be around 26 ± 4 ps and this bleaching at 1.6 eV crosses from negative to positive in about 80 ps. An important observation is that the decay time decreases with increasing energy of the transition. For the rise time, higher energy peaks showed a higher value indicating that the carriers take longer to undergo a high energy transition.

The FTAS measurements in the visible region have enabled the evaluation of T_C as a function of delay time. The T_C of the carriers with respect to the WZ C transition were evaluated. The electrons (holes) were hot with respect to the conduction (valence) band edge for the WZ C transition. After calculating the T_C cooling rates, the energy loss rate was also calculated. Initially, the carriers cool down fast by interaction with the LO phonon, bringing thermal equilibrium between the hot carriers and the LO-phonons. Then the LO-phonons decays into acoustic phonons. At high excitation intensities, like in the case here, there will be a strong amplification of the carrier-LO phonon interaction, leading to the creation of non-equilibrium phonons. Further cooling is dependent on the LO phonon decaying into acoustic phonons. The fast decay of the LO phonons result in the non-equilibrium population of acoustic phonons. The partial heating of the acoustic phonon bath further slows down the cooling of hot carriers. The acoustic phonon decay is strictly controlled by heat diffusion interactions with the enviroment.[115] The data obtained in this thesis agrees with the observations made by Yong *et al.*[55] where they have shown that the hot carrier cooling is hampered due to LA phonon bottleneck. They have shown that the LA phonon bath temperature is around 600 K for 50 nm diameter InP NWs and 400 K for 160 nm diameter InP NWs. The value obtained in this thesis for 130 nm diameter InP NWs is around 460 K, which agrees with the literature value. The LO-phonon scattering time for $T_C = 744$ K is evaluated to be about 0.35 ps for measurements at $T_L = 77$ K.

4.2 Ultrafast spectroscopy of GaAs using a visible probe

In the second part of this chapter, I present the data obtained through the FTAS of GaAs NWs using a visible probe. In this case the GaAs NWs have a ZB structure as they have been grown by the self-catalyzed method.[116]

By performing FTAS in the UV-Vis region it is possible to observe bleaching signal corresponding to critical points of the joint density of states, commonly called E1 and E1 + Δ at energies in the range between 2.75 and 3 eV.[117–120]. Usually, it is very difficult to distinguish the E1 and E1 + Δ transitions in steady-state absorption because of the very high absorption coefficient of GaAs in that energy range. FTAS being a differential method, allows the measurement of small changes of the absorbance and has allowed me to observe the dynamics of the absorption bleaching observed at the characteristic energies. To the best of my knowledge, this thesis reports the first observation of absorption bleaching at the E1 and E1 + Δ critical points in GaAs. Therefore, NWs appear to represent a useful mean to study optical properties otherwise not reported in the bulk using this method.

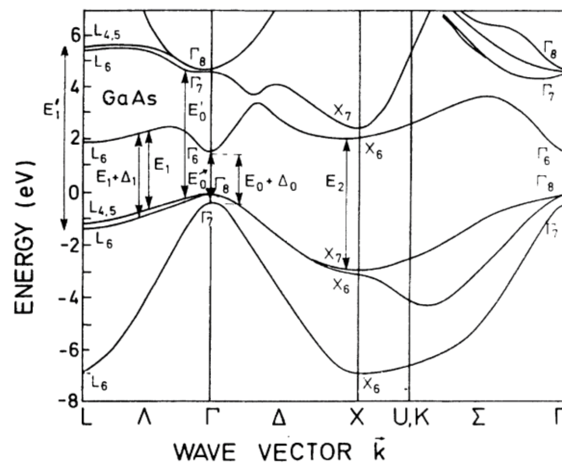

Figure 4. 13. Band structure of GaAs showing critical points reprinted with permission from P. Lautenschlager et al. [121] (1987) by the American Physical Society.

Figure 4.13 taken from Lautenschlager *et al.*[121] shows the band structure of GaAs with the main critical points marked. The first critical point is E_0, the fundamental bandgap of GaAs, and the second one is $E_0 + \Delta$, which corresponds to the fundamental gap plus the spin-orbit split off correction. The next critical point is E1 and followed by E1 + Δ. They are located along the Λ lines of the Brillouin zone. The most common method used to study the E1 and E1 + Δ transitions are ellipsometric measurements, and reflectance measurements.[90] The knowledge

of these critical points helps us have a clear idea about the dielectric function of the material, and hence become important in several electronic device applications.

4.2.1 Material

The ZB NWs are self-catalyzed. The wires were grown in the temperature range of 580-615^{0}C. More detailed description of growth can be found in Ambrosini *et al.*[116] The NWs were provided by Dr. Silvia Rubini from TASC-IOM-CNR laboratory in Trieste, Italy.

4.2.2 Optical characterization

The NWs were mechanically transferred to a transparent quartz substrate for FTAS measurements at room temperature. The TA measurements were done with a probe in the energy range 3.3 eV -1.5 eV using different pump energies to excite the samples.

4.2.2.1 FTAS of ZB GaAs NWs using a visible probe

Figure 4.14 presents the visible FTAS on GaAs NWs using a pump at 4.51 eV and fluence of 159 μJ cm^{-2}. Figure 4.14 (a) shows the 2D false colourmap of ΔA as a function of probe energy and time delay. In this case both E1 and E1 + Δ are observed in the form of negative absorption bleaching. The value of E1 is found to be around 2.8 eV and E1 + Δ is observed at ~ 3 eV. The E1 signal has a short decay constant of about 3 ps and a long decay constant in the order of hundreds of picoseconds. Figure 4.14 (b) shows the TA at 3 different time delays. The E1 peak undergoes a significant blue shift with increasing time, but for the E1 +Δ signal only a small shift is observed. The dynamics of E1 + Δ, was impossible to determine due to high noise to signal ratio for this signal. The black line in the colormap of TA spectra corresponds to the second order of the pump in the monochromator during measurements and has no significance.

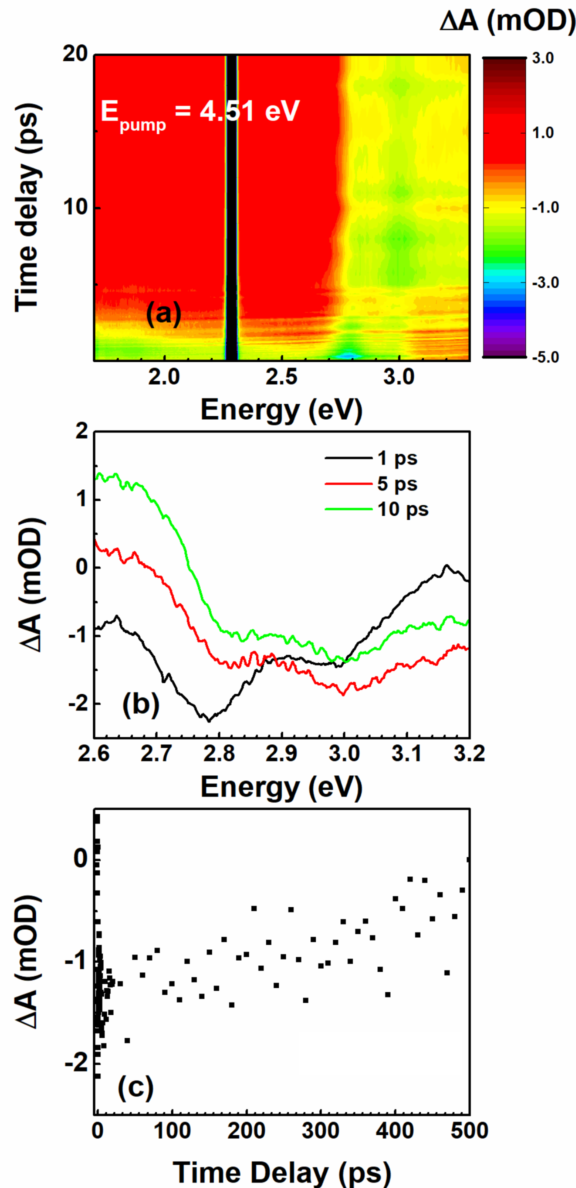

Figure 4. 14. (a) 2D false colourmap of visible FTAS of GaAs NWs, the x axis shows the energy in eV and y axis shows the time delay in ps, with the colors indicate the signal intensity.; (b) TA spectra at different time delays; (c) ΔA at 2.8 eV as a function of time delay. The NWs were excited with pump of energy 4.51 eV and fluence of 159μJcm^{-2}.

Another feature of the TA signals in the visible region is a broad negative bleaching from 2.6 eV down to the NIR. This signal is negative until the first 5 ps and then becomes positive in nature. This feature is shown in Figure 4.15 This signal could be an induced absorption of the photoexcited carriers. This positive signal then recovers in about 0.5 ns.

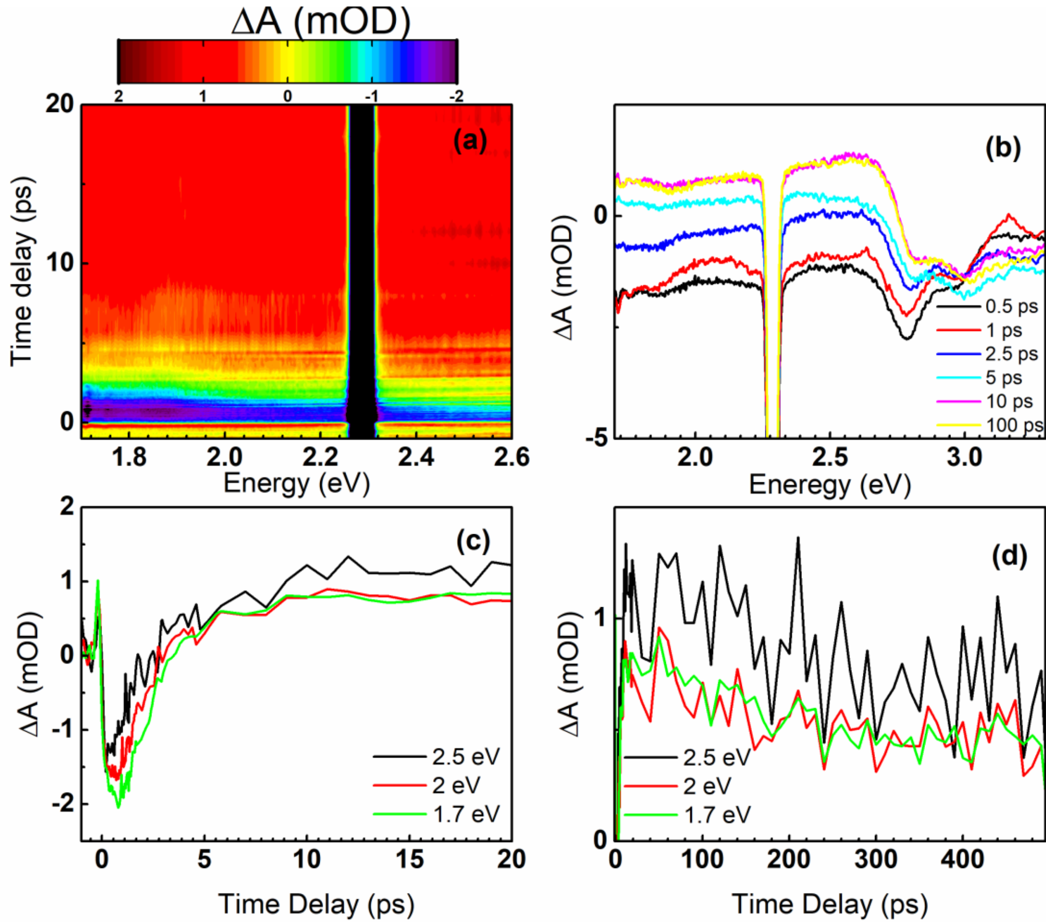

Figure 4. 15. (a) 2D false colourmap of visible FTAS of GaAs NWs, the x axis shows the energy in eV and y axis shows the time delay in ps for the probe region between 1.72 eV and 2.6 eV.; (b) TA spectra at different time delays in the visible region; (c) ΔA as function of time delay until 20 ps;(d) ΔA as function of time delay until 500 ps. The NW samples were excited with pump at 4.51 eV and fluence of 159μJcm^{-2}.

Similar measurements were also done with the help of a pump below the energy of E1 transition. For this measurement, a pump of energy 2.25 eV was used with a fluence of 159 μJcm^{-2}. The results are summarized in Figure 4.16. Similar to what we observed in Si NWs with excitation below the E1 energy, the signals corresponding to the E1 transition and E1 + Δ are observed in the visible spectra. The signal is very noisy, and the dynamics are hard to fit. For excitation using a small pump energy, there is a small blue shift of the signal.

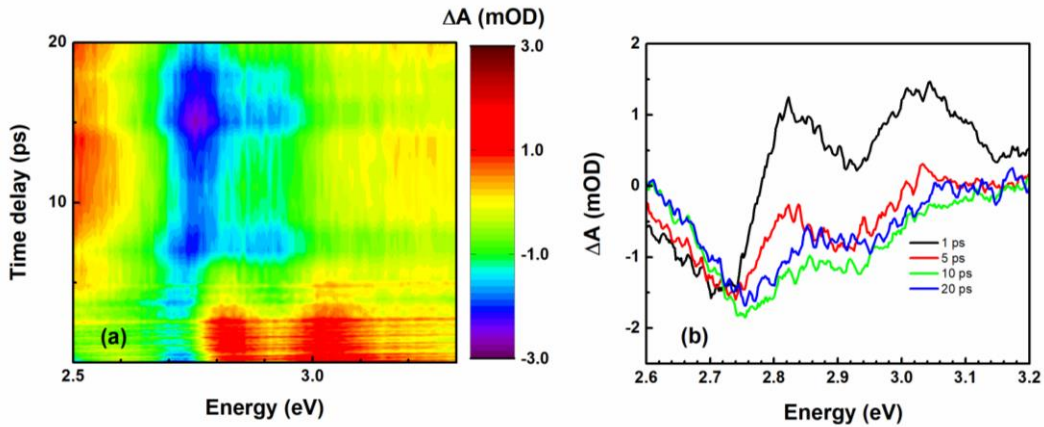

Figure 4. 16. 2D false colourmap of visible FTAS of GaAs NWs, x axis shows energy in eV and y axis shows time delay in ps.; (b) TA spectra at different time delays. The NWs were excited using a pump at 2.25 eV with fluence of 159 μJcm^{-2}.

4.2.3 Discussion

In the second section of this chapter on III-V semiconductors, the visible FTAS of GaAs NWs of ZB structure was studied. By performing FTAS with visible probe, two critical points E1 and E1+Δ in the bandgap of GaAs are observed. For ZB structures, E1 and E1 +Δ are observed at 2.8 eV and 3 eV, respectively. The critical points are usually analyzed through ellipsometric studies. These points give important information about the dielectric constant of the material. This work presented the novel observation of the critical points in the band structure of GaAs near the Λ point in the form of absorption bleaching. With time resolved measurements, it was also possible to see that the critical points undergo a blue shift with time after carrier excitation, suggesting that the band renormalization affects the whole band structure of the semiconductor and not only the levels corresponding to the lowest energy transition.

4.3 Diameter dependent carrier cooling in GaAsP nanowires

As the last case of III-V compounds, I have studied the TA spectroscopy of GaAsP NWs of two different diameters. This part is focused on the dependence of the rates of cooling of hot carriers in NWs on their diameter. It is clear also from this thesis that apart from being technologically versatile material systems, NWs also provide a great platform to study fundamental physical properties. Hot carrier cooling in semiconductors is strongly dependent on the nature of carrier-phonon coupling. As mentioned in the introduction, only a few works have been done to study the carrier cooling in semiconductor NWs. The existing literature shows that the carrier cooling rate efficiency has an inverse dependence on the diameter of the NW structure. In this chapter, I provide the first direct measure of the electron-phonon coupling rate for different NW diameters. In particular, I estimate the carrier cooling rates by measuring the carrier temperatures at different delay times after pump excitation in GaAsP NWs of diameters ~36 nm and 51 nm.

For this experiment, the NWs are provided from the University College of London (UCL)**.** The NWs of the ternary alloy, $GaAs_{(1-x)}P_x$, have $x = 0.2$ in this case. Because of the presence of the phosphide, the alloy has two modes of LO phonon frequencies the GaAs mode and the GaP mode. With the increase in phosphorous content, the intensity of the GaP mode increases, and the GaAs mode shifts to lower frequencies while the GaP mode shifts to higher frequencies. These behaviors are explained in Pistol *et al.*[122] We use the value of $x = 0.2$ and using the relations given in ref.[122]:

$$LO_{GaAs} = 291.1 - 25.5x \ \ cm^{-1} \qquad (4.2)$$

$$LO_{GaP} = 350.1 + 72.2x - 20.0x^2 \ cm^{-1} \qquad (4.3)$$

The LO phonon energies in meV are 35.46 meV and 45.1 meV for GaAs and GaP, respectively.

Similarly, the optical bandgap also changes with composition. The bandgap dependence of III-V semiconductor alloys on mole fraction, x, of a component is given by Thompson and Woolley[123] as, $E = A + Bx + Cx^2$. The bandgap can be tuned in visible and NIR range by changing the x value. GaP being an indirect bandgap material (with a minimum of the bandgap at the X point of the Brillouin zone) and GaAs a direct bandgap compound, $GaAs_{(1-x)}P_x$ will have an indirect or direct character depending on the value of x. The critical value at which $E_X = E_\Gamma$ is x ~0.45.[124] Below this critical value of x the ternary alloy is a direct bandgap material, as in our case.

4.3.1 Material

The ternary alloy compound of the form $GaAs_{0.8}P_{0.2}$ was grown by MBE on (111) Si substrates. The detailed growth conditions are explained in Zhang *et al.*[125] Figure 4.17 (a) and (b) show the scanning electron microscopy images of thin NWs with an average diameter of 36 nm and thick NWs with an average diameter of 51 nm, respectively. The thin and thick wires are denoted by names R11 and R13, respectively. The samples were grown by Dr. Yunyan at UCL.

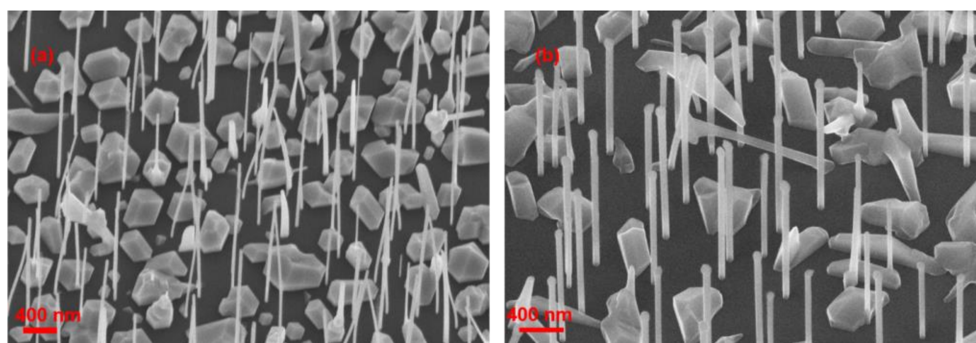

Figure 4. 17. 35^0 tilted SEM image of (a) thin (R11) and (b) thick (R13) GaAsP NW samples

4.3.2 Optical characterization

For the FTAS measurements, the NWs were transferred onto a transparent glass substrate. The NWs were excited using a pump at 2.88 eV of different fluences. The measurements were done at 77K using a liquid nitrogen cooled cryostat. The NW samples under study have a direct (Γ_8-Γ_6) bandgap around 1.7 eV and an indirect (Γ_8-X_6) bandgap around 2 eV. Immediately after pump excitation, the electrons are excited from the valence band to conduction band. In this case, the 2.88 eV creates energetic electrons in both the Γ and X conduction band valleys.

4.3.2.1 Photoluminescence of the GaAsP NWs

The PL of these NWs were carried out at UCL and the PL for the two samples are presented below in Figure 4.18. For the R11 sample, the band edge luminescence is narrow and distinct, while for R13, the band edge emission is present as a broad shoulder. Both the samples show defect band emission in the NIR region. The PL emission indicates that R13 samples may contain more defects or compositional inhomogeneity compared to R11 sample.

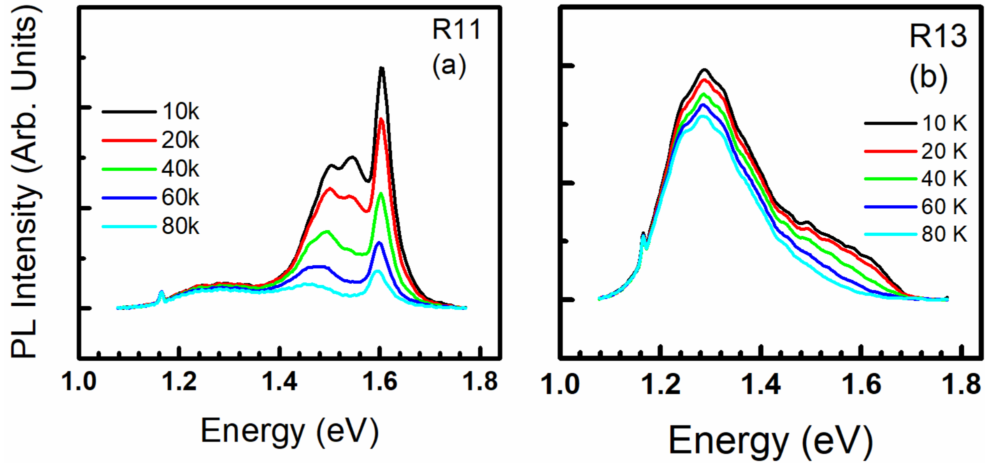

Figure 4.18. Temperature dependent PL of (a) R11 and (b) R13.

4.3.2.2 Raman measurements

Raman measurements were performed on both R11 and R13 to verify the quality of the crystallinity in the two samples. The results are presented below in Figure 4.19.

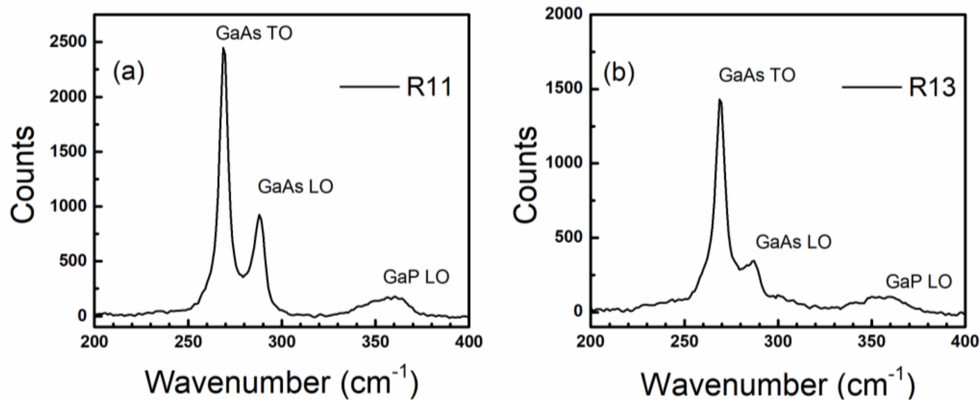

Figure 4.19. Raman spectra of (a) R11 and (b) R13 NW samples measured on as-grown samples.

For both the samples, there are 3 peaks present in the Raman spectra that are marked as 1, 2, and 3. Peak 1 is at 269.1 cm^{-1}, peak 2 at 287.8 cm^{-1} and peak 3 at 356.8 cm^{-1} corresponding to energies 33.36 meV, 35.68 meV, and 44.25 meV, respectively. Comparing with values in literature, the peak 1 is assigned to GaAs-like TO phonon, peak 2 is assigned to GaAs-like LO phonon mode and peak 3 is GaP-like LO-phonon.[122,126] From the Raman spectra it can be seen that R11 has a narrower, well defined and more intense peaks as compared to R13 for the same

excitation conditions. Associating this with the PL spectra one can say that R11 is of better crystalline quality.

4.3.2.3 Fast transient absorption of GaAsP NWs at 77 K

Figure 4.20 presents the results of the FTAS measurements at 77K for the GaAsP NWs transferred onto a quartz substrate. Figure 4.20 (a) and (b) show the 2D false colourmap of ΔA for R13 and R11 NW samples, respectively. The spectral analysis shows two absorbance bleaching peaks: a high intensity peak centered around 1.72 eV and a second, less intense peak centered around 2 eV. The peak at 1.72 eV corresponds to the Γ_8-Γ_6 transition, and the peak around 2 eV corresponds to the indirect Γ_8-X_6 transition. Using the calibration curve given in Thompson *et al.*[123] and the energy of the direct transition at 77 K measured with the FTAS (1.72 eV), the value of x is estimated to be around 0.17, which is in very good agreement with the nominal value given by the growth parameters. The indirect band gap relative to this alloy composition is then expected to be at 2.01 eV in excellent agreement with the energy position found in our FTAS measurements for the high energy peak. Figure 4.20 (c) shows the TA of the R13 and R11 at a time delay of 300 fs between the pump and the probe. The absorbance bleaching at 2 eV is more intense for R11 compared to R13 NW sample, and both samples show a clear bleaching at ~1.72 eV. The temporal analysis of the TA measurements is summarized in Figure 4.20 (d). The absorbance bleaching at 1.72 eV has a decay time constant of ~2.2 ps for both samples. With increasing energy, the separation between the decay times of R13 and R11 increases, and at 2 eV the decay time constants are ~500 fs for R13 and ~ 1.1ps for R11. Figure 4.20 (d) shows how the decay time constants are varying with energy for the two samples, clearly indicating that in sample R11 the decay is slower than R13 which is the thicker NW sample. This first observation points towards faster decay of the bleaching in thicker wires compared to thinner wires of the same composition. The faster decay in R13 could also point to more defect mediated recombination.

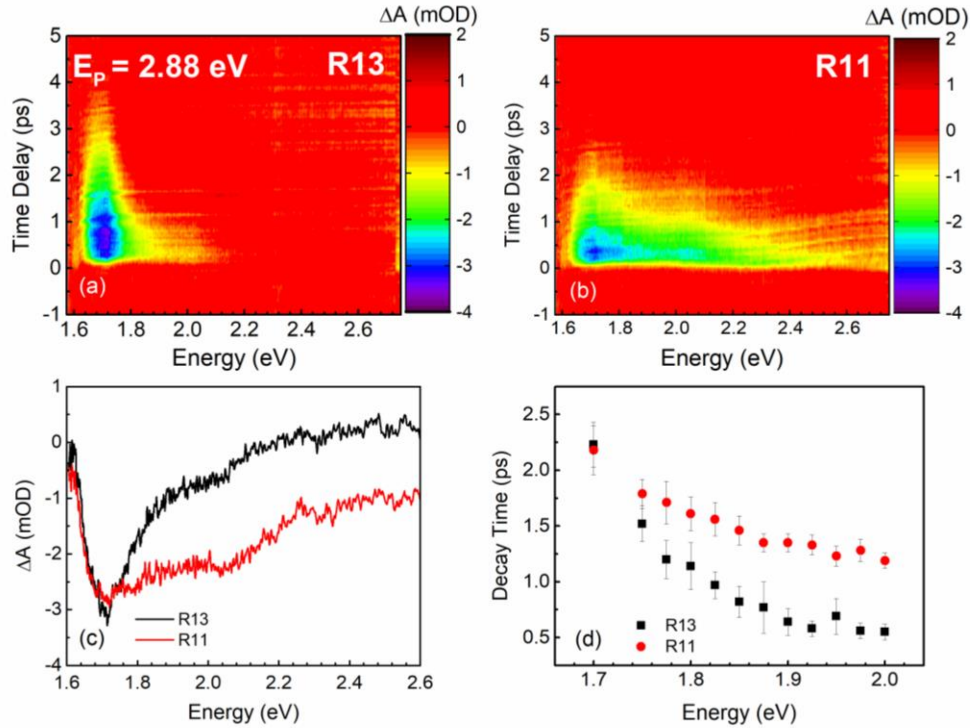

Figure 4. 20. 2D false colormap of ΔA at 77 K for: (a) R13, and (b) R11 samples pumped at 2.88 eV with fluence of 159 μJ/cm^2. The probe energy is depicted on the x-axis and the time delay between the pump and the probe is depicted on the y-axis; (c) TA spectra for R13 (black) and R11(red) samples at a time delay of 300 fs between the pump and the probe; (d) The decay time at different probe energies for R13 (black) and R11(red) samples.

The carrier temperatures are extracted by the analysis of the high energy tail of the TA spectra. The presence of the bleaching signal of the indirect transition limits the spectral range useful for the estimate of T_c. Moreover, since the decay times were faster than 500 fs for R13, an accurate fit is difficult at energies larger than 2 eV. Nevertheless, Figure 4.21 shows the ΔA signal as a function of time delay for R13 (black) and R11(red), for energies greater than 2 eV. For the sample R13, the bleaching signal above 2 eV is very weak, and decays faster than R11.

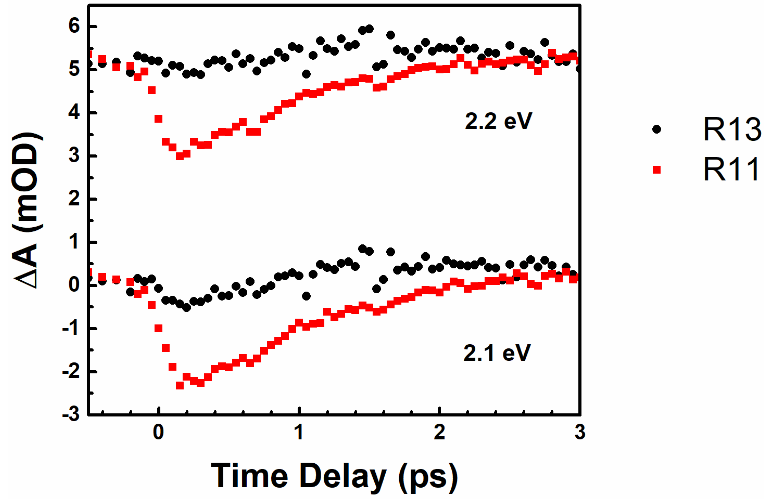

Figure 4. 21. Y offset plot of ΔA for R13(black) and R11 (red), for energies greater than 2 eV.

The carrier temperature extracted for energies greater than 2eV, with respect the Γ-X transition energy, is shown in the Figure 4.22 below.

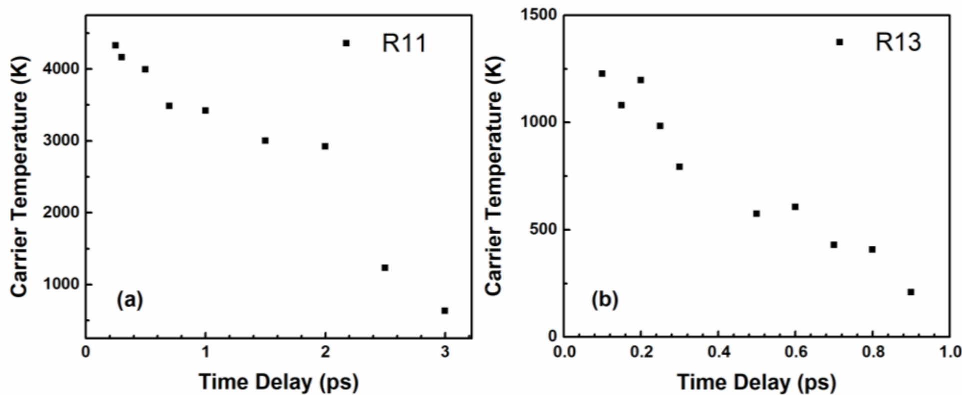

Figure 4. 22. T_C with respect to the Γ-X-transition in (a) R11 and (b) R13 NWs

The carrier temperature taken with respect to the Γ_8-X_6 transition shows that electrons are hot with respect to the X-valley bottom, and holes are hot with respect to the top of the valence band. For thin wires, R11, the highest T_C obtained is much higher than in the case of thick wires, R13. For R13, the highest temperature obtained was 1200 K, and that for R11 was 4300 K. From this observation, it is evident that thinner NWs attain higher T_C compared to thicker

NWs. Similar analyses were also done with respect to the direct Γ_8-Γ_6 transition. Here the carrier temperatures were only considered for time delays larger than 0.75 ps to avoid the rising of the signal at 2 eV from interfering with the fit of the high energy tail above 1.72 eV. This also ensures that we are extracting the carrier temperatures after the carriers attain a thermal energy distribution.

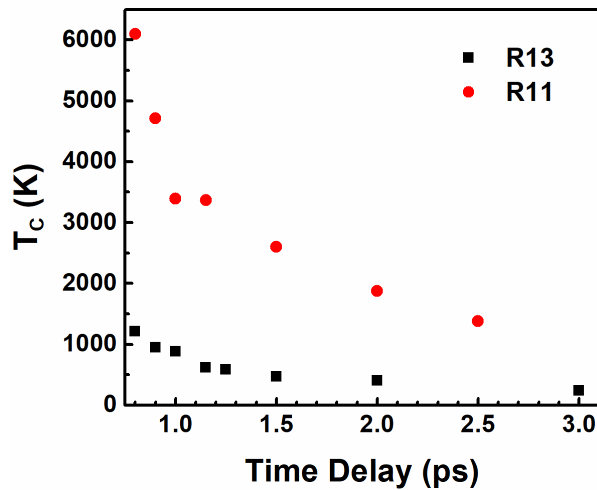

Figure 4. 23. T_C at different time delays for Γ-Γ transition for R11 (red) and R13(black) samples.

Figure 4.23 shows T_C as a function of delay time for both R11 and R13. Here too we can see that the carrier temperature of thinner wires is higher than that of the thick wires. Also, a single exponential decay function was used to fit temperature as a function of time delay, in the form of $T_c = A_0 * exp(-t/\tau) + T_0$, where the τ values for R11 and R13 are 0.5 ± 0.1 ps and 0.3±0.1 ps, respectively, implying that the decay is faster for R13.

The rate of hot carrier energy loss can also be given by,

$$\frac{dE}{dt} = J_C = \frac{3}{2} k_B \frac{dT_c}{dt} \qquad (4.4)$$

Like in the evaluation done for InP NWs of diameter 130 nm, the hot carrier energy loss rates were also calculated for R11 and R13. For this, the numerical differentiation of T_C was done as a function of time delay. Figure 4.24 below shows J_C as a function of T_C for the two samples.

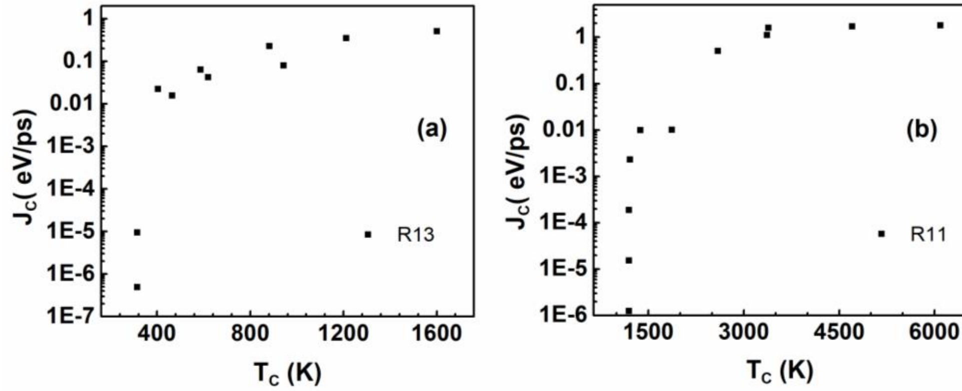

Figure 4. 24. J_C (eV/ps) evaluated as a function of T_C (K) for (a) R13 and (b) R11.

For R13, the carrier temperature does not rise as high as in R11. This observation is in agreement with Tedeschi *et al.*[58]. However, in their work they study the temperature of long-lived hot carriers through steady state PL. J_C values showed that for the thinner NWs, the carrier energy loss rate decreased by several orders of magnitude at about 1000 K, while for R13 the hot carrier energy loss rates plummeted after 350 K. The initial energy loss is rapid due to the efficient interaction with LO-phonons, which then decays to two counter-propagating LA phonons. The decrease in the energy loss rate is linked to LA phonon-bottleneck. The temperature at which the phonon-bottleneck takes place is dependent on the NW diameter. The smaller the NW diameter, the higher the T_C at which the phonon bottleneck is achieved, leading to an inverse dependence of carrier cooling rates on the NW diameter.

4.3.3 Discussion

The FTAS at 77 K of GaAsP NWs of two different diameters showed that the T_C obtained by carriers in a thinner NW is higher than that in a thicker NW for the same time delay. This was true with respect to both the direct and the indirect bandgap transition in the GaAsP NW samples. Another important evidence for faster carrier dynamics in thinner NW samples were shown by the decay dynamics of the ΔA signal as a function of the probe energy. At all probe energy values, the thick NW sample had decay time of ΔA ≥ decay constant in the thinner NW sample.

The T_C evaluation shows that for both the direct and indirect electronic transitions, the thinner NWs have a higher T_C compared to the thicker NW sample. An important aspect to study with the hot carrier cooling rates is the hot carrier energy loss rate. For thick NWs the initial J_C values were around 0.5 eV/ps, which after 350 K drops several orders of magnitude and hence T_C is sustained at this temperature for longer time delays. In thin NWs, the initial cooling rate

is ~1.5 eV/ps because of efficient carrier LO phonon coupling, and after about T_C ~ 1000 K this value falls several orders of magnitude. Because of this efficient coupling, there will be a buildup of acoustic phonons. These acoustic phonons then decay over several picoseconds which in turn reduces the hot carrier cooling rates. Hence, according to our observations, thin NWs sustain hot carriers effectively for longer delay times at a higher temperature.

Similar to the calculations done in InP NWs, using equation 1.4 the LO-scattering times, τ_{LO}, were also determined for GaAsP NWs. For R13 NWs using the LO phonon energy as 35.68 meV, at T_C =944 K, the τ_{LO} is found to be 0.3 ps and with T_C = 1600, the value of τ_{LO} is 0.05 ps. Similar evaluation for R11 NWs with T_C =1380 K gives τ_{LO} = 2 ps and with T_C = 3300 K gives τ_{LO} = 0.03 ps. This indicate a faster scattering for phonons when T_C is high, and falls as T_C decreases.

However, it is important to keep in mind that the effects of the defect densities, and other differences between the two NW samples are not taken into consideration in these evaluations.

4.4 Conclusion

In Chapter 4 I have carried out the ultrafast spectroscopy of NWs of III-V family. Three different materials were chosen with three different aims. The first material to be studied was InP, the TA spectroscopy revealed the spectral and temporal behavior of the photoexcited carriers. Both WZ and ZB homostructures were systematically studied as a function of pump energy and pump fluence. T_C with respect to the WZ C transition was also evaluated giving an idea about how carriers cool down to the lattice temperature as a function of time delay. The peak positions of all the electronic transitions were in good agreement with the values in literature. For WZ InP NWs, a positive TA signal was observed at higher energies whose presence is attributed to excited state absorption and absorption of free carriers. The T_C at which acoustic phonon bottleneck takes place was evaluated to be 460 K. For measurements at 77 K, the initial J_C for InP NWs was found to be 0.3 eV/ps and LO scattering time was about 0.35 ps when T_C = 744 K.

The second material to be studied was GaAs NWs. GaAs was studied with the aim of observing the critical points E1 and E1 +Δ with the help of an optical TA spectroscopy. The two critical points were clearly observable when excited using different pumps as well as fluences, even excited using a pump energy lower than that of the critical points. The positions of E1 and E1 + Δ were found to be 2.8 eV and 3 eV, respectively, in ZB GaAs NWs. This observation is of significance in terms of realizing the observation of the critical points in the band structure of GaAs through absorption spectroscopy.

The final part of this chapter dealt with the dependence of carrier cooling on the diameter in GaAsP NWs. The FTAS measurements made it possible to observe the direct and indirect transitions for GaAsP. For thinner wires it was possible to clearly observe the high energy peak, while for the thicker wires it was less prominent. T_C extracted from TA spectra shows that the carriers in the thin wires were at a higher temperature than those in thick wires at all time

delays. This was seen to be true for both the direct and indirect transitions. While calculating the hot carrier cooling rate, features of a phonon-bottleneck were observed. For NWs of diameter ~36 nm, the T_C at which the energy loss rate of carriers dropped significantly is ~1000 K and for NWs with diameter of ~ 51 nm, this temperature is found to be 350 K. The carrier cooling rates slow down at this temperature because of the heating of the acoustic phonon bath temperature to temperatures close to the T_C. After carefully analyzing the experimental data it was found that the thinner NWs sustained hot carriers longer at an elevated temperature, hence verifying the inverse relation of carrier cooling on the NW diameter. The initial J_C for thin wires was about 1.5 eV/ps and that for thick wires was around 0.5 eV/ps. In thin NWs the initial efficient coupling with LO phonons lead to a non-equilibrium production of hot phonons, which in turn leads to the phonon-bottleneck hampering further cooling.

This chapter is mainly focused on understanding the basic properties of these III-V NWs. Starting with InP NWs, TA measurements enabled the visualization of the different energy transitions in two different crystal structures. In addition, after calculating the T_C values in two different materials, i.e., InP and GaAsP NWs, similar hot carrier cooling mechanisms are observed. For InP NWs the initial energy loss rate was about 0.3 eV/ps, and for GaAsP NWs it was 0.5 eV/ps for thick wires and ~1.5 eV/ps for thin wires. Initially the τ_{LO} was found to be about 0.35 ps for InP when T_C = 774 K, τ_{LO} = 0.3 ps for T_C = 944 K in thick GaAsP NWs, and τ_{LO} = 2 ps for T_C = 1380 K in thin GaAsP NWs. NWs with smaller diameters tend to sustain hot carriers for longer durations, and at an elevated temperature. This observation is of practical importance while designing devices where one has to harvest the energy of hot carriers.

Chapter 5 Functionalized nanowires

Semiconductor NWs exhibit a large array of unique opto-electronic, thermal, and photonic properties. Functionalization of semiconductor NWs with plasmonic nanoparticles (NPs) and doping with other elements allows further modification of their properties. Hybrid NW structures composed of semiconductor NWs and plasmonic metal NPs display interesting optical and electronic properties. The tandem existence of local surface plasmon resonance (LSPR) of the metal NPs and the semiconducting properties of the NWs lead to synergetic interactions between the two, leading to better photo-response, such as improved photocatalysis. Similarly, doping semiconductor NWs with other elements, allows bandgap engineering, and facilitates defect state modifications. Both these hybrid systems help design NW based devices with enhanced photonic and optoelectronic properties.

This chapter is devoted to the study of ZnSe NWs decorated with silver NPs and cobalt - doped ZnO nanorods (NRs). Section 5.1 deals with the study of resonant plasmonic effects of Ag NPs on the stationary and transient optical properties of ZnSe NWs. Gold-decorated ZnSe NWs are also studied for the sake of comparison. Transient absorption, photoluminescence and Raman measurements are done on the samples for probing the changes induced by the presence of plasmonic NPs. Section 5.2 deals with the study of the optical properties of Co-doped ZnO NRs. ZnO NRs are doped with Co for their potential use in photoelectrochemical (PEC) water splitting. The further functionalization of these NRs with a metal organic framework (MOF) around them is also discussed briefly. Cathodoluminescence, transient absorption and electrochemical measurements are done to characterize the Co-doped ZnO NRs.

5.1 ZnSe nanowires decorated with plasmonic nanoparticles

5.1.1 Introduction

Metal NPs exhibit unique optical and photonic properties due to plasma oscillations of the conduction band electrons upon interaction with an electromagnetic field.[127] The coherent oscillations of the conduction band electrons localized on a metal NP are called local surface plasmon resonance. When the NPs are irradiated with light having a proper wavelength, the electron cloud oscillates with the electric field against the relatively positive metal nuclei. Figure 5.1 illustrates a localized surface plasmon in the presence of an alternating electric field. The frequencies or modes of these oscillations are determined by the dielectric constants of the

metal and surrounding medium, and the shape and size of the metal NPs.[128] Hence, by controlling the size and shape of the metal NPs, we can change the LSPR wavelength. For small metal NPs with their size much smaller than the wavelength of light, the LSPR are dipole in nature, but as the size of the NPs increase higher multipoles become important, especially the quadrupole term, giving rise to many LSPR modes.[128,129]

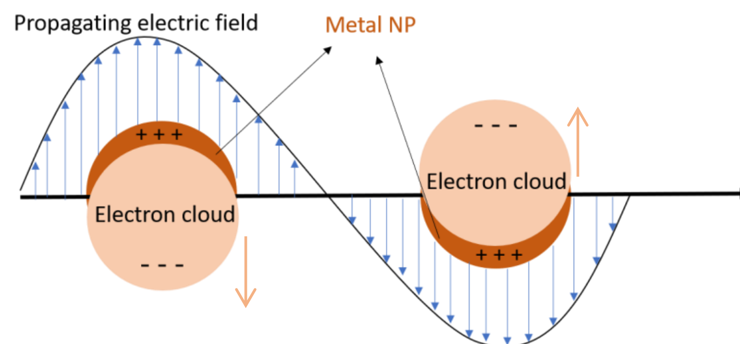

Figure 5. 1. Schematic illustration of local surface plasmon resonance.

The LSPR gives rise to strong resonant fields in its vicinity, making it a very useful candidate in biomedical[130] and molecular sensing,[131] and optoelectronic[132] device design. LSPR of metal NPs also interact strongly with their proximate environment, making them useful in creating tandem devices where the NPs and semiconductors work together, particularly in photocatalysis.[133,134] When the plasmonic NPs are placed in close vicinity of a semiconductor, several electronic interactions can take place between the two leading to the modification of the opto-electronic properties of the semiconductor.[135,136] Upon light incidence, the electrons dephase in the first few femtoseconds due to Landau damping[137] to form a non-thermal distribution of energetic electrons. Within the first 100 fs these electrons form a quasi-equilibrium distribution of hot electrons through electron-electron scattering and, in few picoseconds relax via electron-phonon scattering. Then within tens of picoseconds they couple with the environment, in our case the semiconductor NWs. Over the next hundreds of picoseconds, they complete their heat dissipation process.[138] During LSPR, the hot electrons after dephasing can efficiently transfer energy to the adjacent semiconductor, either by direct injection of the hot electrons, or through dipole mediated energy transfer mechanisms like the Forster resonant energy transfer (FRET) mechanism.[138–141]

In hot electron injection from metal NP to semiconductor, the high energy electrons generated after LSPR dephasing might have the energy necessary to cross the Schottky barrier between the metal and the semiconductor, and move from the conduction band of the metal to the conduction band of the semiconductor.[138,142,143] In plasmon induced resonance energy transfer,

the LSPR induces the creation of electron-hole pairs in the semiconductor through strong dipole-dipole coupling.[139] For the hot electron injection, the requirement is physical contact between the metal NP and the semiconductor, while for the resonant energy transfer, an additional condition of spectral overlap between the LSPR and absorption band of the semiconductor is required. In the systems that we have studied, for Ag-decorated ZnSe NWs, apart from the physical contact, there is also a spectral overlap between the LSPR and the bandgap of ZnSe. Instead, in the case of Au-decorated ZnSe NWs, there is only physical contact between the two. Figure 5.2 shows the static absorption of Ag NPs and the room temperature PL of the ZnSe NWs. Figure 5.2 (a) shows the steady state absorption of Ag NPs deposited on silica NWs[144,145], with similar shape and size distribution as the ones deposited on the ZnSe NWs. Ag decorated silica NWs were chosen to show the absorbance because in these samples only the contribution from Ag NPs is seen at this spectral range.[144,145] Figure 5.2 (b) shows the near band edge emission of the room temperature PL. The ZnSe NWs have a near band edge (NBE) emission at ~2.7 eV, while the LSPR absorption is a broad band from 2.5 eV to 3.5 eV peaking near 2.7- 3 eV. The two peaks in the LSPR are due to the dipole and quadrupole terms in the LSPR modes, with the prominent being the dipole term, which is of importance in this study. While for Ag decorated ZnSe NWs there is spectral overlap between the LSPR spectra and the semiconductor bandgap, the Au NPs have their LSPR at a lower energy compared to the ZnSe bandgap.[146] Hence for the Ag decorated NWs we expect a dipole mediated resonance energy transfer, while for Au decorated NWs we do not anticipate any resonant interactions.

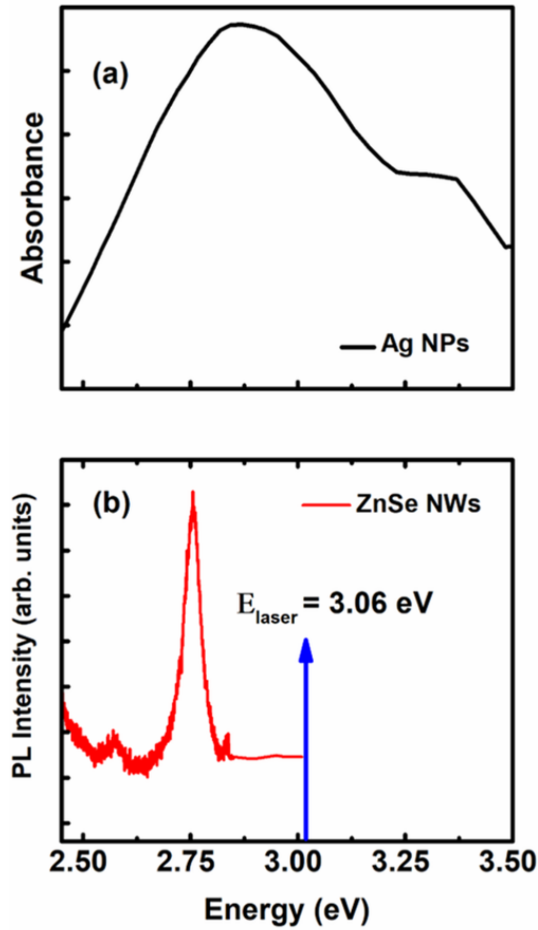

Figure 5. 2. (a) Absorbance of Ag NPs fabricated on the sidewalls of silica NWs, with similar size and shape distribution as the NPs fabricated on ZnSe NWs. (b) Room temperature PL of pristine ZnSe NWs. The blue arrow indicates the pump energy used in the PL measurements.

5.1.2 Material

The ZnSe NWs used in this thesis have been provided by Dr. Silvia Rubini from TASC-IOM-CNR laboratory in Trieste, Italy. They have been grown by molecular beam epitaxy (MBE) on GaAs, quartz and sapphire at 300 °C. A low growth temperature is used to maintain superior optical properties.[147] The samples consist of a very high density of randomly oriented ZnSe NWs which are tapered, with a mean diameter at the tip of 10 nm and base diameter of about 100 nm , and an average length of about 1 μm. Detailed morphological characterization and growth details can be found in Zannier *et al.*[147] A more complete picture of optical properties

including TA measurements and carrier dynamics of ZnSe NWs grown with the same technique have already been studied previously in our laboratory, using the same characterization methods. The details of this study can be found in Tian *et al.*[148]

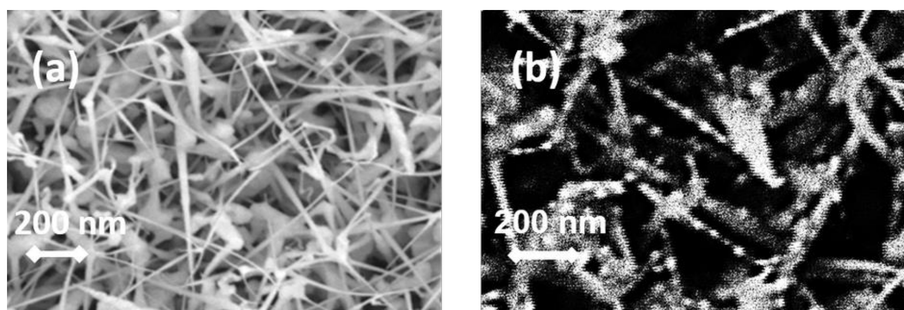

Figure 5. 3. SEM image of typical (a) pristine ZnSe NWs and (b) Ag decorated ZnSe NWs

To deposit metal NPs on the sidewalls of ZnSe NWs, I have evaporated thin films of silver and gold with nominal thickness below 5 nm onto the ZnSe NWs. After the thin film deposition, they were annealed at 280 °C for 10 minutes to form the NPs by thermal dewetting of the thin film. Figure 5.3 shows a scanning electron microscopy (SEM) image of (a) pristine NWs and (b) decorated NWs showing the Ag NPs. The Ag NPs had their size distribution between 20 nm and 50 nm.

5.1.3 Optical characterization

The samples were investigated using stationary absorption, TA spectroscopy in pump-probe configuration, steady state and time resolved PL and Raman measurements using the setups mentioned in Chapter 2. For TA measurements the probe was taken from 3.1 eV to 1.55 eV and measurements were done at room temperature. The PL was carried out using a pump at 3.02 eV with 35 fs long pulses at 80 MHz repetition rate. The measurements were done at room temperature as well as at 10 K in a cryostat.

5.1.4 Results

5.1.4.1 Ag-decorated ZnSe nanowires

(a). Steady state absorption

Figure 5.4 shows the steady state absorbance of pristine (red) and Ag-decorated (black) ZnSe NWs. The overall absorbance of the Ag-decorated ZnSe NW sample is higher than that of the pristine sample. It can also be seen that the line shape of absorbance for Ag-decorated NWs differs from that of pristine sample between 2.2 eV and 2.6 eV. The higher absorbance is due to increased light absorption by the plasmonic metal NPs, as well as increased light scattering by the metal NPs.

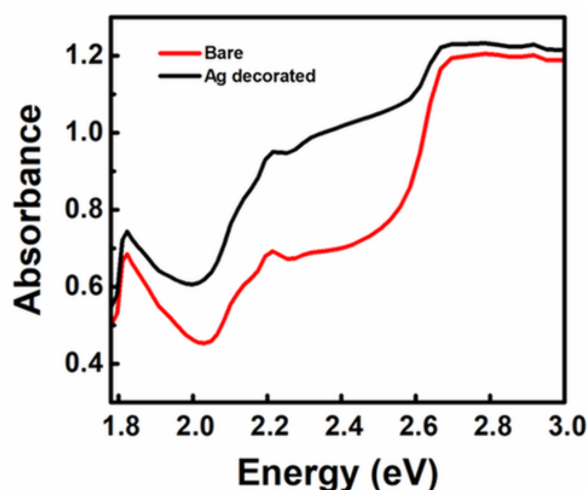

Figure 5. 4. Absorbance of bare (red curve), and Ag-decorated ZnSe NWs (black curve).

(b). Fast Transient Absorption spectroscopy

Figure 5.5 presents the results of TA measurements on bare and Ag-decorated ZnSe NWs. The samples were excited using an ultrafast pump at 3.02 eV with a fluence of 260 μJ/cm^2. Figure 5.5 (a) and Figure 5.5 (b) show the 2D false colormaps of the TA spectroscopy measurements, with probe energy along y axis and time delay along x axis for bare and Ag-decorated ZnSe NWs, respectively. Both samples show absorption bleaching at the NBE energy of ~ 2.7 eV, and a broad defect band at lower energies, like the observations made in Tian *et al.*[148]. The two maps are spectrally similar with a few notable differences. The intensity of the TA signal of the NBE region in the Ag-decorated sample is reduced by about 20% with respect to that of the bare ZnSe NWs. Also, the defect related bands have lost relative intensity of their TA signal

in Ag-decorated ZnSe NWs compared to bare ZnSe NWs. An important observation is the lack of the presence of plasmonic signals in the TA of Ag-decorated ZnSe NWs.

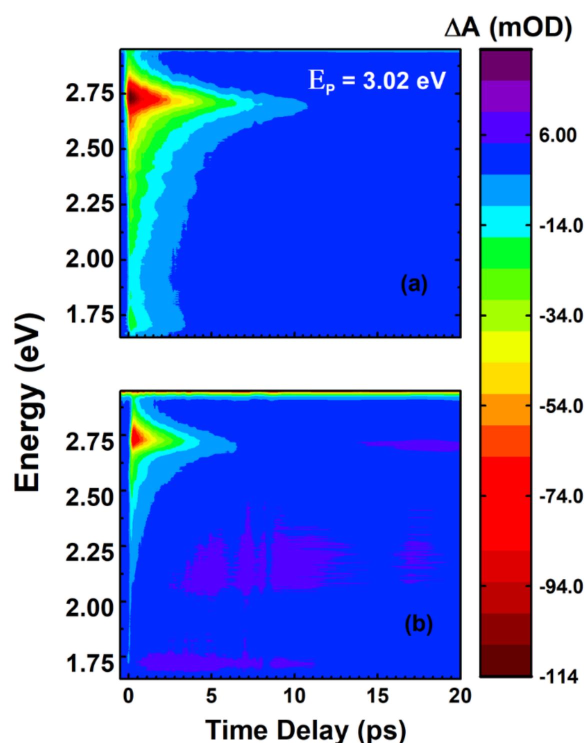

Figure 5. 5. Two-dimensional false colormap of the absorbance difference, ΔA, as a function of the delay time between pump and probe (x axis) and probe energy (y axis) of (a) bare, and (b) Ag decorated ZnSe NWs. The samples were excited with a pump at 3.02 eV with a fluence of 260 $\mu J/cm^2$.

Figure 5.6 shows the normalized TA intensity at time delay of 1 ps between the pump and the probe for bare and Ag decorated ZnSe NWs. The intensity is normalized between {0,1}. The red curve represents the bare ZnSe NWs, while the black curve represents the Ag-decorated ZnSe NWs. The reduction of the relative intensity of the defect band can be observed clearly from Figure 5.6.

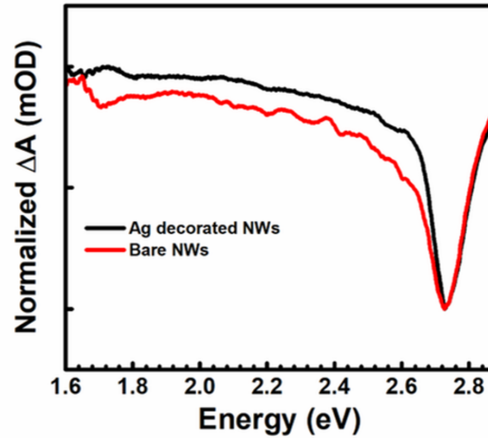

Figure 5. 6. Normalized between {0,1} TA signal of bare (red) and Ag-decorated (black) ZnSe NWs, at a time delay of 1 ps between pump and probe.

Further differences in the TA spectra were revealed upon the analysis of the temporal behavior of the spectra. Figure 5.7 reports the dynamics of ΔA in bare and Ag-decorated ZnSe NWs. Figure 5.7 (a) and Figure 5.7 (b) show ΔA at bandgap energy for bare and Ag-decorated ZnSe NWs, respectively, along with the exponential fit to determine the rise time of the bleaching signal. The rise time increases from τ_r=165±52 fs in the bare ZnSe NW sample to τ_r=250±95 fs in the Ag-decorated sample. Figure 5.7 (c) shows the normalized ΔA as a function of time delay and a reduction is observed in the decay lifetime of the TA signal at the NBE energy in the Ag-ZnSe NWs with respect to the bare ZnSe NWs. In the former case we find τ_d=1.85±0.05 ps as compared with τ_d = 3.57±0.08 ps in the latter one. Finally, Figure 5.7 (d) shows the values obtained for the decay time as a function of the probe energy for the bare ZnSe NWs (red circles) and Ag-decorated ZnSe NWs (black squares). The decay time constant is higher around the bandgap and falls for higher as well as lower probe energies. This behavior was reported in Tian *et al* as well.[148] Ag-decorated ZnSe NWs show a similar trend, but with the decay times being lower than their corresponding values in pristine samples throughout the probed region. TA measurements were also performed using lower fluences. Figure 5.8 shows the summary of temporal analysis of rise time for both samples obtained through TA measurements with a pump of 40 μJ/cm^2 as well as the fluence dependence of rise and decay times.

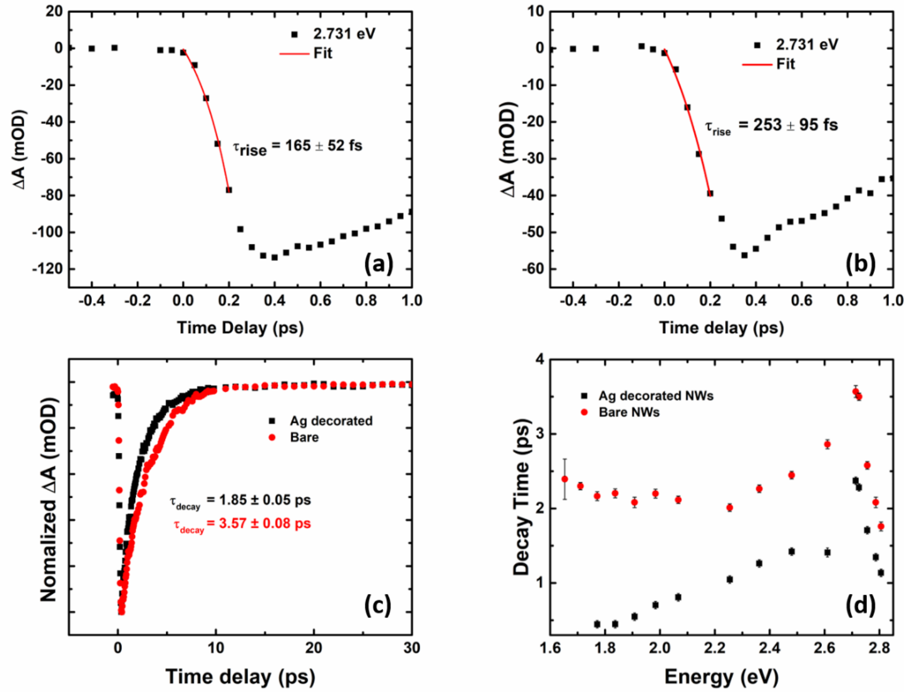

Figure 5. 7. Temporal behavior of ΔA signal at bandgap energy for (a) bare, and (b) Ag-decorated ZnSe NWs, along with the best fit (red curve) for rise time. (c) Normalized between {0,1} ΔA at bandgap bleaching for bare (red) and Ag-decorated (black) ZnSe NWs. (d) The decay time as a function of probe energy for bare (red) and Ag-decorated (black) ZnSe NWs.

The rise time increases with decreasing excitation fluence and the decay time decreases with decreasing fluence. Similar behavior was reported in Tian *et al.*[148] For the Ag-decorated ZnSe NWs, the rise time has been observed to be higher than their corresponding values in bare ZnSe NWs at all fluences. The decay times in Ag-decorated NWs are observed to be lower than corresponding values for bare ZnSe NWs at all fluences.

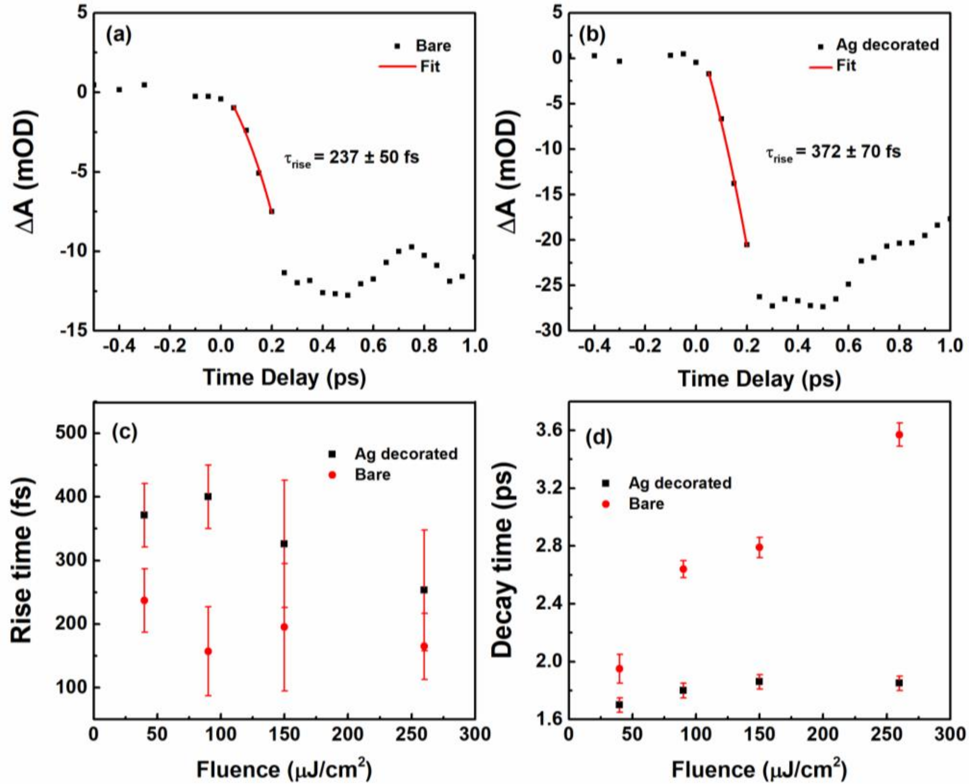

Figure 5. 8. The temporal behavior of ΔA at bandgap energy showing rise time at the bandgap bleaching for (a) bare and (b) ZnSe NWs at an excitation fluence of 40 μJ/cm². The red curve is the trace of the exponential fit. The dependence of rise time (c) and decay time (d) of Ag decorated (black squares) and bare (red circles) ZnSe NWs.

(c) Steady state and time resolved photoluminescence measurements

The low temperature photoluminescence (LTPL) of ZnSe at 10 K typically has three prominent spectral features: the near band edge (NBE) emission around 2.8 eV, and deep and shallow donor acceptor pair bands.[147,149] Liang and Yoffe[149] have extensively characterized LTPL spectra from hexagonal ZnSe crystals at 4 K and 77 K. They have described three types of bound excitons in ZnSe; excitons bound to neutral donors, excitons bound to ionized acceptors, and excitons bound to neutral acceptors. All these bound excitons have low ionization energies, being 0.0029 eV, 0.0057 eV and 0.0098 eV, respectively. [149] Because of the polar nature of ZnSe crystal, the LO-phonons produce a macroscopic electric field and the electrons interact with this field. The coupling is called the Frohlich interaction.[150] This leads to the emission of LO phonon replicas in the LTPL. Figure 5.9 presents the results of LTPL at 10 K measured on

Ag-decorated and bare ZnSe NWs grown on quartz substrate, excited using a pulsed laser at 3.06 eV (405 nm) and fluence of 0.19 μJ/cm^2.

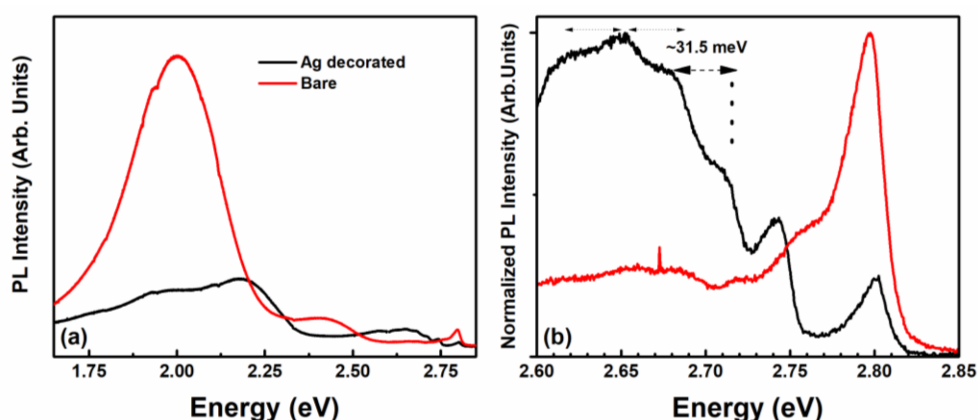

Figure 5. 9. (a) LTPL at 10 K for Ag decorated (black curve) and bare (red curve) ZnSe NWs. (b) Detail of the high-energy part of the PL spectrum in (a) shown as normalized PL intensity. Samples grown on quartz, and excited using a pulsed laser at 3.06 eV with a fluence of 0.19 μJ/cm^2.

In Figure 5.9 (a), the red curve shows the PL emission for bare ZnSe NWs. The two peaks centered around ~2 eV and centered around ~ 2.4 eV are assigned to luminescence from deep centers. The very weak emission (seen in Figure 5.9 (b) in red)) between 2.7 eV and 2.6 eV is assigned to emission from shallow centers. The peak at ~ 2.8 eV is assigned to luminescence from free exciton emission. In the presence of Ag NPs (black curve in the PL spectra) The broad emission around (shallow centers) 2.7 eV gains prominence and splits into several narrower peaks. The excitonic peak is at 2.8 eV, while in the energy range between 2.65 eV and 2.75 eV 4 to 5 equidistant peaks are observed. For samples grown on quartz for the shallow center recombination, we have the data in Table 5.1. From Table 5.1, it can be seen that the shallow centers related emission band is split into 5 narrow peaks, all separated from adjacent peaks by the energy of the LO-phonon (~31.5 meV).

Table 5.1. The energies of the shallow emission centers in Ag-decorated ZnSe NWs. The observed peaks at 10 K and the values found in literature for comparison, along with the assignment of the peaks.

Energy position observed at 10 K	**Energy at 77 K in literature** [149]	**Assignment**
2.7436 eV	2.7461 eV	Zero-phonon
2.7122eV	2.7143 eV	One-phonon
2.6804 eV	2.6830 eV	Two-phonon
2.6489 eV	2.6501 eV	Three-phonon
2.6181 eV	2.620 eV	Four-phonon

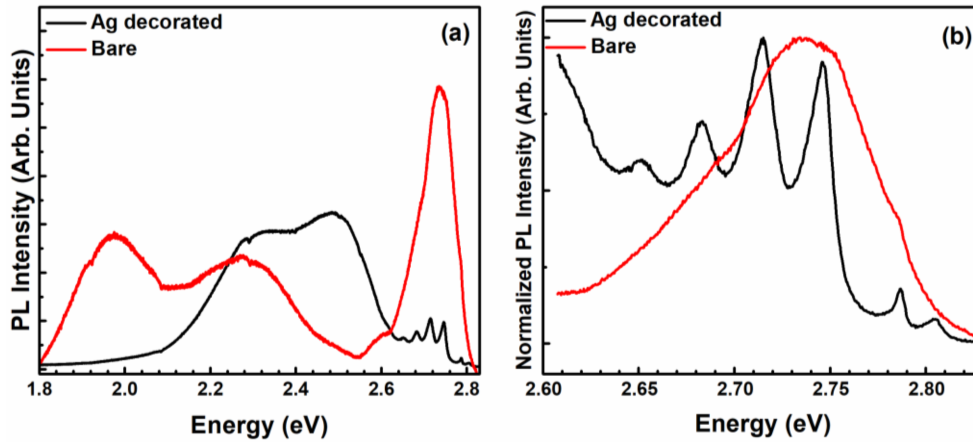

Figure 5. 10. (a) LTPL at 10 K for Ag decorated (black curve) and bare (red curve) ZnSe NWs. (b) Detail of the high-energy part of the LTPL spectra shown in (a). Samples are grown on Sapphire substrate, and excited using a pulsed laser at 3.06 eV with a fluence of 0.19 μJ cm^2.

PL measurements were also done on samples grown on sapphire and GaAs substrates. Figure 5.10 shows the LTPL spectra at 10 K for the Ag decorated and bare ZnSe NWs grown on

sapphire substrate. Figure 5.10 (a) shows the PL spectra in the entire energy range, while Figure 5.10 (b) focuses on the high energy part of the spectra, with black and red curves representing Ag-decorated and bare ZnSe NWs, respectively. The nature of the defect band changes with the substrate used, which is attributed to the contamination from the substrate. Nevertheless, the donor acceptor pair (DAP) band splits into equally separated (~31.5 meV) peaks in the presence of Ag NPs on the NW sidewalls, while this is not the case in the bare ZnSe NWs under the same excitation conditions. Temperature dependent and power dependent measurements were also performed to determine the onset of the equidistant peaks in the presence of Ag NPs on the ZnSe NW sidewalls. Figure 5.11.(a) and Figure 5.11.(b) show temperature dependent PL spectra of Ag-decorated ZnSe NWs grown on quartz and GaAs substrates, respectively. The samples were excited with a pulsed laser of 3.06 eV of fluence of 0.13 μJcm^{-2}.

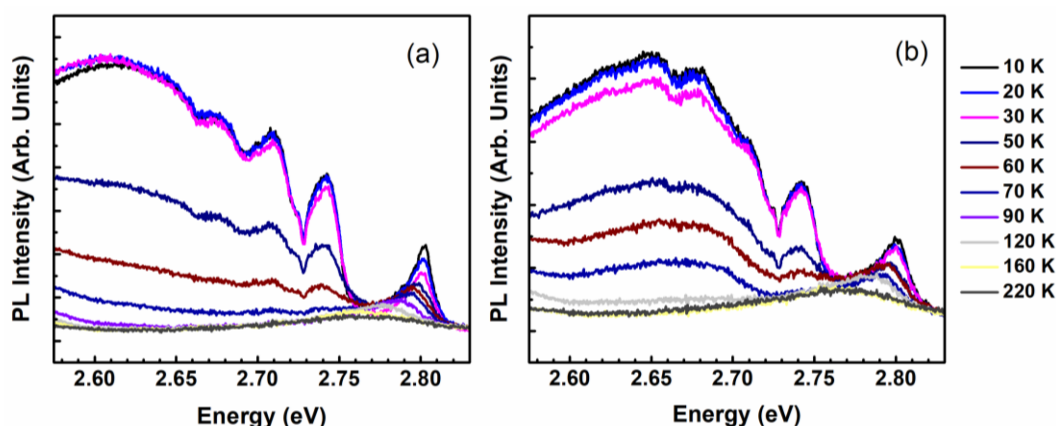

Figure 5. 11. Temperature dependent PL spectra of Ag-decorated ZnSe NWs grown on (a) quartz and (b) GaAs substrates. Samples were excited by a pulsed laser at 3.06 eV and fluence of 0.13 μJ cm^{-2}.

The Ag-decorated NWs grown on all the substrates show the splitting of the DAP band between 2.6 eV and 2.75 eV. Temperature dependent PL measurements with a pulsed laser excitation at 3.06 eV and laser fluence of 0.13 μJ/cm^2 show that the splitting of the band into equidistant peaks disappears around 70 K with rising temperature. Liang and Yoffe[149] have assigned the binding energy of excitons bound to ionized acceptors as 66.15 K (0.0057 eV). This is verified by the disappearance of the band centered around 2.7 eV around 70 K. Figure 5.12 (a) and Figure 5.12 (b) show the power dependent LTPL spectra at 10 K of Ag decorated and bare ZnSe NWs, respectively. The samples were grown on quartz and excited with a 3.06 eV pulsed laser. The power dependent measurements show that the splitting of the DAP band in the presence of Ag NPs become more prominent with increasing excitation intensity. Time

resolved PL (TRPL) measurements were also performed on Ag-decorated and bare ZnSe NWs to study the resonant effects of metal LSPR in the vicinity of the semiconductor NW.

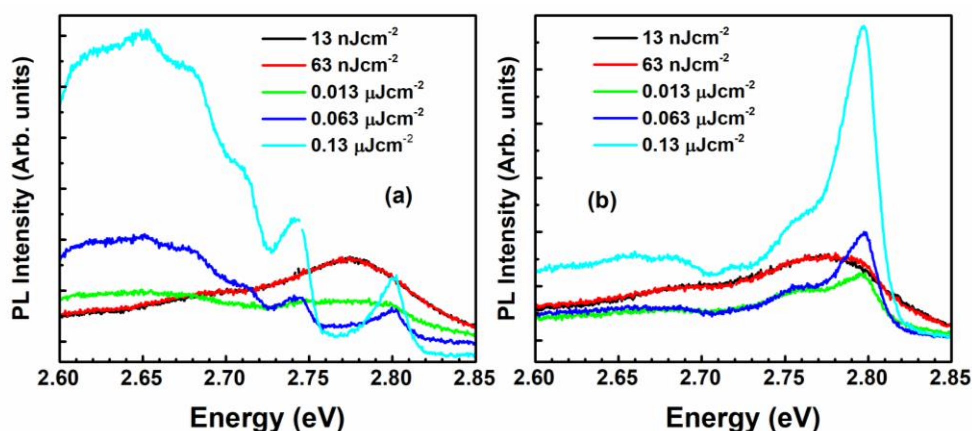

Figure 5. 12. Power dependent PL spectra at 10K for (a) Ag-decorated and (b) bare ZnSe NWs grown on quartz substrate. The samples were excited using a pulsed laser at 3.06 eV.

The TRPL measurements were done for the NBE peak at 2.8 eV. The measurements were done at 10 K and samples were excited by a 3.06 eV pulsed laser with a fluence of 0.19 μJcm^{-2}. Figure 5.13 presents the results of TRPL measurements. Figure 5.13 (a) shows the TRPL measurements on bare ZnSe NWs. The red curve shows the best fit for the data. Figure 5.13 (b) shows the TRPL data along with the best fitting curve(red) for the Ag decorated ZnSe NWs. The TRPL data were fitted with a single exponential decay function of the form: $y(t) = y_0 + A_1 \exp(-t/\tau)$. The decay times were found to be 0.46 ± 0.01 ns and 0.44 ± 0.02 ns for bare and Ag decorated ZnSe NWs, respectively. The values agree with previously measured decay time for radiative recombination in ZnSe.[148] The presence of Ag NPs does not affect the radiative decay time of ZnSe NWs within the limits of experimental setup.

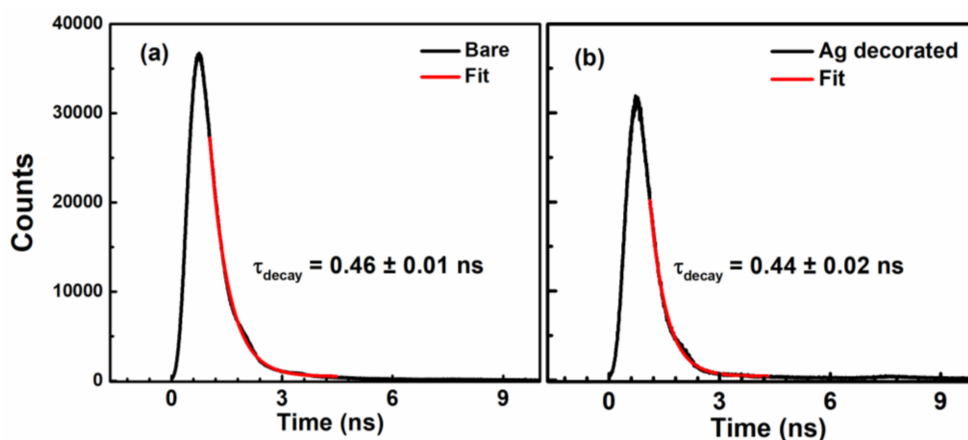

Figure 5. 13. TRPL measurements at 10 K of the NBE for (a) bare and (b) Ag-decorated ZnSe NWs grown on quartz substrate. The samples were excited using a laser at 3.06 eV and with laser fluence of 0.13 μJcm^{-2}.

(d) Raman measurements

Raman measurements were done on both bare and Ag-decorated ZnSe NWs to probe the direct implication of the presence of metal NPs on the phonon interaction in the semiconductor NWs, as well as on the crystalline quality. Figure 5.14 shows the room temperature Raman spectra of Ag-decorated and bare ZnSe NWs. The emission line from Ar^+ laser at 457 nm is used to excite the NW samples.

Figure 5.14 shows a series of 4 peaks at 252.8 cm^{-1}, 503 cm^{-1}, 753 cm^{-1} and 1002.8 cm^{-1}, corresponding to the different longitudinal optical (LO)-phonon replicas in ZnSe.[151] The first LO-phonon replica at 252.8 cm^{-1} being the most intense. A shoulder appearing around 206 cm^{-1} is assigned to the presence of transverse optical (TO) phonons[152] and the peak at around 140 cm^{-1} is assigned to transverse acoustic (TA) phonons. The Raman spectra of Ag-decorated ZnSe NWs were spectrally like that of the pristine NWs. No peak shift is observed in the presence of Ag NPs. No peaks related to defects are observed in both spectra. Only the intensity of the peaks is diminished in the presence of Ag NPs. The relatively high symmetry and sharpness of the peaks suggest high crystalline quality, both for bare and Ag decorated ZnSe NWs.

The lack of the shift in the Raman peak suggests that the presence of Ag NPs does not impact the crystal structure.

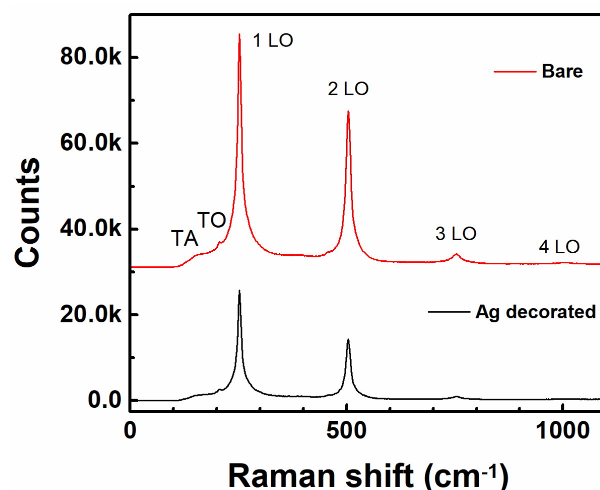

Figure 5. 14. Raman spectrum of as-grown bare (red) and Ag decorated (black) ZnSe NWs at room temperature. Excited using a laser at 457 nm.

5.1.4.2 Au-decorated ZnSe NWs

Optical measurements were also performed on Au-decorated ZnSe NWs. These measurements were done for the comparison between two systems: (1) a system with LSPR resonant with the semiconductor bandgap (Ag-decorated ZnSe NWs) and (2) a system with no resonance between the metal NP LSPR and semiconductor bandgap (Au-decorated ZnSe NWs). For Au NPs of similar shape and size distribution, the LSPR lies at a lower energy compared to ZnSe bandgap.[146,153]

(a) Transient Absorption spectroscopy

Figure.5.15 presents the results of room temperature TA measurements on Au-decorated ZnSe NWs. Figure.5.15 (a) shows the 2D transient map of the ΔA intensity as a function of time delay and probe energy for Au-decorated ZnSe NWs. The sample was excited with a pump of 3.02 eV and fluence of 260 μJcm^{-2}. For Au-decorated ZnSe NWs, the 2D colormap shows the NBE bleaching at 2.7 eV, and the LSPR signal around 2.3 eV as well. The positive wings of the Au LSPR is also clearly visible from the 2D map around 2.5 eV. Figure.5.15 (b) shows a clearer picture of the TA at 0.6 ps delay between pump and probe. It is also important to note that the ΔA values are much lower for Au-decorated ZnSe NWs compared to Ag-decorated or bare ZnSe NWS.

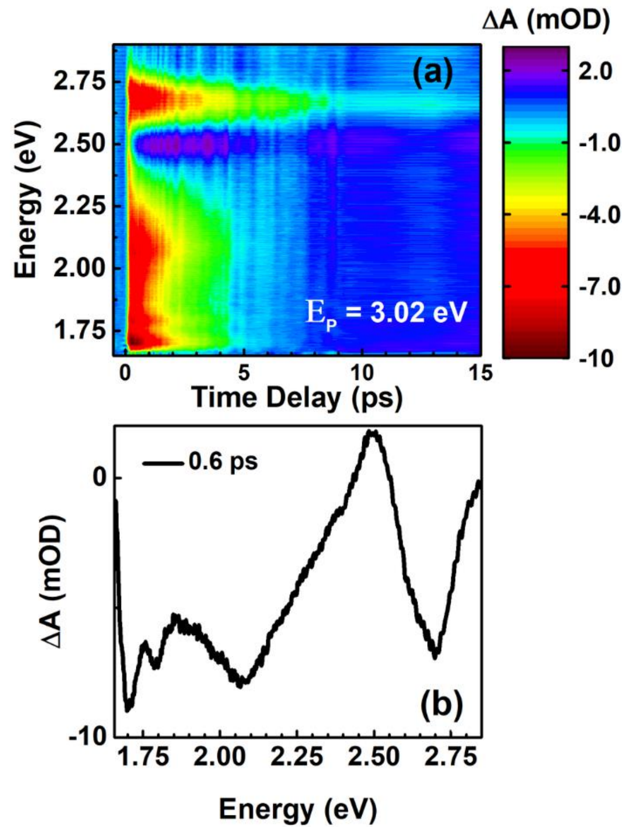

Figure 5. 15. (a) 2D false color map of the TA, ΔA as a function of the delay time between pump and probe (x axis) and probe energy (y axis) of Au decorated ZnSe NWs. (b) TA of Au decorated ZnSe NWs at a time delay of 0.6 ps.

The bandgap bleaching of Au-decorated ZnSe NWs was fitted with an exponential decay function by considering the response function of the spectrometer (50 fs). Figure 5.16 shows the comparison of the TA dynamics for Ag-decorated, Au decorated and bare ZnSe NWs, excited by 3.02 eV laser with a fluence of 260 μJ/cm^2.The rise time of the bandgap bleaching for Au-decorated and bare ZnSe NWs are 150 ± 90 fs and 162 ± 52 fs, respectively. Instead, the rise time for Ag decorated ZnSe NWs is longer at 253 ± 95 fs. Similarly, the decay time constant for the bleaching signal at the bandgap for Au decorated ZnSe NWs is 3.69 ±0.21 ps, very close to 3.57 ± 0.08 ps found in bare ZnSe NWs, while Ag-decorated ZnSe NWs have a faster decay for the bandgap bleaching with the decay constant of 1.85 ± 0.05 ps.

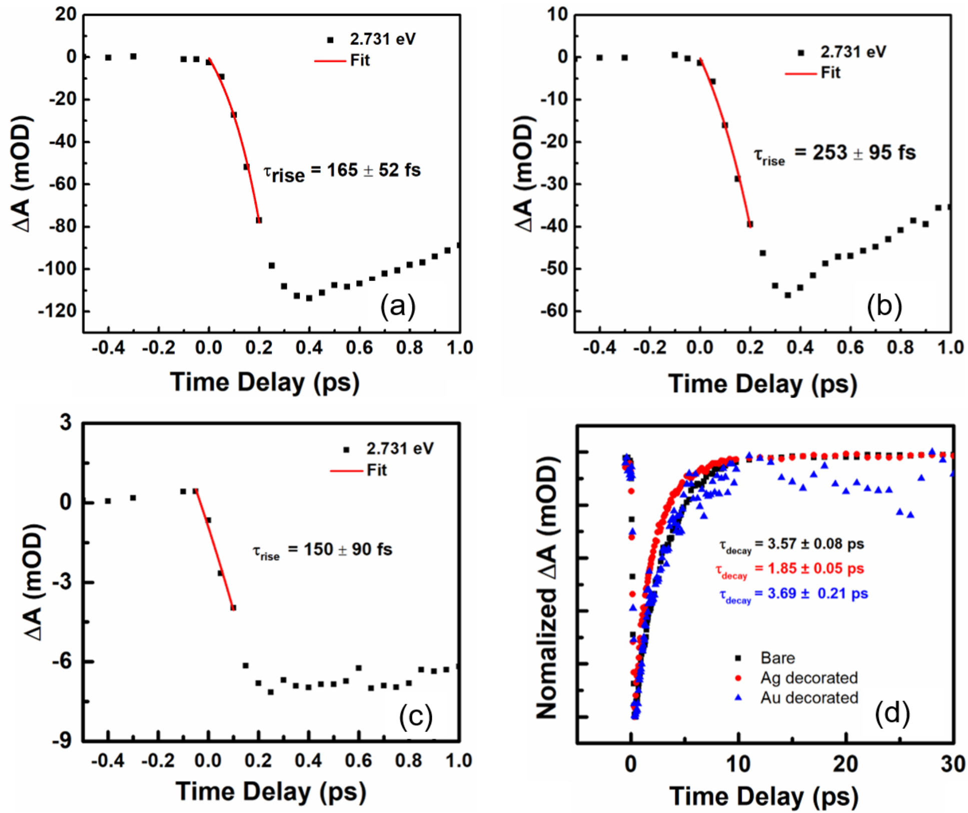

Figure 5. 16. Rise time of bandgap bleaching in (a) bare, (b) Ag-decorated, and (c) Au-decorated ZnSe NWs along with the red curve showing the fitting of the data. (d) Normalized ΔA signal at bandgap bleaching as a function of time delay to show the difference in the decay times. Black, red, and blue represents bare, Ag-decorated, and Au-decorated ZnSe NWs.

(b) Photoluminescence measurements

Figure 5.17 shows the LTPL spectra of Au-decorated ZnSe NWs along with Ag decorated and bare ZnSe NWs for comparison. The green curve in Figure 5.17 (a) and Figure 5.17 (b) show the LTPL of Au decorated ZnSe NWs, excited with a pulsed laser of 3.06 eV energy and fluence of 0.19 μJcm^{-2}. The black and red curves show the PL spectra of Ag decorated and bare ZnSe NWs, respectively, measured in similar conditions. The Au NPs deposited on the ZnSe sidewalls do not cause any significant change to the PL line shape. The only effect is the decrease of the NBE PL intensity due to increased light scattering. The DAP emissions between 2.65 eV and 2.75 eV are also reduced in intensity.

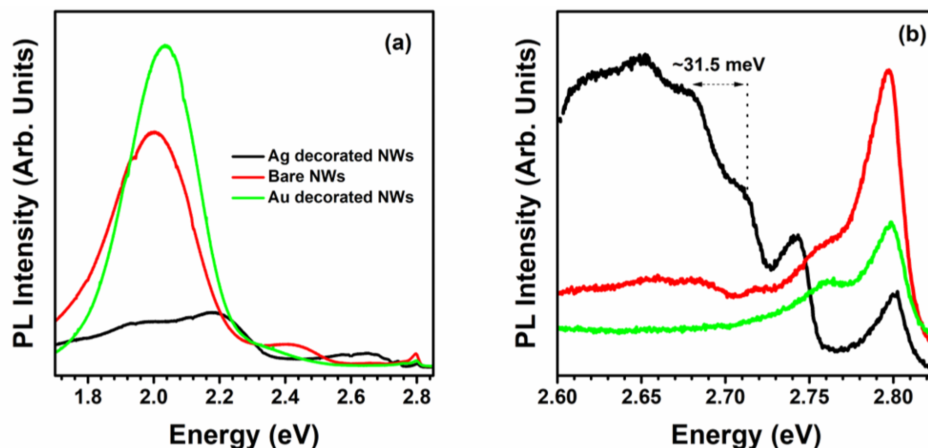

Figure 5. 17. (a) LTPL spectra at 10 K of bare (red) and Ag-decorated (black) and Au-decorated (green) ZnSe NWs grown on quartz. (b) Detail of the high-energy part of the PL spectrum shown in (a). The samples are grown on quartz, excited with a pulsed laser at 3.06 eV.

5.1.5 Discussion

The optical properties of ZnSe NWs can be significantly modified by depositing plasmonic metal NPs with resonant LSPR on its sidewalls. By studying two different systems involving plasmonic metal NPs deposited on the sidewalls of ZnSe NWs, we have observed the difference between the systems where the LSPR is resonant with semiconductor bandgap and the LSPR is not in resonance with bandgap of the semiconductor. The spatial proximity is the common factor in Ag-decorated and Au-decorated ZnSe NWs; however, the spectral overlap is present only in the former. The two mechanisms of interaction that can take place when plasmonic NPs are in the vicinity of semiconductors are hot carrier injection and dipole mediate resonant energy transfer. Both interactions are possible for Ag-decorated ZnSe NWs while only the hot electron transfer is possible for Au-decorated ZnSe.

As mentioned in the introduction, the LSPR decays in a very short time scale leading to the creation of hot electrons, which then interact with the environment. If these hot electrons have sufficient energy to cross the Schottky barrier between the metal and semiconductor (ZnSe), the hot electron injection from metal to semiconductor can take place. The Schottky barrier is defined as the difference between the metal work function and semiconductor electron affinity, and it is the indication of the minimum energy that an energetic electron possesses to move from the metal to the semiconductor. In this case the Schottky barrier is 1.06 eV for Ag and

1.45 eV for Au. [154–156] The Fermi level in both these metals lie above their d-bands (2.58 eV for Au and 3.93 eV for Ag).[157,158] The hot electrons that having sufficient energy to pass to ZnSe will be close to the Fermi level. Assuming a parabolic density of states, this is comparable in both systems. If the changes in optical properties were only because of hot electron transfer this should be the same for both the systems. However, both the TA and PL spectra are modified in Ag-decorated ZnSe NWs, while the Au-NPs did not report significant changes. Hence, the mechanism of interaction between Ag NPs and ZnSe NWs is assigned to the dipole mediated resonant energy transfer.

The main changes in the TA spectra in the presence of Ag NPs are the increase in the rise time and the decrease in the decay time of the bandgap bleaching. The increase in rise time could indicate a resonant energy transfer mechanism with Ag NPs acting as donors and ZnSe acting as acceptor,[141] leading to electron-hole creation in ZnSe after the time of photoexcitation. On the other hand, the decay time constant is reduced in the presence of Ag NPs throughout the spectral region. From Figure 5.2, the steady state absorption of Ag NPs is broad due to the presence of dipole and quadrupole plasmonic excitations. The broad width may allow for resonant interaction throughout the spectral region, such as with the defect band, leading to the decrease in the bleaching signal lifetimes. At lower energies, there could also be contribution from free carriers in the absorbance. A possible explanation for the decrease in the lifetime of bleaching signal could be the improvement in electron-phonon coupling. This increased coupling could lead to better carrier-phonon scattering rates leading to faster cooling of the excited carriers. The appearance of the phonon-replicas in the LTPL emission for Ag-decorated ZnSe NWs at low excitation intensities also suggest the stronger coupling of carriers and phonons. However, it is important to note that a direct correlation cannot be made between the TA measurements made at room temperature and PL measurements at 10 K.

The presence of Au-plasmonic signal in the Au decorated ZnSe NWs, while no plasmonic signal was seen in the Ag decorated NWs, could indicate that the energy transfer in the latter system is very efficient, i.e., the energy absorbed by the plasmon resonance is efficiently transferred to ZnSe NWs before the heating of Ag NPs.

Even though the exact mechanism of the resonant interaction between the plasmonic NPs and semiconductor NWs cannot be pinpointed, one can rule out a simple passivation mechanism due to the presence of the Ag NPs on the NW sidewalls, because not even the slightest line shape change of the same type is observed with Au-decorated NWs. Since the surface coverage is very similar in both the cases, one can also exclude that the differences are due to different degrees of surface passivation. The impurity-related recombination occurs only at low temperatures because of the involvement of shallow donors and acceptors, and related effects cannot be observed at room temperature, at which we perform our FTAS measurements. This prevents us from making a direct comparison between the low-temperature PL and the room

temperature FTAS. Nevertheless, both measurements point towards a more efficient carrier–phonon interaction.

5.2 Cobalt doped ZnO nanorods

5.2.1 Introduction

In the second part of this chapter, the effects of Co-doping in ZnO NWs are studied. ZnO is a widely studied wide bandgap (3.3 eV) semiconductor of the II-VI group.[159–161] ZnO has high exciton binding energy of about 60 meV at room temperature making it an important material for photonic devices.[160] ZnO also has tremendous applications as a transparent conductive oxide, in sensors, in piezoelectric devices, etc.[162] The most important aspect of ZnO is that it is earth abundant and it can be grown with inexpensive, industrial techniques.[163,164] ZnO also has high electron mobility.[164] These factors make it an interesting candidate for photoelectrochemical (PEC) applications such as photocatalysis or PEC water splitting. However, the wide bandgap of ZnO proves to be a limitation for these applications due to poor visible light absorption. This is where the Co-doping comes into play because the Co-doping can narrow the bandgap and extend the light absorption to the visible part of the spectrum.[165] Co-doping has also gained large popularity because of the possible room temperature ferromagnetism in Co-doped ZnO.[165–167] In this thesis only the changes in the optical properties are discussed with the application in PEC devices, especially water splitting as the main application driver.

ZnO is a wurtzite crystal, with the valence band governed by the p orbitals of oxygen, and the conduction band governed by the hybridized sp orbitals of Zn.[164,168] Upon Co-doping, the d electrons of the Co^{2+} interacts with the band electrons of ZnO forming an sp-d exchange interaction, which in turn narrows the bandgap.[169,170] The improvement in the light absorption is further enhanced by using the material in the form of NRs, where the high surface to volume ratio helps to enhance the functionality. By using 3D arrays of NRs, it is possible to have more light absorbing surface for the same amount of material when comparing with thin films or bulk counterparts.

The characterizations are done on ZnO NRs grown by a scalable and economic chemical growth process.[171] The doping levels in the ZnO NRs are controlled by varying the ratio of Co and Zn precursors in the chemical bath. Initial optical and PEC characterization are done to identify the optimal growth condition for the best PEC performance. Through these characterization techniques, the importance of defect engineering in semiconductors are also studied. The best concentration in growth solution was determined and these NRs are further

functionalized to improve their PEC performance. For this purpose, the Co-doped ZnO NRs are coated with a transparent metal organic framework (MOF) of the zeolite family, in particular the zeolitic imidazolate frameworks-8 (ZIF-8).[45] MOFs are hybrid crystals containing both organic and inorganic components. They are highly porous in nature. Hence, the presence of the MOF around the Co-doped ZnO NR core provides more surface area as well as improved charge separation and better chemical stability.[172,173] The hybrid combination of Co-doping combined with the presence of MOF around the NR gives the optimal performance. The optical and PEC characterization of MOF coated Co-doped ZnO NRs are also discussed in this chapter.

The PEC characterization was done by Alejandro Galan Gonzalez at Instituto de Carboquímica (ICB-CSIC), Zaragoza, Spain as well as the SEM images at Durham University, UK. I have performed the FTAS and CL measurements. The latter was performed by at EPFL, Switzerland.

5.2.2 Material

The ZnO NRs used in the study were grown on textured seed layers by chemical bath deposition on a 25 nm thick ZnO seed layer deposited by atomic layer deposition on a range of different substrates such as quartz, ITO-coated glass and silicon.[171] The NRs were grown by Alejandro Galan Gonzalez, at Durham University. The seed layers were immersed in a solution containing equimolar concentrations (25 mM) of zinc nitrate hexahydrate and hexamethylenetetramine in water, which was subsequently heated to 90ºC for 6 hours. Afterwards, the as-grown NRs were thoroughly washed with deionized water and blow dried under a N_2 stream. For the cobalt doping, the desired amount of cobalt nitrate hexahydrate was added to the growth solution, with the nominal doping levels being defined by the concentration ratio of the Co^{2+}/Zn^{2+} in the solution, as 1%, 5% and 20%. Figure 5.18 shows the schematic of the growth process for the Co-doped ZnO NRs.

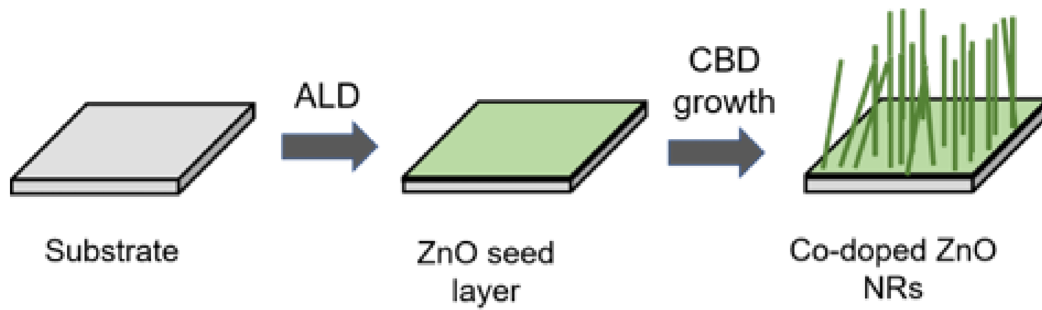

Figure 5. 18. Schematic diagram of the growth process of Co-doped ZnO NRs.

Figure 5.19 (a), (b), (c) and (d) show the SEM images of undoped, 1%, 5% and 20% ZnO NRs, respectively.

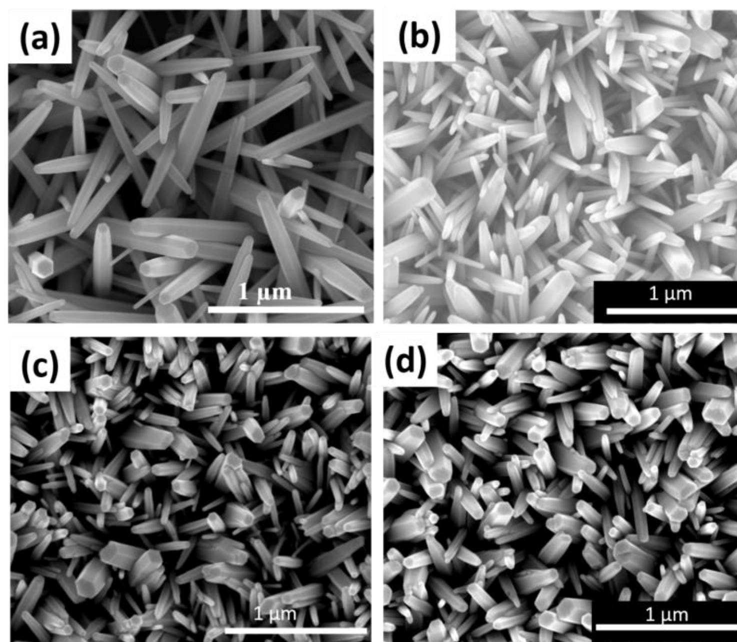

Figure 5. 19. SEM images of (a) undoped, (b) 1% C-doped, (c) 5% Co-doped, and (d) 20% Co-doped ZnO NRs.

5.2.3 Optical characterization

The samples were investigated using transient absorption in pump-probe configuration, and CL measurements using setups mentioned in Chapter 2. For transient absorption measurements the probe wavelength was in the visible region of the spectra and measurements were done at room temperature. The CL was carried out using an electron beam of energy 5 keV, at room temperature as well as 10K in a liquid He cooled cryostat. The time resolved PL (TRPL) was carried out using a time correlated single photon counting (TCSPC) method after sample excitation at 4.51 eV.

5.2.4 Results

(a) Cathodoluminescence measurements

Figure 5.20 presents the results of room temperature CL measurements on Co-doped ZnO NRs. The measurements were done on a mechanically transferred ZnO NR onto a conductive silica substrate. The CL spectra consist of a narrow emission band at ~ 3.3 eV for all the samples, which has been assigned to NBE emission. There is also a broad emission spanning the visible region of the spectra, which has been assigned to defect related emissions.[174,175] Even though all the samples have similar spectral features, it must be noted that with increasing doping concentration, the ratio of intensity of NBE to intensity of defects decreases.

Figure 5.20 (a) shows the SEM image of a 1% Co doped ZnO NR, superimposed with the color specific emission. The red color corresponds to the NBE emission of ZnO, around 3.3 eV, while the green color corresponds to the broad defect band spanning 1.5 to 2.7 eV. Four points are numbered along the length of the NR, and CL spectra extracted from these points are shown in Figure 5.20 (b). The CL spectra shows a narrow NBE emission and broad defect band. Figure 5.20 (c) shows color specific emission similar to the one shown in Figure 5.20 (a) for 5% Co doped ZnO NRs. Figure 5.20 (d) shows the CL spectra extracted from 4 points marked on Figure 5.20 (c). Figure 5.20 (e) shows the normalized CL spectra from undoped, 1%, 5% and 20 % Co-doped ZnO NRs. The relative contribution of the defect band with respect to the NBE peak increases with increasing Co-doping concentration.

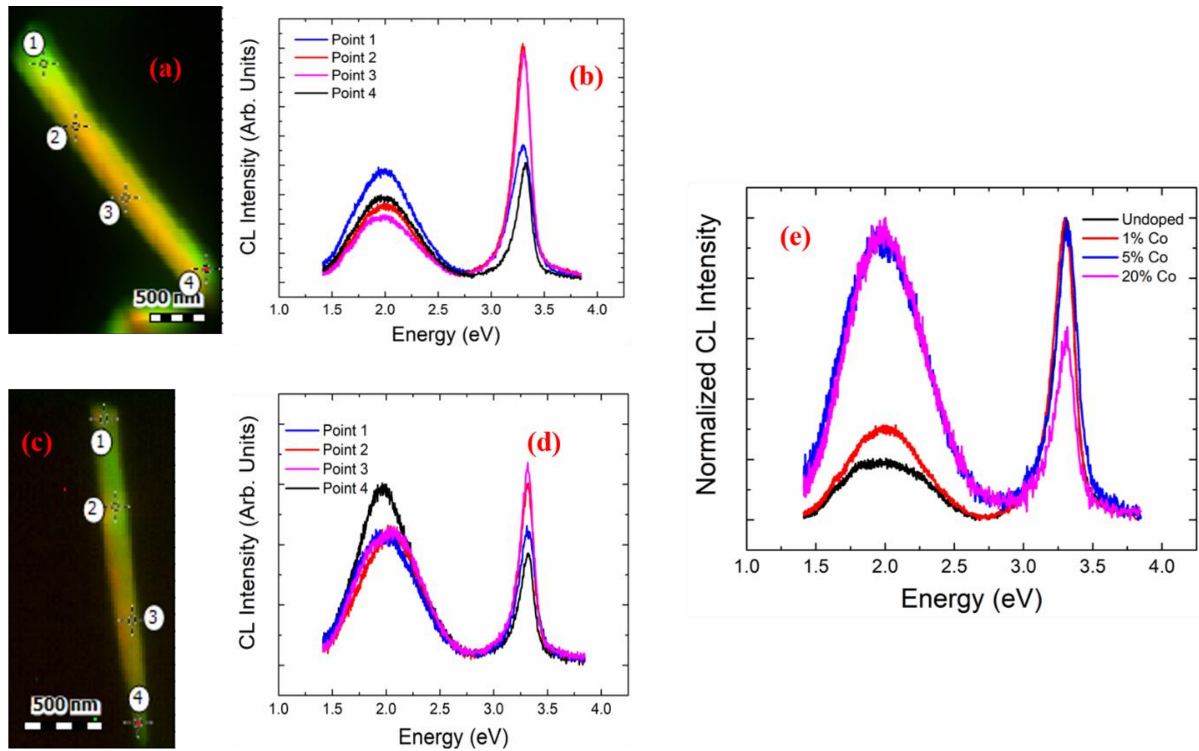

Figure 5. 20. (a) SEM image superimposed with color specific CL emission map of 1% Co-doped ZnO NRs, where red color indicates the NBE emission while the green color indicates the defect band emission, 4 points are numbered along its length and (b) shows the CL emission from these 4 points. (c) SEM image superimposed with color specific CL emission map of 5% Co-doped ZnO NRs, where red color indicates the NBE emission while the green color indicates the defect band emission, 4 points are numbered along its length and (d) shows the CL emission from these 4 points. (e) Normalized CL emission spectra from undoped, 1%, 5% and 20% Co-doped ZnO NRs.

Figure 5. 21 shows the spatial analysis of the energy distribution of the peaks along with standard deviation of the fits for a typical 1% Co-doped ZnO NR measured at 10 K. Figure 5. 21 (a) and Figure 5. 21 (b) shows the fitted peak values of the UV peak using a split Lorentzian and the standard deviation of the peak along the length of the NR, respectively.[176] The split Lorentzian accommodates the line shape of the UV peak better. The peak energy is uniform for UV peak with peak shift spanning about 40 meV with an uncertainty of 1 sigma between 1 meV and 6.5 meV. Figure 5. 21 (c) and Figure 5. 21 (d) show the Gaussian fitted peak values and the standard deviation of the visible peak centered around 1.9 eV, respectively, along the length of the NR. The peak shift spans approximately 45 meV with an uncertainty (1 sigma) below 1 meV. The fits were done using *hyperspy*.[177]

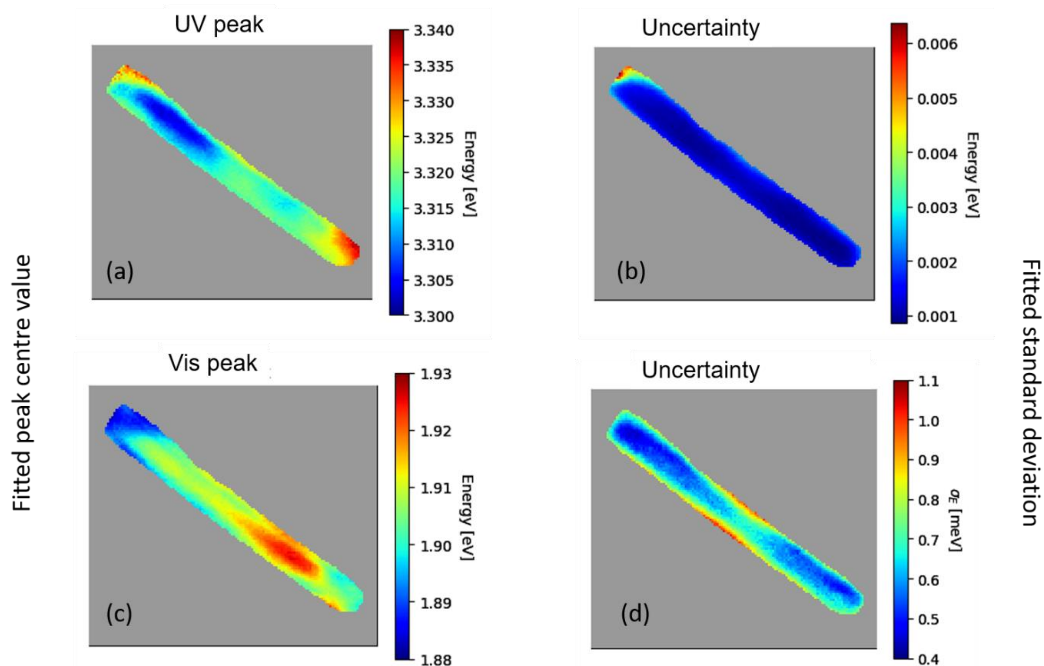

Figure 5. 21. The results of the fitting of the peaks in UV and visible region of the CL emission spectra at 10 K along the length of the NR for a typical 1% Co-doped ZnO NR. (a) the UV peak center values obtained by using a split Lorentzian function for the fitting, (b) standard deviation of the fit for the UV peak, (c) Gaussian fitted peak center values for the visible emission, and (d) standard deviation of the Gaussian peak fit in the visible.

(b) Transient absorption spectroscopy

Figure 5.22 summarizes the results of FTAS measurements at room temperature on the undoped, and Co-doped ZnO NRs. The samples were excited using a pump at 4.51 eV of fluence 260 μJcm^{-2} This figure shows the measurements on 3 samples, including undoped, 1% and 20% Co-doped ZnO NRs. The results on 5% Co-doped ZnO NRs will be discussed later. The 2D false-colormaps show negative signals, indicating a reduction in absorbance after photoexcitation by the pump from carrier (de)population of the (valence) conduction band.

From the 2D colormaps (Figure 5.22 (a), (b) and (c)), it can be seen that the bandgap bleaching red shifts with increased Co-doping values. The optical bandgap values shift from 3.3 eV in undoped ZnO NRs to 3.18 eV and 2.92 eV in 1% and 20% Co-doped ZnO NRs, respectively. Another important feature to notice is the extension of probe absorption in the whole spectral

range for the doped samples while the bleaching falls to zero at 2.5 eV for the undoped ZnO NRs. The TA values at different time delays are shown in Figure 5.22 (d), (e) and (f) for undoped, 1% Co-doped, and 20% Co-doped ZnO NRs, respectively. In 20% Co-doped ZnO NRs the absolute value of ΔA has decreased significantly compared to undoped and 1% Co-doped ZnO NRs.

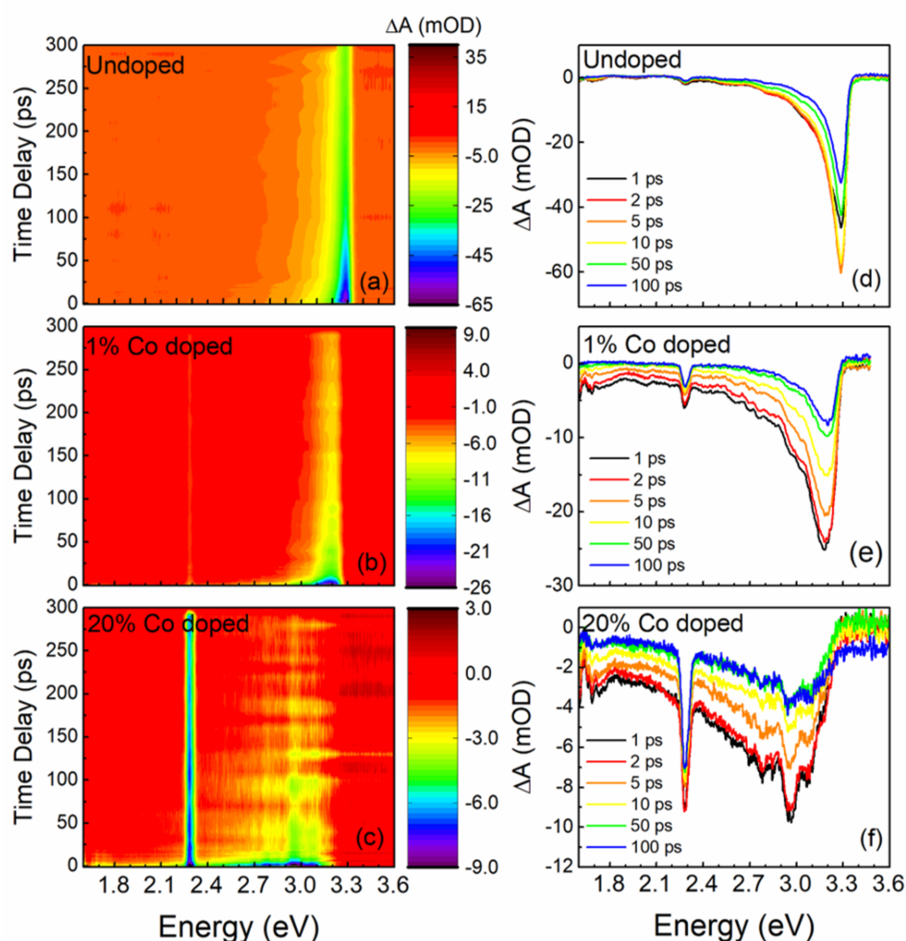

Figure 5. 22. 2D false colormap of the difference in absorbance (ΔA) for (a) undoped, (b) 1 % Co doped and (c) 20 % Co-doped ZnO nanorods. ΔA at different time delays for (d) undoped, (e) 1 % Co-doped and (f) 20 % Co-doped NRs. All samples were excited with a pump of 4.51 eV with a fluence of 260 μJcm^{-2}.

To fully understand the effects of Co-doping on the TA spectra of ZnO NRs the dynamics of the signals must be investigated. For this purpose, the time dependence of ΔA values at

different values of probe energy are studied. The values of ΔA as a function of time delay are plotted and fit with the best fitting exponential decay function. The results are shown in the following section.

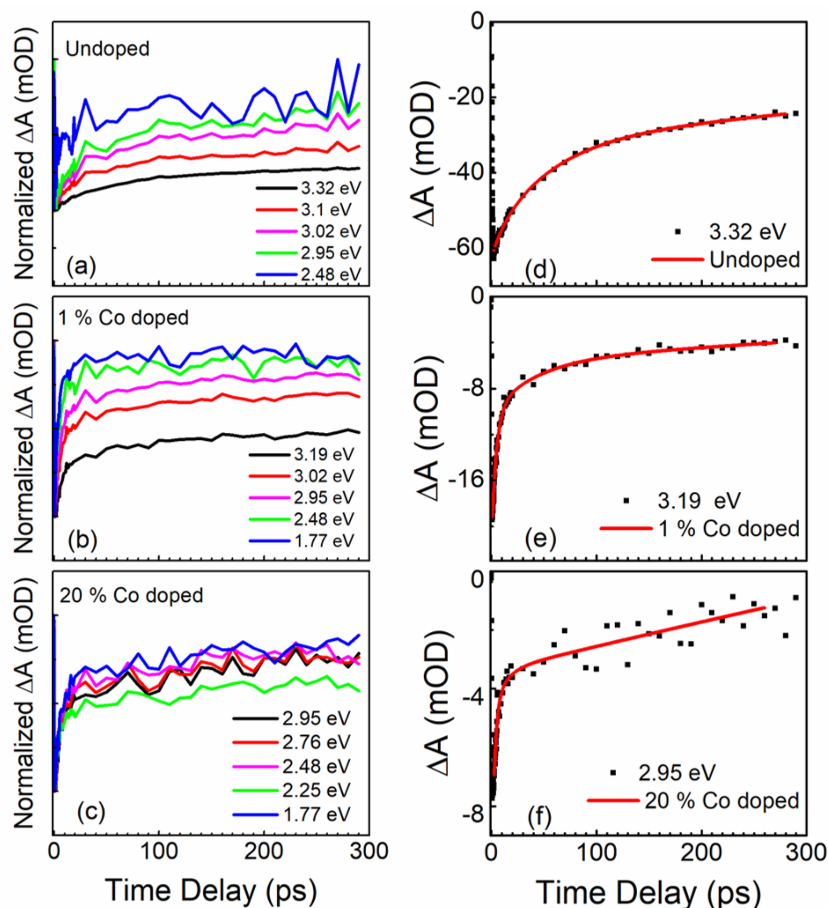

Figure 5. 23. The time dependence of normalized ΔA between {0,1} at different probe energies for (a) undoped, (b) 1% Co-doped and (c) 20 % Co-doped ZnO NRs. Experimental data (black dots) and best fitting models (red line) for the NBE bleaching of (d) undoped, (e) 1% Co-doped and (f) 20% Co-doped ZnO NRs.

The temporal analyses of the absorption bleaching signals are shown in Figure 5. 23. The ΔA signals were fitted with a multiexponential curve as shown in Figure 5. 23 (d), (e), and (f) with three decay constants τ_1, τ_2, and τ_3. The value of τ_1 and τ_2 decreased with increasing Co-concentration. For undoped ZnO NRs, τ_1 and τ_2 were found to be 20 ± 6 ps and 99 ± 18 ps, respectively. The longest component τ_3 was found to be longer than the measurement window

and could not be calculated accurately. The two short components are assigned to decay related to non-radiative pathways, while the last τ_3 is assigned to radiative decay. In the presence of Co-doping, the values of the non-radiative recombination decreases. For 1% Co-doping, τ_1 and τ_2 were found to be 5.4 ± 0.5 ps and 82 ± 14 ps, respectively. For 20% Co – doped ZnO NRs τ_1=4.7 ± 0.7 ps and τ_2=32±14 ps.

Figure 5. 24 shows the results of room temperature TA measurements on 5% Co-doped ZnO NRs. For 5% Co-doped ZnO NRs, a pump at 4 eV was used and a fluence of 260 µJ cm^{-2}.

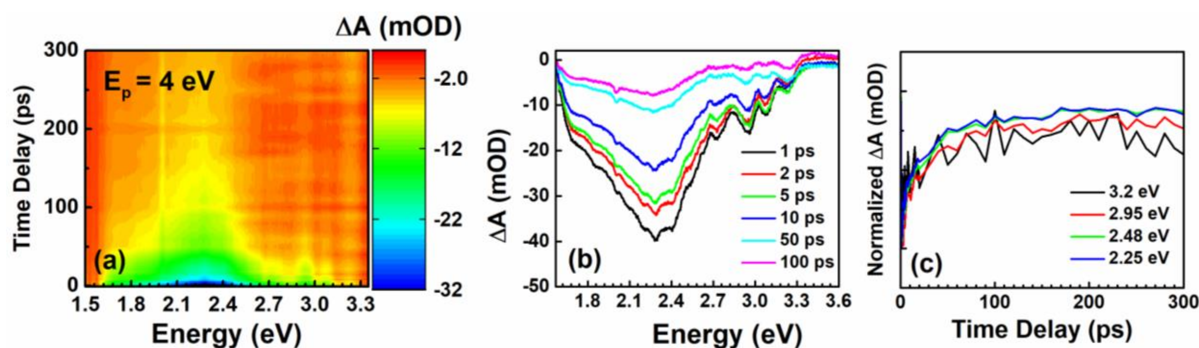

Figure 5. 24. Room temperature FTAS measurements on 5% Co-doped ZnO NRs excited with a pump of 4 eV and fluence of 260µJcm^{-2}. (a) 2D-false colormap of the TA, with probe energy on x axis, and time delay on y axis. (b) The TA measurements at different time delays and (c) the time dependence of ΔA at different probe energies.

Figure 5. 24 (a) shows the 2D false colormap of the ΔA measurements. The bandgap bleaching has red shifted to 3.09 eV. In the TA spectra at different time delays (Figure 5. 24 (b)), however, certain new peaks appear in the TA spectra as well. There is a broad band between 1.6 eV and 2.7 eV, with a peak at 2.35 eV which is attributed to Zn vacancy and a small shoulder at around 2.5 eV attributed to oxygen vacancies.[175] The decay time also follows a probe energy dependent nature as seen in Figure 5. 24 (c). After the multi exponential fit, we find that for the 5% Co-doped ZnO NRs, τ_1=4 ± 0.6 ps and τ_2 =57 ± 18 ps.

Figure 5. 25 presents the summary of the temporal analysis of undoped and Co-doped ZnO NRs. Figure 5. 25 (a) shows the normalized ΔA as a function of delay time. We observe that with increasing Co-doping, the ΔA decay dynamics becomes faster. The shorter decay time constant τ_1 as a function of probe wavelength is plotted in Figure 5. 25(b).

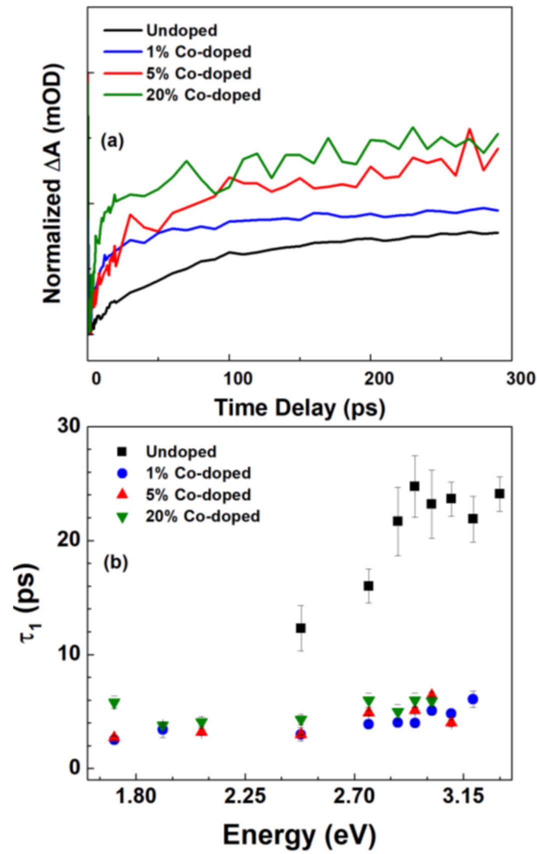

Figure 5. 25. (a) Normalized ΔA as a function of time delay for bandgap bleaching and (b) the probe energy dependence of short time constant for the bleaching decay. The data for Undoped, 1%, 5% and 20 % Co- doped ZnO NRs are represented by black (curve and squares), blue (curve and dots), red (curve and triangles) and green (curve and triangles) respectively.

The undoped ZnO NRs have a higher decay constant τ_1. This value also decreases with decreasing probe energy. The shortest decay constant is dependent on the probe energy for undoped ZnO NRs, like the observations made by Bauer *et al*.[178] The value of τ_1 is much lower for all the doped samples. There is a general trend of decrease of decay time constant with decreasing probe energy. However, for the doped samples this is not as pronounced as in the undoped ZnO NRs. The short decay time τ_1 is attributed to excited carriers getting trapped by the defect states, while τ_2 is attributed to carriers recombining non-radiatively.

(c) Time resolved photoluminescence

TRPL measurements were done by the method of time correlated single photon counting at room temperature. The samples were excited by pulsed laser at 4.51 eV and the NBE bleaching lifetimes were studied. The PL decay was fitted using a double exponential function, also taking into consideration the response function of the instrument (IRF) which is 0.5 ns. Figure 5. 26 shows the results of TRPL for the samples. The Co-doping has no significant impact on the recombination lifetime of ZnO NRs. The best fitting model consists of two decay times. However, the shortest decay time in all samples were found to be less than the IRF and was only used to provide the best possible fit. The black dots represent the undoped ZnO NRs, and the best fit gives the decay time constant as 1.3 ± 0.7 ns. For 1% Co-doped, 5% C-doped and 20% Co-doped, they are 1.1 ± 0.3 ns, 1.1 ± 0.5 ns and 1.2 ± 0.2 ns, respectively. The recombination time is found to be around 1 ns, irrespective of doping in agreement with literature.[179]

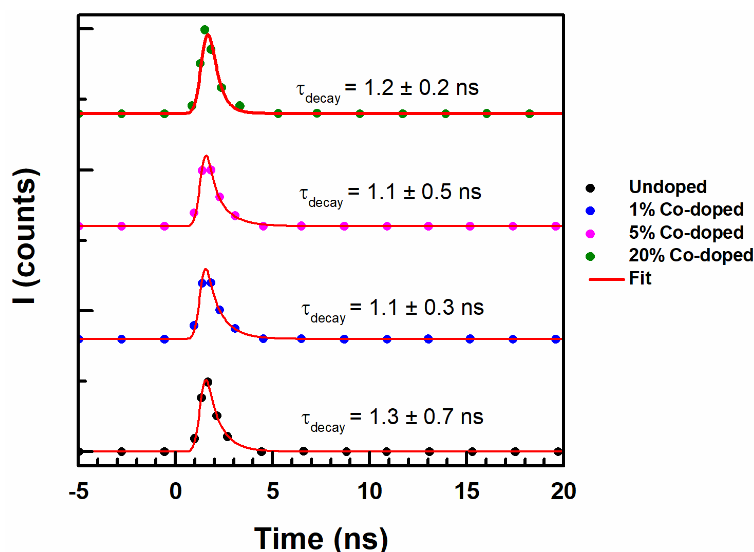

Figure 5. 26. Time resolved PL (TRPL) measurements of undoped (black), 1% Co-doped (blue), 5% Co-doped (magenta), and 20% Co-doped (green) ZnO NRs.

(d) Photoelectrochemical measurements

The PEC measurements were done at the Instituto de Carboquímica (ICB-CSIC), Zaragoza, Spain by Alejandro Galan Gonzalez, and Javier Hernandez Ferrer. Incident photon to charge carrier efficiency (IPCE) is a critical quantity while characterizing materials for photoelectrochemical (PEC) application, such as PEC water splitting. Figure 5. 27 (a) shows

the wavelength dependent IPCE measurements at 1.33 V against the standard reversible hydrogen electrode (RHE) for the doped and undoped ZnO NR samples. The IPCE changes with Co-doping. All the Co-doped samples showed higher IPCE than undoped ZnO NR sample. The highest improvement was noted between 300 nm and 350 nm. 1% Co-doped ZnO NRs show the highest IPCE value in this region, about 51%, with 5% and 20% Co-doped samples following with IPCE of 40%.

Figure 5. 27 (b) shows the shows the electronic response to light exposure for the undoped and Co-doped NRs when illuminated with AM 1.5G and at a voltage sweep between -0.5 V and 1.33 V against standard RHE. The photogenerated current density is also higher for 1% Co-doped ZnO NRs, with a little over 0.1 mAcm^{-2}. The lowest value of photogenerated current is observed for 20% Co-doped ZnO NRs. From PEC characterization, 1% Co-doped ZnO NRs show the best photoresponse.

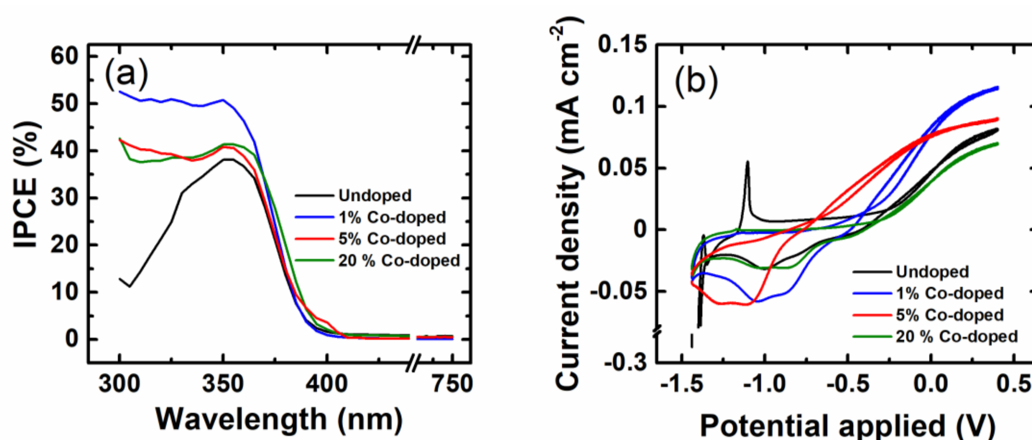

Figure 5. 27. (a) Wavelength dependent IPCE measurements at 1.33 V vs RHE and (b) Cyclic sweeping voltammetry under AM 1.5 G illumination, for undoped and Co-doped ZnO NRs. Black curves: undoped ZnO NRs; blue: 1%, red: 5%, and green: 20%- Co-doped ZnO NRs.

5.2.5 Metal organic framework functionalized Co-doped ZnO nanorods

From the optical and photoelectrochemical measurements, it was seen that the 1 % Co doped ZnO NRs showed the best IPCE and photocurrent density values. This sample was then chosen for further functionalization of the surface to improve its PEC properties to be used in PEC water splitting cell as a photoanode. As mentioned in the introduction, 1% Co-doped ZnO NRs are coated with a metal organic framework (MOF) to improve chemical stability as well as charge separation. MOFs also provide further enhancement of surface area. In this work, the group of zeolitic imidazolate frameworks (ZIF) in the MOF family is exploited, where the

material is called ZIF-8. ZIF-8 consists of Zn nuclei tetrahedrally coordinated by 2-methylimidazole organic linkers. It has been shown that ZIF-8 can be easily integrated as a shell around a ZnO core. In the following sections the synthesis, optical and PEC characterizations are discussed.

5.2.5.1 Synthesis

The synthesis of the core shell NR structure was carried out by Alejandro Galan Gonzalez at Durham university. The 1% Co-doped ZnO NRs are synthesized by the chemical bath deposition mentioned in the section 5.2.2. These NRs are then spin coated with ZIF-8 using a methanol solution containing the imidazole linker onto the ZnO NRs. 1 M of the organic linker(2-methylimidazole) was dissolved in 10 ml methanol with magnetic stirring. 3-5 drops of the imidazole solution were spin-coated onto the NRs at 5000 rpm for 30 s. After spin-coating, two growth processes were performed on a hotplate. First, evaporation of methanol at 65 °C for 5 min. Then, the surface conversion reaction of the ZnO NRs into ZIF-8 at 160 °C for 30 min was performed. The samples were then rinsed with methanol and blow-dried with nitrogen. Figure 5. 28 shows the SEM image of the 1% Co-doped ZnO core with ZIF-8 shell NRs, denoted from now on as ZnO:Co@ZIF-8. The MOF shell appears as the roughened surfaces.

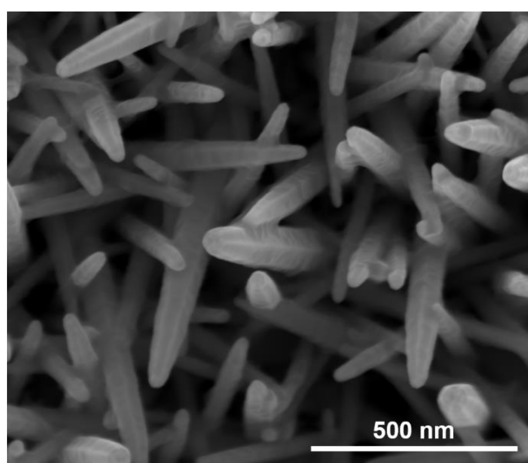

Figure 5. 28. SEM image of ZnO:Co@ZIF-8 core shell NRs

5.2.5.2 Optical and photoelectrochemical characterization

The optical and PEC characterization were performed on the core shell NRs with the methods explained for the Co-doped NRs in section 5.2.3. CL, FTAS and amperometric measurements were done on the ZnO:Co@ZIF-8 core shell NRs.

5.2.5.3Results

(a) Cathodoluminescence measurements

Figure 5. 29 shows the results of room temperature CL measurement on the ZnO:Co@ZIF-8 core shell NRs. The NRs were transferred onto a conductive silicon substrate to avoid charge build-up during excitation by the electron beam. For sake of comparison the CL of ZnO:Co@ZIF-8 core shell NRs is shown along with the CL of 1% Co-doped ZnO NRs. The samples were excited using a 5 keV electron beam. The CL spectra is extracted from 3 points along the length of the NRs. Figure 5. 29 (a) shows the CL spectra from the three points along the length of a transferred ZnO:Co@ZIF-8 core shell NR and Figure 5. 29 (b) shows the CL spectra extracted form 3 points along the length of a transferred 1 % Co-doped ZnO NR. The CL intensities are normalized to the NBE emission intensity.

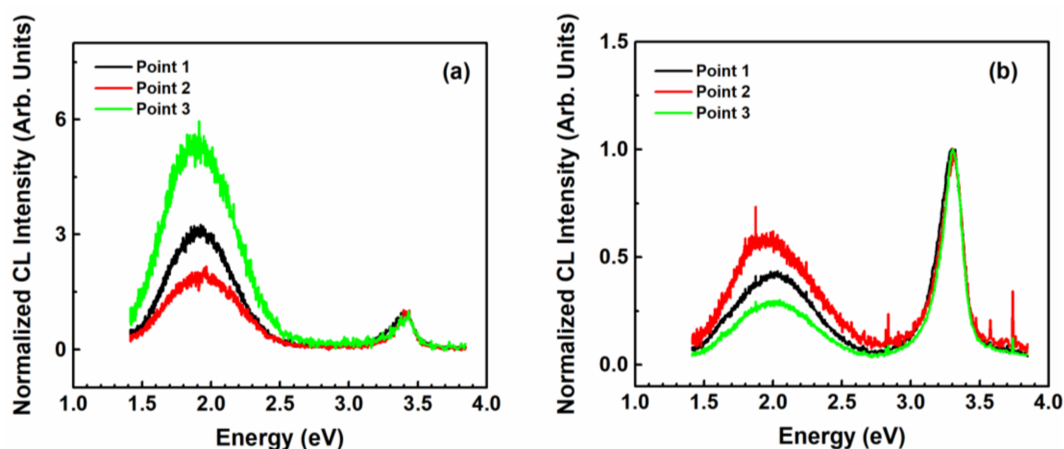

Figure 5. 29. Room temperature CL spectra extracted from 3 points along the length of (a) the ZnO:Co@ZIF-8 core shell NR and (b) 1% Co-doped ZnO NR. The CL intensities in the spectra are normalized to the NBE emission intensity.

The two samples are spectrally similar, in that we can observe both the NBE and the defect bands. However, for the ZnO:Co@ZIF-8 core shell NR the defect band contribution is more

prominent than the NBE emission. This aspect is made clear by normalizing the spectra to the NBE emission intensity. The overall intensity of the emission is also significantly reduced in the case of the ZnO:Co@ZIF-8 core shell NR as seen from the panchromatic CL intensity map in Figure 5. 30. Figure 5. 30. (a) and Figure 5. 30. (b) show the panchromatic CL map at room temperature for a 1% Co-doped ZnO NR and a ZnO:Co@ZIF-8 core shell NR.

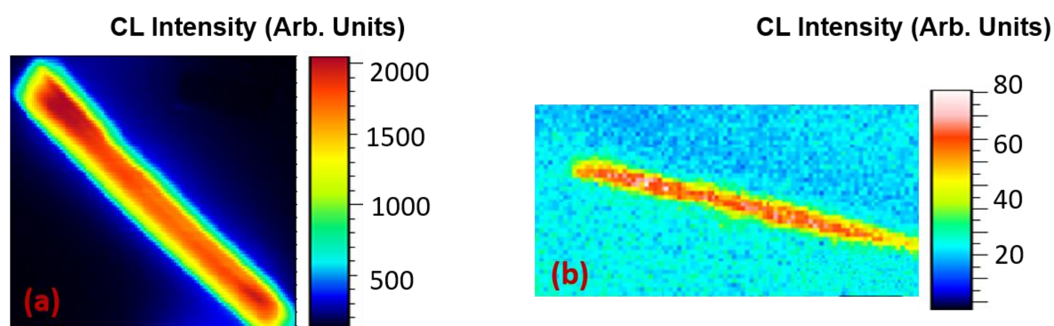

Figure 5. 30. The panchromatic CL map superimposed on the SEM image of a transferred NR for (a) 1% Co- doped ZnO NR and (b) ZnO:Co@ZIF-8 core shell NR.

(b) Transient absorption spectroscopy

Figure 5. 31 presents the results of FTAS measurements on ZnO:Co@ZIF-8 core shell NRs. The measurements were done on as-grown samples on ITO. We see a strong bleaching at 3.08 eV and a less intense bleaching at the bandgap of ZnO, probably due to the seed layer. The TA extends over the visible region. For the decay lifetime dynamics, it was sufficient to fit with a double exponential. The two decay time constants are τ_1=10 ± 4 ps and τ_2=70± 17 ps. While the short time constants τ_1 lies above the value for 1% Co-doped ZnO NRs, it is shorter than that for the undoped ZnO NRs, and τ_2 is shorter than that of both undoped and 1% Co-doped ZnO NRs. Also, the huge reduction in the luminescence intensity, combined with the lack of a longer decay constant (τ_3) points to the possibility that in ZnO:Co@ZIF-8 core shell NRs the carriers recombine non-radiatively.

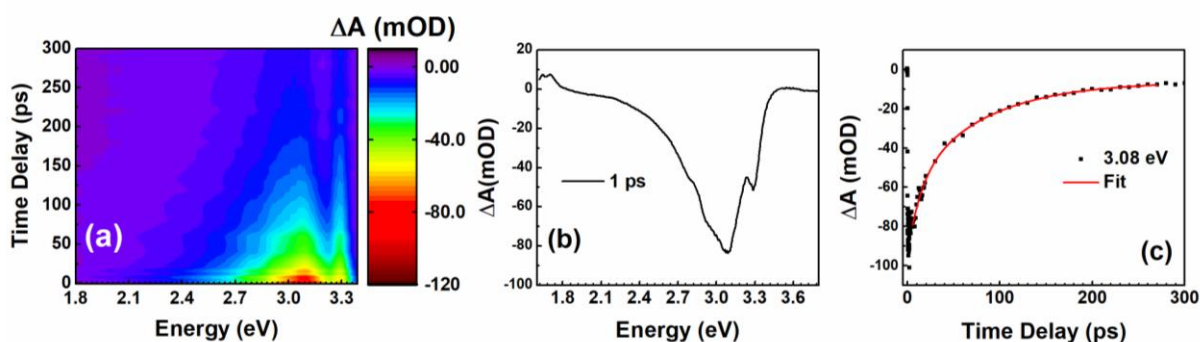

Figure 5. 31. Room temperature FTAS measurements on ZnO:Co@ZIF-8 core shell NRs excited with a pump of 4 eV and fluence of 260µJcm-2. (a) 2D-false colormap of the TA, with probe energy on x axis, and time delay on y axis. (b) The TA measurements at 1 ps time delay between the pump and the probe and (c) shows the time dependence of ΔA at bandgap bleaching.

(c) Photoelectrochemical measurements

Figure 5. 32 (a) shows the wavelength-dependent IPCE measurements at 1.33 V against the standard RHE for the ZnO:Co@ZIF-8 core shell NRs along with the IPCE for undoped and 1% Co-doped ZnO NRs.

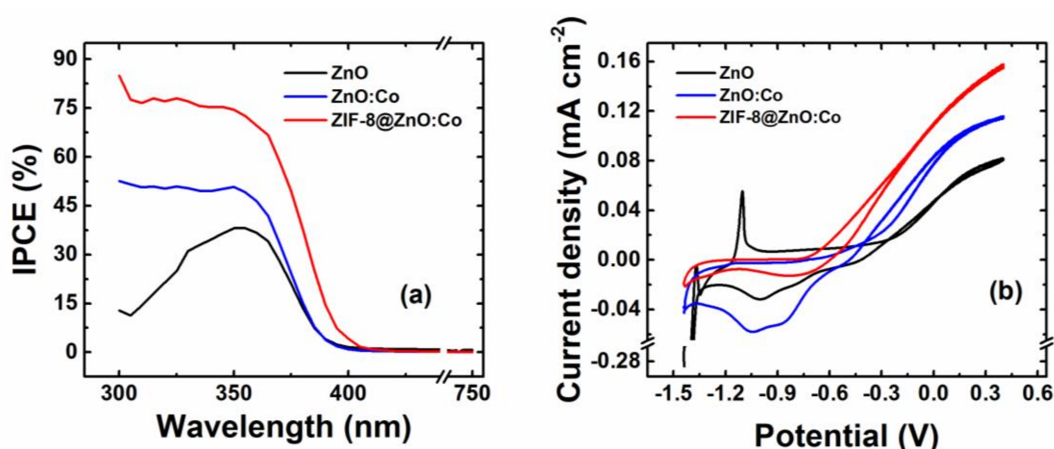

Figure 5. 32. (a) Wavelength dependent IPCE measurements at 1.33 V vs RHE and (b) Cyclic sweeping voltammetry under AM 1.5 G illumination, black curves for undoped ZnO NRs; blue curves for 1%Co-doped ZnO NRs and red ZnO curves for Co@ZIF-8 core shell NRs.

The ZnO:Co@ZIF-8 core shell NRs (red curve) has the highest IPCE value along with a red shift in the IPCE values up to 405 nm (corresponding to the red shift in absorption). The IPCE increases to 75% at 350 nm and to a remarkable 85% at 300 nm when compared to undoped and 1% Co-doped ZnO NRs. Similarly, Figure 5. 32 (b) shows the cyclic voltammetry measurements for all three samples and the current densities achieved for ZnO:Co@ZIF-8 core shell NRs are the highest at about $0.16 mAcm^{-2}$.

5.2.6 Discussion

In the second section of this chapter 5, I have studied the optical properties of Co-doped ZnO NRs. I have also presented the data on the photoelectrochemical characterization of these NRs performed at two different collaborative institutes. I have also described the results obtained for a MOF-functionalized Co-doped ZnO NRs. In this section I will discuss the results obtained in detail.

CL spectra remained spectrally similar in the presence of Co-doping. However, the relative intensity of the defect related emission increased with increasing Co-doping. The defects usually present in ZnO are vacancies, interstitials and antisites of both zinc and oxygen[180]. Oxygen vacancies can be neutral (V^0_O), singly charged (V^+_O) or doubly charged (V^{++}_O).[174]Though the exact source of visible emission has been debated largely, the emission centered around 2 eV is assigned to oxygen vacancies and Zn interstitial related transitions .[174,178,181–183]Since the samples are grown by chemical bath deposition where the Zn atoms are substituted by Co atoms whose ionic radii is smaller, this might have led to the formation of oxygen vacancies and Zn interstitials.[184] Another important aspect is the reduction of the relative intensity of NBE emission with increased doping. This might point to non-radiative recombination pathways being favored in the presence of Co-doping. There have been several studies on the effects of Co-doping on the optical properties of ZnO. Several groups have reported the presence of sharp d-d transitions due to Co^{2+} in the absorption or emission spectra, centered around 1.9 eV, 2.25 eV and 2.07 eV.[164,185] In the samples measured for this thesis, the d-d transition bands are not visible in the CL or TA measurements. This could be because of the strong signals from the defect band, as well as NBE. There have been reports also of other works where the d-d transition was not observed.[164,186,187]

Further optical characterization was carried out by measuring the room temperature TA spectra. The TA spectra showed a red shift of the absorption bleaching. The increase in surface defects density, observed by the CL, is also reflected in the broadening of the absorption bleaching, which shows a long tail of bleaching up to 1.65 eV. The red shift of the NBE absorption bleaching is attributed to an increased sp-d exchange interaction in the presence of Co^{2+} [169,170]. This interaction is between the band electrons of the ZnO with the d-orbital electrons of the

Co^{2+} leading to a positive and negative correction of valence and conduction band, respectively. Another explanation for the narrowing of the bandgap combined with increasing surface defects or oxygen vacancies is that the delocalized defect states can overlap with the valence band leading to the narrowing of the bandgap.[188] The dynamics of the ΔA signal were fit with multiexponential curves, and it was observed that the dynamics became faster with increased Co-doping concentration. τ_1 is the short component of the decay function and is more affected by the doping than τ_2. τ_1 is also wavelength -dependent and is attributed to carrier trapping by oxygen vacancies. The second component, τ_2, is attributed to non-radiative recombination channels that depend on the doping contents like Co-clusters.[189] Since the Co-doping had a measurable effect on the fast carrier dynamics, its effect on radiative recombination will be negligible. The TRPL measurements were carried out on these NRs to verify this, and the Co-doping showed no effect on the radiative recombination lifetimes.

Oxygen vacancies and surface defects play a very important role in photocatalytic activity, especially in the efficiency of ZnO as a PEC material.[190,191] This is attributed both to enhanced light absorption as well as the increased carrier trapping. As shown in CL and FTAS measurements, there is both increased absorptions, as well as increased carrier trapping in the presence of increased doping. This was then verified by PEC measurements. The 1% Co-doped ZnO NRs showed maximum IPCE as well as photocurrent density. The IPCE and photocurrent density increased for 1% Co-doping after which it decreased in the case of 5% and 20 % Co-doped ZnO NRs. This could be because of excess non-radiative recombination sites resulting in decrease in photocurrent density.

Through these measurements, 1% Co-doped ZnO NRs were found to be most suitable for PEC applications. This was further functionalized with the help of a MOF shell around the ZnO NR. This core shell structure provides better charge separation, and better chemical stability. From the CL measurements, it was seen that while spectrally similar i.e., the NBE and defect bands being present, the ratio of NBE to defect band emission significantly reduces in the presence of the MOF framework around the NRs. The intensity of the CL emission also significantly reduces. This could point to the creation of more non-radiative recombination pathways. The lack of a long decay time constant in the TA measurements also adds to this observation. There is also a stronger red shift in the bandgap emission in case of ZnO:Co@ZIF-8 core shell NRs. The appearance of more defects in the CL emission could be linked to the further red shift in the ZnO:Co@ZIF-8 core shell NRs as compared to 1% Co-doped ZnO NRs. With more surface defects and narrower bandgap, the PEC performance was also improved, which was seen in the wavelength dependent IPCE measurements as well as in the values of photocurrent density. This increased efficiency can be attributed to the increased charge separation in the presence of the MOF shell. The light excitation creates electron-hole pairs in the ZnO:Co@ZIF-8 core shell NRs. The presence of surface defects with Co-doping, traps the electrons, while the ZIF-8 shell can move the holes from the core to the surface, making them available for reaction

with the electrolyte. For the transfer of holes from valence band of Co-doped ZnO to the ZIF-8 shell the energy difference has to be small. From Mott-Schottky measurements the energy difference is found to be about 0.25 eV,[192] which is a small enough barrier for the photogenerated holes. Similarly, the electrons are transferred from the shell to the core because of the position of conduction bands. The conduction band is formed by the empty orbitals of Zn, hence the electrons travel to the Zn cluster and then to the core. Figure 5. 33 shows the schematic of the charge transfer mechanism suggested above. This synergetic presence of Co-doping along with MOF shell helps improves the photoresponse of ZnO making it a viable candidate in PEC water splitting. This is demonstrated by the 75% IPCE at 350 nm which is exceptional for a ZnO based photoanode. The significant improvements in the IPCE could be directly linked to the modifications of optoelectronic properties in the presence of Co-doping, combined with the MOF-functionalization.

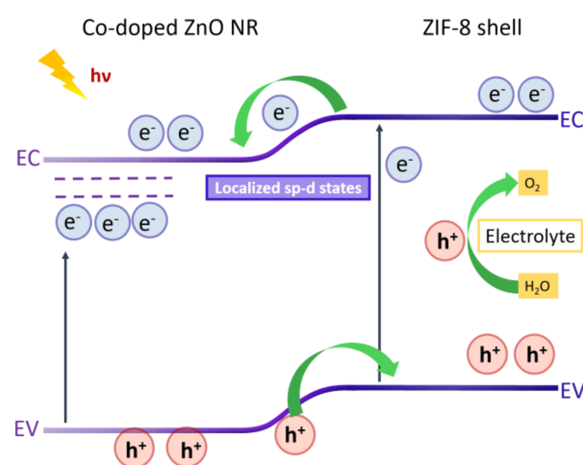

Figure 5. 33. Schematic diagram of band alignment and flow of carriers in ZnO:Co@ZIF-8 core shell NRs.

By systematically studying the optical properties of Co-doped ZnO NRs, the impact of Co-doping on the optoelectronic properties are studied. From the optical measurements it was evident that that the Co-doping created more surface defects or oxygen vacancies in the ZnO NRs. By combining different optical measurements, and comparing with the PEC measurements, the importance of surface defects in improving the efficiency of PEC functionality of a photoanode was established. At the same time, through PEC measurements, one can see that in samples that showed evidence of high amount of non-radiative recombination rates (~20% Co-doped) in optical measurements, the PEC efficiencies also dropped.

5.3 Conclusions

In chapter 5 I have studied the optical properties of functionalized semiconductor NWs. Two types of functionalization were studied:

1. Semiconductor NWs decorated with plasmonic NPs (ZnSe NWs decorated with Ag/Au NPs.
2. Doping of semiconductor NWs

The Ag-decorated and Au-decorated ZnSe NWs were studied to understand the importance of the resonance between the plasmonic LSPR and the semiconductor bandgap for efficient energy transfer between the metal and semiconductor. TA measurements and LTPL measurements showed the fingerprints of efficient energy transfer from Ag NPs to ZnSe NWs, while the Au-decorated ZnSe NWs did not show similar modifications. The most interesting aspects of the measurements were the decrease in the decay time constant of bleaching signal in a large spectral window where the LSPR and the absorption band of the semiconductor overlapped. The faster decay was attributed to the possible enhancement of carrier-phonon coupling in the presence of resonant plasmonic NPs. Another evidence for the enhancement of the coupling of electrons and phonons in the system is the appearance of the LO-phonon replicas in the LTPL spectra. By using Au-NPs, which forms similar Schottky barrier conditions with ZnSe as Ag NPs, one could verify that all the changes observed in the optical measurements require a resonant condition between the LSPR and the semiconductor bandgap because similar changes were not observed in ZnSe NWs decorated with Au NPs whose LSPR is not resonate with the bandgap of ZnSe.

Co-doped ZnO NRs were studied for the photoelectrochemical applications, especially to be used as a photoanode in a PEC cell for water splitting. Different concentrations of Co precursors were introduced along with Zn precursors in a chemical bath growth, where the Co^{2+} competitively substitutes Zn^{2+} ions and form Co-doped ZnO NRs. Through optical and PEC characterization, the optical ratio of Co^{2+} to Zn^{2+} is found to be 1%. The drastic changes in the intensity of defect bands along with the red shift of the optical absorption and increased carrier trapping in Co-doped ZnO NRs point to the importance of defects while tailoring the properties of a semiconductor. Through systematic optical measurements it was possible to understand the reason behind the enhancement of PEC performance of Co-doped ZnO NRs.

Chapter 6   Conclusions and Outlook

The present PhD thesis reports the study of the optical properties, with a major focus on the ultrafast carrier dynamics, of semiconductor nanowires of different materials. The materials are studied with two main aims in mind, (i) understanding their fundamental properties, and (ii) characterizing their properties for applications in NW based devices. NWs of Si, InP, GaAs, GaAsP, ZnSe, and ZnO were studied.

Starting with one of the most fundamental semiconductor materials, Si, the thesis progressed through studying photoexcitation in III-V compound semiconductors and finished by exploring functionalized NWs of group II-VI semiconductors. The study of the behavior of photoexcited carriers in these nanostructures were done with the help of ultrafast laser as a pump and probe, allowing one to visualize the temporal evolution of carriers at very short time delays after pump excitation. In some cases, the study of the carrier dynamics via pump-probe experiments were accompanied by photo- and or cathodoluminescence and time-resolved photoluminescence.

The effects of photo excitation in the optical properties of Si NWs were studied using fast transient absorption. The TA measurements in the range of 1.5 – 3.5 eV were studied using a pump excitation below the direct bandgap energy. By observing the absorption bleaching signal at the energy of direct bandgap transition in Si after exciting using a pump with energy much lower than the direct bandgap, and comparing the results with those obtained for energies close or above the direct bandgap energy, it was possible to disentangle the hole and the electron contributions to the dynamics of carrier relaxation. In particular, it was shown that the electron dynamics is faster than the hole dynamics. This thesis also presented introductory results on ultrafast spectroscopy of ultrathin Si NWs. This topic needs to be elaborated further, with a systematic TA spectroscopy to study carrier-carrier interactions, carrier-phonon interaction, and carrier recombination to understand the effects of quantum confinement of both carriers and phonons. The lack of more samples, also due to the difficulties made by the global Covid-19 crisis, has limited my research that I plan to resume in future with the study of the dependence on the wire diameter.

The III-V materials were studied to understand their carrier cooling rates, and to distinguish the optical properties of different crystal phases of the same material. In InP NWs of ZB and WZ crystal structure, TA spectroscopy allowed probing different electronic transitions and their corresponding temporal behaviors. The study of carrier cooling rates in GaAsP NWs allowed the establishment of inverse dependence of NW diameter on the carrier cooling rates, particularly showing that thinner wires can sustain hot carriers at elevated temperature for longer times. The carrier temperature at which the phonon bottleneck takes place is also

evaluated for NWs of different diameter. This thesis also presented the successful observation of the two critical points E1 and E1 + Δ in GaAs in the form of absorption bleaching. Future studies on GaAs will involve the TA measurements in both visible and NIR region, to learn the photoinduced processes at these energies in the time scale of hundreds of femtoseconds to few nanoseconds. A modification of the experimental set-up is necessary to complete the investigation of the carrier dynamics in InP and GaAs NWs. This improvement will be done in the next months and will allow the transient absorption measurements around 800 nm.

Finally, the study of functionalized NWs is performed using ultrafast spectroscopic and other optical techniques. Plasmonic NP decorated ZnSe NWs were investigated using both LTPL and TA measurements. The results in this thesis establish a strong evidence for an efficient energy transfer mechanism that enhances phonon interaction in semiconductor when the LSPR of the metal NPs are resonant with the bandgap of the semiconductor.

The final part of this thesis presented the systematic modification of the optoelectronic properties of ZnO NRs by introducing different concentrations of Co-dopant. FTAS and CL analysis showed clear modification of both stationary and transient optical properties through the creation of more surface defects upon Co-doping of ZnO NRs. It was shown that with the introduction of about 20% Co^{2+} in the growth solution of ZnO, the bandgap can be reduced from 3.3 eV to 2.95 eV. CL measurements showed the enhancement of defect related contributions with increased Co-doping. PEC characterization of Co-doped ZnO NRs showed that the presence of 1% Co-dopant in the growth solution provides an enhanced IPCE and photocurrent density compared to undoped ZnO NRs. These Co-doped ZnO NRs were further functionalized using a metal organic framework for PEC applications. The optical measurements were also carried out on the MOF functionalized 1% Co-doped ZnO NRs, which provided a 75% IPCE value at 350 nm compared to 38% observed for undoped ZnO NRs. By comparing the PEC measurements with the optical measurements, the importance of surface states in enhancing PEC efficiency is also understood.

In conclusion, this thesis reported experimental results on the optical properties of semiconductor NWs that show their importance as a functional material structure, as well as an interesting system to study new physics.

List of Publications

1. **A. K. Sivan,** A. Galan-Gonzalez, L. Di Mario, N. Tappy, J. Hernández-Ferrer, D. Catone, S. Turchini, A. M. Benito, W. K. Maser, S. E. Steinvall, A. F. I Morral, A. J. Gallant, D. A. Zeze, D. Atkinson, F. Martelli, *Optical properties and carrier dynamics in Co-doped ZnO nanorods*, accepted manuscript in *Nanoscale Advances*: https://doi.org/10.1039/D0NA00693A

2. D. Catone, L Di Mario, F. Martelli, P. O'Keeffe, A. Paladini, J. S Pelli Cresi, **A. K. Sivan**, L. Tian, F. Toschi, S. Turchini, *Ultrafast optical spectroscopy of semiconducting and plasmonic nanostructures and their hybrids*, accepted manuscript, *Nanotechnolog*, https://iopscience.iop.org/article/10.1088/1361-6528/abb907

3. V. Campanari, A. Agresti, S. Pescetelli, **A. K. Sivan**, D. Catone, P. O'Keeffe, S. Turchini, A. Di Carlo, F. Martelli, *Photoluminescence of MAPbI3: a semiconductor science and technology point of view,* manuscript submitted for publication. Preprint on arxiv: https://arxiv.org/ftp/arxiv/papers/2008/2008.09009.pdf

4. A. Galan-Gonzalez, **A. K. Sivan**, J. Hernández-Ferrer, L. Bowen, L. Di Mario, F. Martelli, A. M. Benito, W. K. Maser, M. U. Chaudhry, A. Gallant, D. A. Zeze, and D. Atkinson*,* Cobalt-Doped ZnO Nanorods Coated with Nanoscale Metal-Organic Framework Shells for Water-Splitting Photoanodes, *ACS Appl. Nano Mater*, 3, 7781–7788 (2020), https://pubs.acs.org/doi/10.1021/acsanm.0c01325.

5. **A. K Sivan**, L Di Mario, D Catone, P O'Keeffe, S Turchini, S Rubini, F. Martelli, Plasmon-induced resonant effects on the optical properties of Ag-decorated ZnSe nanowires*, Nanotechnology* 31, 174001 (2020), https://iopscience.iop.org/article/10.1088/1361-6528/ab68ba/meta.

6. L. Tian, L. Di Mario, **A. K. Sivan**, D. Catone, P. O'Keeffe, A. Paladini, S. Turchini, F. Martelli, Carrier dynamics in silicon nanowires studied via femtosecond transient optical spectroscopy from 1.1 to 3.5 eV, *Nanotechnology* 30, 214001 (2019), https://iopscience.iop.org/article/10.1088/1361-6528/ab044a/meta.

Appendix A
Optical measurements

A.1 Optical parametric amplifier

An OPA is used to produce laser light of tunable wavelength through an optical amplification process. The OPA used for experiments in this thesis is the OPerA-Solo from Coherent. This OPA emits light from the UV to IR spectral regions.

An OPA amplifies a seed laser of frequency, ω_s with the help of a pump pulse with frequency, ω_s, where $\omega_s < \omega_p$ with the help of a non-linear crystal. As a pump, the output of the regenerative amplifier at 800 nm is used. In an OPA, the seed laser and pump laser combine to form an amplified signal with frequency, ω_{signal}, where the $\omega_s = \omega_{signal}$. A pulse called idler pulse with frequency, ω_{idler} and the attenuated pump pulses are also produced at the output due to energy conservation rules. Figure A.1 shows the energy transfer from high intensity pump to the seed beam, resulting in the amplified signal along with the idler signal.

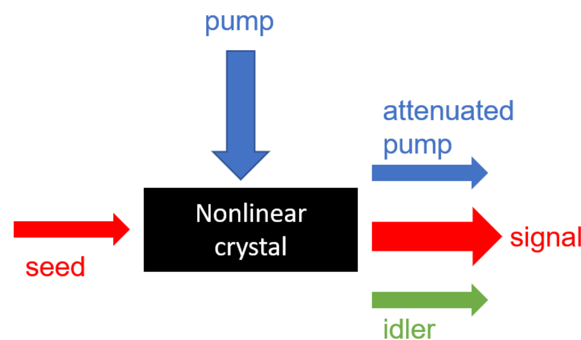

Figure A. 1. Optical parametric amplification of seed beam from pump beam to signal beam.

For the experimental setup used in this thesis, the 800nm output of the regenerative amplifier goes into the input port of the OPA. Initially upon entry into the OPA, the beam splits into 2, ~80-98 % to be used as pump, and the remaining to derive the seed pulse. The small portion transmitted to be the seed pulse gets focused into a sapphire plate to generate the white light continuum. The white light and the pump are focused on a BBO crystal to undergo parametric amplification.

Inside a BBO crystal the white light is preamplified, using a collinear geometry for the intersection of white light and pump. This helps the preamplified white light (signal) to be separated easily from the attenuated pump, and idler signals. The wavelength of the signal

depends on the wavelength of the white light that overlaps with the pump. This can be controlled by adjusting the delay between the pump and white light. Using a computer controlled retro reflector, the time delay of the white light is controlled before interacting with the pump. The output at this stage has only 0.5-3 μJ energy. This signal is then power amplified using a second non-linear crystal. At this stage the wavelength of the output signal is only tuned in the IR region (1160 nm-1600 nm) and of idler in the range 1600 nm - 2600 nm.

However, more wavelength ranges can be accessed using several integrated wavelength extensions in the OPA. The wavelength extensions can be produced using frequency mixers. Frequency mixer is a computer-controlled stage with non-linear crystals which are rotated at different angles allowing for the mixing of different frequencies depending upon the demanded output allowing to produce different wavelength as needed. A range of signals can be produced with processes such as sum frequency (SF), second harmonic (SH), second harmonic of sum frequency, fourth harmonic (FH) and difference frequency (DF) generations of both signal and idler. The processes are as follows involving 2 pulses with frequencies ω1 and ω2 in a non-linear medium,

1. Sum frequency:

$$\omega 1 + \omega 2 = \omega 3$$

2. Second harmonic:

$$\omega 1 + \omega 1 = 2 * \omega 1 = \omega 2$$

3. Fourth harmonic:

$$2 * (\omega 1 + \omega 1) = \omega 2$$

4. Difference frequency:

$$\omega 1 - \omega 2 = \omega 3$$

5. Second harmonic of sum frequency:

$$2 * (\omega 1 + \omega 2) = \omega 3$$

For example, with the signal in the range of 1160 nm-1600 nm, SH generation can create output in the range of 580 nm-800nm

A.2. Transmittance and Reflectance of Si NWs

The transmittance and reflectance of Si NWs, adapted from the doctoral thesis of Dr. Lin Tian.[80]

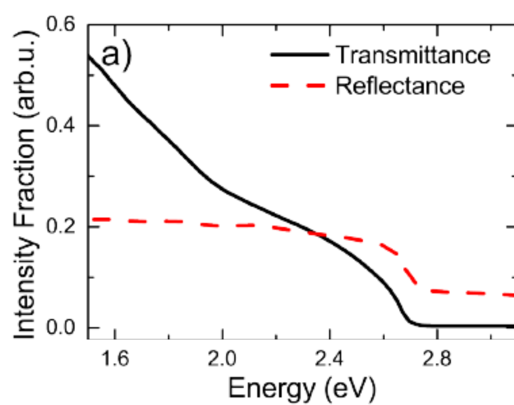

Figure A. 2. The trasnmittance and reflectance of Si NWs.

.

Bibliography

[1] R.S. Wagner and W.C. Ellis, Appl. Phys. Lett. **4**, 89 (1964).

[2] M.S. Gudiksen and C.M. Lieber, Annu. ReV. Phys. Chem **279**, 8801 (1998).

[3] M.S. Gudiksen and C.M. Lieber, J. Am. Chem. Soc. **122**, 8801 (2000).

[4] X. Duan and C.M. Lieber, Adv. Mater. **12**, 298 (2000).

[5] Y. Cui, L.J. Lauhon, M.S. Gudiksen, J. Wang, and C.M. Lieber, Appl. Phys. Lett. **78**, 2214 (2001).

[6] M. Law, J. Goldberger, and P. Yang, Annu. Rev. Mater. Res. **34**, 83 (2004).

[7] K. Pemasiri, M. Montazeri, R. Gass, L.M. Smith, H.E. Jackson, J. Yarrison-Rice, S. Paiman, Q. Gao, H.H. Tan, C. Jagadish, X. Zhang, and J. Zou, Nano Lett. **9**, 648 (2009).

[8] M. Yazawa, M. Koguchi, A. Muto, M. Ozawa, and K. Hiruma, Appl. Phys. Lett. **61**, 2051 (1992).

[9] M. Yazawa, M. Koguchi, A. Muto, and K. Hiruma, Adv. Mater. **5**, 577 (1993).

[10] T.J. Trentler, K.M. Hickman, S.C. Goel, A.M. Viano, P.C. Gibbons, and W.E. Buhro, Science (80-.). **270**, 1791 (1995).

[11] Y. Xia, P. Yang, Y. Sun, Y. Wu, B. Mayers, B. Gates, Y. Yin, F. Kim, and H. Yan, Adv. Mater. **15**, 353 (2003).

[12] P. Yang, R. Yan, and M. Fardy, Nano Lett. **10**, 1529 (2010).

[13] M.S. Gudiksen, L.J. Lauhon, J. Wang, D.C. Smith, and C.M. Lieber, Nature **415**, 617 (2002).

[14] J. Johansson and K.A. Dick, CrystEngComm **13**, 7175 (2011).

[15] Y. Wu, R. Fan, and P. Yang, Nano Lett. **2**, 83 (2002).

[16] F. Jabeen, V. Grillo, S. Rubini, and F. Martelli, Nanotechnology **19**, (2008).

[17] C. Yang, Z. Zhong, and C.M. Lieber, Science (80). **310**, 1304 (2005).

[18] P. Caroff, M.E. Messing, B. Mattias Borg, K.A. Dick, K. Deppert, and L.E. Wernersson, Nanotechnology **20**, 495606 (2009).

[19] B.J. Ohlsson, M.T. Björk, A.I. Persson, C. Thelander, L.R. Wallenberg, M.H. Magnusson, K. Deppert, and L. Samuelson, in *Phys. E Low-Dimensional Syst. Nanostructures* (North-Holland, 2002), pp. 1126–1130.

[20] E.P.A.M. Bakkers, J.A. Van Dam, S. De Franceschi, L.P. Kouwenhoven, M. Kaiser, M. Verheijen, H. Wondergem, and P. Van Der Sluis, Nat. Mater. **3**, 769 (2004).

[21] M.T. Chen, M.P. Lu, Y.J. Wu, J. Song, C.Y. Lee, M.Y. Lu, Y.C. Chang, L.J. Chou, Z.L. Wang, and L.J. Chen, Nano Lett. **10**, 4387 (2010).

[22] J. Wallentin, Doping of Semiconductor Nanowires, Lund University, 2012.

[23] J. Johansson, Z. Zanolli, and K.A. Dick, Cryst. Growth Des. **16**, 371 (2016).

[24] P. Masri, Surf. Sci. Rep. **48**, 1 (2002).

[25] New York Times (2020), https://www.nytimes.com/2020/09/20/arts/design/climate-clock-metronome-nyc.html

[26] https://www.mcc-berlin.net/en/research/co2-budget.html

[27] H. Ritchie and M. Roser, Our World Data (2017).

[28] L. Tsakalakos, J.E. Balch, J. Fronheiser, M.-Y. Shih, S.F. LeBoeuf, M. Pietrzykowski, P.J. Codella, B.A. Korevaar, O. Sulima, J. Rand, A. Davuluru, and U.D. Rapol, J. Nanophotonics **1**, 1 (2007).

[29] O.L. Muskens, J.G. Rivas, R.E. Algra, E.P.A.M. Bakkers, and A. Lagendijk, Nano Lett. **8**, 2638 (2008).

[30] G. Mariani, A.C. Scofield, C.H. Hung, and D.L. Huffaker, Nat. Commun. **4**, 1 (2013).

[31] P. Krogstrup, H.I. Jørgensen, M. Heiss, O. Demichel, J. V. Holm, M. Aagesen, J. Nygard, and A. Fontcuberta I Morral, Nat. Photonics **7**, 306 (2013).

[32] J. Wallentin, N. Anttu, D. Asoli, M. Huffman, I. Åberg, M.H. Magnusson, G. Siefer, P. Fuss-Kailuweit, F. Dimroth, B. Witzigmann, H.Q. Xu, L. Samuelson, K. Deppert, and M.T. Borgström, Science (80-.). **339**, 1057 (2013).

[33] M.A. Green, E.D. Dunlop, J. Hohl-Ebinger, M. Yoshita, N. Kopidakis, and X. Hao, Prog. Photovoltaics Res. Appl. **28**, 629 (2020).

[34] M. Yao, S. Cong, S. Arab, N. Huang, M.L. Povinelli, S.B. Cronin, P.D. Dapkus, and C. Zhou, Nano Lett. **15**, 7217 (2015).

[35] A. Standing, S. Assali, L. Gao, M.A. Verheijen, D. Van Dam, Y. Cui, P.H.L. Notten, J.E.M. Haverkort, and E.P.A.M. Bakkers, Nat. Commun. **6**, (2015).

[36] L. Gao, Y. Cui, J. Wang, A. Cavalli, A. Standing, T.T.T. Vu, M.A. Verheijen, J.E.M. Haverkort, E.P.A.M. Bakkers, and P.H.L. Notten, Nano Lett. **14**, 3715 (2014).

[37] M. De Luca, A. Polimeni, H.A. Fonseka, A.J. Meaney, P.C.M. Christianen, J.C. Maan, S. Paiman, H.H. Tan, F. Mura, C. Jagadish, and M. Capizzi, NANO Lett. **14**, 4250 (2014).

[38] A. Irrera, P. Artoni, F. Iacona, E.F. Pecora, G. Franzò, M. Galli, B. Fazio, S. Boninelli, and

F. Priolo, Nanotechnology **23**, (2012).

[39] M.Y. Swinkels, M.R. Van Delft, D.S. Oliveira, A. Cavalli, I. Zardo, R.W. Van Der Heijden, and E.P.A.M. Bakkers, Nanotechnology **26**, (2015).

[40] D. Li, Y. Wu, P. Kim, L. Shi, P. Yang, and A. Majumdar, Appl. Phys. Lett. **83**, 2934 (2003).

[41] L. Tsakalakos, J. Balch, J. Fronheiser, B.A. Korevaar, O. Sulima, and J. Rand, Appl. Phys. Lett. **91**, 233117 (2007).

[42] M.T. Borgstrom, J. Wallentin, M. Heurlin, S. Falt, P. Wickert, J. Leene, M.H. Magnusson, K. Deppert, and L. Samuelson, IEEE J. Sel. Top. QUANTUM Electron. **17**, 1050 (2011).

[43] X. Zhang, J. Qin, Y. Xue, P. Yu, B. Zhang, L. Wang, and R. Liu, Sci. Rep. **4**, 4596 (2014).

[44] D. Commandeur, J. McGuckin, and Q. Chen, Nanotechnology **31**, 265403 (2020).

[45] A. Galan Gonzalez, A.K. Sivan, J. Hernández Ferrer, L. Bowen, L. Di Mario, F. Martelli, A.M. Benito, W.K. Maser, M.U. Chaudhry, A. Gallant, D.A. Zeze, and D. Atkinson, ACS Appl. Nano Mater. (2020).

[46] F. Patolsky, G. Zheng, and C.M. Lieber, Anal. Chem. **78**, 4260 (2006).

[47] Y. Cui and C.M. Lieber, Science (80-.). **291**, 851 (2001).

[48] Y. Cui, X. Duan, J. Hu, and C.M. Lieber, J. Phys. Chem. B **104**, 5215 (2000).

[49] C. Thelander, M.T. Björk, M.W. Larsson, A.E. Hansen, L.R. Wallenberg, and L. Samuelson, Solid State Commun. **131**, 573 (2004).

[50] J. Shah, *Ultrafast Spectroscopy of Semiconductors and Semiconductor Nanostructures*, 2nd ed. (Springer-Verlag Berlin Heidelberg, 1999).

[51] Q.T. Vu, H. Haug, W.A. Hügel, S. Chatterjee, and M. Wegener, Phys. Rev. Lett. **85**, 3508 (2000).

[52] R. Huber, C. Kübler, S. Tübel, A. Leitenstorfer, Q.T. Vu, H. Haug, F. Köhler, and M.C. Amann, Phys. Rev. Lett. **94**, 027401 (2005).

[53] R.T. Ross and A.J. Nozik, J. Appl. Phys. **53**, 3813 (1982).

[54] M.B. Price, J. Butkus, T.C. Jellicoe, A. Sadhanala, A. Briane, J.E. Halpert, K. Broch, J.M. Hodgkiss, R.H. Friend, and F. Deschler, Nat. Commun. **6**, 1 (2015).

[55] C.K. Yong, J. Wong-Leung, H.J. Joyce, J. Lloyd-Hughes, Q. Gao, H.H. Tan, C. Jagadish, M.B. Johnston, and L.M. Herz, Nano Lett. **13**, 4280 (2013).

[56] H.M. Van Driel, Phys. Rev. B **19**, 5928 (1979).

[57] V. Klimov, P. Haring Bolivar, and H. Kurz, Phys. Rev. B **52**, 4728 (1995).

[58] D. Tedeschi, M. De Luca, H.A. Fonseka, Q. Gao, F. Mura, H.H. Tan, S. Rubini, F. Martelli, C. Jagadish, M. Capizzi, and A. Polimeni, Nano Lett. **16**, 3085 (2016).

[59] Gordon E. Moore, Electronics **38**, (1965).

[60] K. Masuko, M. Shigematsu, T. Hashiguchi, D. Fujishima, M. Kai, N. Yoshimura, T. Yamaguchi, Y. Ichihashi, T. Mishima, N. Matsubara, T. Yamanishi, T. Takahama, M. Taguchi, E. Maruyama, and S. Okamoto, IEEE J. Photovoltaics **4**, 1433 (2014).

[61] S. Rühle, Sol. Energy **130**, 139 (2016).

[62] W. Shockley and H.J. Queisser, J. Appl. Phys. **32**, 510 (1961).

[63] M. Maiuri, M. Garavelli, and G. Cerullo, J. Am. Chem. Soc. **142**, 3 (2020).

[64] K.E. Knowles, M.D. Koch, and J.L. Shelton, J. Mater. Chem. C **6**, 11853 (2018).

[65] S. Backus, C.G. Durfee, M.M. Murnane, and H.C. Kapteyn, Rev. Sci. Instrum. **69**, 1207 (1998).

[66] M. Fox, Optical Properties of Solids, Oxford University Press, USA, 2001, vol. 3.

[67] S. Nakamura, G. Fasol, S. Nakamura, and G. Fasol, in *Blue Laser Diode* (Springer Berlin Heidelberg, 1997), pp. 21–34.

[68] D. Vanmaekelbergh and L.K. Van Vugt, Nanoscale **3**, 2783 (2011).

[69] S.S. Iyer and Y.H. Xie, Science (80-.). **260**, 40 (1993).

[70] W.H.W. R. Merlin, A. Pinczuk, *Raman Scattering in Materials Science* (Springer-Verlag Berlin Heidelberg, 2000).

[71] B. Sukumar, *Crystalline Silicon: Properties and Uses* (2011).

[72] D. Thomson, A. Zilkie, J.E. Bowers, T. Komljenovic, G.T. Reed, L. Vivien, D. Marris-Morini, E. Cassan, L. Virot, J.M. Fédéli, J.M. Hartmann, J.H. Schmid, D.X. Xu, F. Boeuf, P. O'Brien, G.Z. Mashanovich, and M. Nedeljkovic, J. Opt. (United Kingdom) **18**, 073003 (2016).

[73] J.G. Wangüemert-Pérez, A. Hadij-ElHouati, A. Sánchez-Postigo, J. Leuermann, D.X. Xu, P. Cheben, A. Ortega-Moñux, R. Halir, and Í. Molina-Fernández, Opt. Laser Technol. **109**, 437 (2019).

[74] J. Liu, D.D. Cannon, K. Wada, Y. Ishikawa, S. Jongthammanurak, D.T. Danielson, J. Michel, and L.C. Kimerling, Appl. Phys. Lett. **87**, 011110 (2005).

[75] Z. Wang, J.E. Alaniz, W. Jang, J.E. Garay, and C. Dames, Nano Lett. **11**, 2206 (2011).

[76] M. Heiss, E. Russo-Averchi, A. Dalmau-Mallorquí, G. Tütüncüoğlu, F. Matteini, D. Rüffer, S. Conesa-Boj, O. Demichel, E. Alarcon-Lladó, and A. Fontcuberta i Morral, Nanotechnology **25**, 014015 (2014).

[77] J.P. Proot, C. Delerue, and G. Allan, Appl. Phys. Lett. **61**, 1948 (1992).

[78] P.M. Fauchet, Mater. Today **8**, 26 (2005).

[79] L. Tian, L. Di Mario, A.K. Sivan, D. Catone, P. O'Keeffe, A. Paladini, S. Turchini, and F. Martelli, Nanotechnology **30**, 1 (2019).

[80] Tian, Lin , Growth and Optical Properties of Semiconductor Nanowires, Universita degli studi di Roma, 2016.

[81] X. Zhao, C.M. Wei, L. Yang, and M.Y. Chou, Phys. Rev. Lett. **92**, 236805 (2004).

[82] D.D.D. Ma, C.S. Lee, F.C.K. Au, S.Y. Tong, and S.T. Lee, Science (80-.). **299**, 1874 (2003).

[83] K. Kimura, J. Clust. Sci. **10**, 359 (1999).

[84] V. Kuntermann, C. Cimpean, G. Brehm, G. Sauer, C. Kryschi, and H. Wiggers, (n.d.).

[85] Y. Kanemitsu, Phys. Rep. **263**, 1 (1995).

[86] D. Sangalli, S. Dal Conte, C. Manzoni, G. Cerullo, and A. Marini, Phys. Rev. B **93**, 195205 (2016).

[87] T. Ichibayashi, S. Tanaka, J. Kanasaki, K. Tanimura, and T. Fauster, Phys. Rev. B - Condens. Matter Mater. Phys. **84**, 235210 (2011).

[88] M. Schultze, K. Ramasesha, C.D. Pemmaraju, S.A. Sato, D. Whitmore, A. Gandman, J.S. Prell, L.J. Borja, D. Prendergast, K. Yabana, D.M. Neumark, and S.R. Leone, Science (80-.). **346**, 1348 (2014).

[89] H.J. Hovel, *Semiconductors and Semimetals. Volume 11. Solar Cells* (Academic Press, Inc.,New York, United States, 1975).

[90] D.E. Aspnes and A.A. Studna, Phys. Rev. B **27**, 985 (1983).

[91] S. Dal Conte, D. Sangalli, A. Marini, G. Cerullo, and C. Manzoni, in *Springer Proc. Phys.* (Springer Science and Business Media, LLC, 2015), pp. 230–232.

[92] M. Mattila, T. Hakkarainen, M. Mulot, and H. Lipsanen, Nanotechnology **17**, 1580 (2006).

[93] M. Murayama and T. Nakayama, Phys. Rev. B **49**, 4710 (1994).

[94] S. Perera, K. Pemasiri, M.A. Fickenscher, H.E. Jackson, L.M. Smith, J. Yarrison-Rice, S. Paiman, Q. Gao, H.H. Tan, and C. Jagadish, Appl. Phys. Lett. **97**, (2010).

[95] S. Perera, T. Shi, M.A. Fickenscher, H.E. Jackson, L.M. Smith, J.M. Yarrison-Rice, S. Paiman, Q. Gao, H.H. Tan, and C. Jagadish, Nano Lett. **13**, 5367 (2013).

[96] K. Pemasiri, S. Perera, Y. Wang, M. Montazeri, H. Jackson, L. Smith, J. Yarrison-Rice, Q. Gao, H. Tan, and C. Jagadish, in *Phys. Semicond.*, edited by Ihn, T and Rossler, C and Kozikov, A (2013), p. 476+.

[97] T. Akiyama, K. Sano, K. Nakamura, and T. Ito, JAPANESE J. Appl. Phys. PART 2-LETTERS EXPRESS Lett. **45**, L275 (2006).

[98] K.A. Dick, P. Caroff, J. Bolinsson, M.E. Messing, J. Johansson, K. Deppert, L.R. Wallenberg, and L. Samuelson, Semicond. Sci. Technol. **25**, (2010).

[99] H.J. Joyce, J. Wong-Leung, Q. Gao, H.H. Tan, and C. Jagadish, NANO Lett. **10**, 908 (2010).

[100] M. Heiss, S. Conesa-Boj, J. Ren, H.-H. Tseng, A. Gali, A. Rudolph, E. Uccelli, F. Peiró, J.R. Morante, D. Schuh, E. Reiger, E. Kaxiras, J. Arbiol, and A. Fontcuberta I Morral, Phys. Rev. B **83**, 45303 (2011).

[101] P. Caroff, J. Bolinsson, and J. Johansson, IEEE J. Sel. Top. Quantum Electron. **17**, 829 (2011).

[102] A. Belabbes, C. Panse, J. Furthmueller, and F. Bechstedt, Phys. Rev. B **86**, (2012).

[103] D.C. Reynolds, C.W. Litton, R.J. Almassy, S.B. Nam, P.J. Dean, and R.C. Clarke, Phys. Rev. B **13**, 2507 (1976).

[104] A. Mishra, L. V. Titova, T.B. Hoang, H.E. Jackson, L.M. Smith, J.M. Yarrison-Rice, Y. Kim, H.J. Joyce, Q. Gao, H.H. Tan, and C. Jagadish, Appl. Phys. Lett. **91**, 263104 (2007).

[105] A. Zilli, M. De Luca, D. Tedeschi, H.A. Fonseka, A. Miriametro, H.H. Tan, C. Jagadish, M. Capizzi, and A. Polimeni, ACS Nano **9**, 4277 (2015).

[106] P. Rochon and E. Fortin, Phys. Rev. B **12**, 5803 (1975).

[107] I. Vurgaftman, J.R. Meyer, and L.R. Ram-Mohan, J. Appl. Phys. **89**, 5815 (2001).

[108] A. De and C.E. Pryor, Phys. Rev. B **81**, (2010).

[109] J. Wallentin, K. Mergenthaler, M. Ek, L.R. Wallenberg, L. Samuelson, K. Deppert, M.-E. Pistol, and M.T. Borgstrom, NANO Lett. **11**, 2286 (2011).

[110] M.H. Hadj Alouane, N. Chauvin, H. Khmissi, K. Naji, B. Ilahi, H. Maaref, G. Patriarche, M. Gendry, and C. Bru-Chevallier, Nanotechnology **24**, 035704 (2013).

[111] G.L. Tuin, M.T. Borgström, J. Trägårdh, M. Ek, L.R. Wallenberg, L. Samuelson, and M.-E. Pistol, Nano Res **2011**, 159 (2011).

[112] E.G. Gadret, M.M. De Lima, J.R. Madureira, T. Chiaramonte, M.A. Cotta, F. Iikawa, and A. Cantarero, Appl. Phys. Lett. **102**, 122101 (2013).

[113] Y. Wang, H.E. Jackson, L.M. Smith, T. Burgess, S. Paiman, Q. Gao, H.H. Tan, and C. Jagadish, Nano Lett. **14**, 7153 (2014).

[114] S. Barman and G.P. Srivastava, Phys. Rev. B - Condens. Matter Mater. Phys. **69**, 235208 (2004).

[115] M. Achermann, A.P. Bartko, J.A. Hollingsworth, and V.I. Klimov, Nat. Phys. **2**, 557 (2006).

[116] S. Ambrosini, M. Fanetti, V. Grillo, A. Franciosi, and S. Rubini, AIP Adv. **1**, 042142 (2011).

[117] M. Garriga, M. Cardona, N.E. Christensen, P. Lautenschlager, T. Isu, and K. Ploog, Phys. Rev. B **36**, 3254 (1987).

[118] A. Lastras-Martínez, R.E. Balderas-Navarro, and L.F. Lastras-Martínez, Thin Solid Films **373**, 207 (2000).

[119] S. Loughin, R.H. French, L.K. De Noyer, W.Y. Ching, and Y.N. Xu, J. Phys. D. Appl. Phys. **29**, 1740 (1996).

[120] K.S. Burch, J. Stephens, R.K. Kawakami, D.D. Awschalom, and D.N. Basov, Phys. Rev. B - Condens. Matter Mater. Phys. **70**, 205208 (2004).

[121] P. Lautenschlager, M. Garriga, S. Logothetidis, and M. Cardona, Phys. Rev. B **35**, 9174 (1987).

[122] M.E. Pistol and X. Liu, Phys. Rev. B **45**, 4312 (1992).

[123] A.G. Thompson, M. Cardona, K.L. Shaklee, and J.C. Woolley, Phys. Rev. **146**, 601 (1966).

[124] R.J. Nelson, N. Holonyak, and W.O. Groves, Phys. Rev. B **13**, 5415 (1976).

[125] Y. Zhang, A.M. Sanchez, Y. Sun, J. Wu, M. Aagesen, S. Huo, D. Kim, P. Jurczak, X. Xu, and H. Liu, Nano Lett. **16**, 1237 (2016).

[126] O. Pagès, J. Souhabi, A. V. Postnikov, and A. Chafi, Phys. Rev. B - Condens. Matter Mater. Phys. **80**, 035204 (2009).

[127] D. Bohm and D. Pines, Phys. Rev. **82**, 625 (1951).

[128] K.L. Kelly, E. Coronado, L.L. Zhao, and G.C. Schatz, J. Phys. Chem. B **107**, 668 (2003).

[129] D.D. Evanoff and G. Chumanov, ChemPhysChem **6**, 1221 (2005).

[130] X. Huang, I.H. El-Sayed, W. Qian, and M.A. El-Sayed, J. Am. Chem. Soc. **128**, 2115 (2006).

[131] K.A. Willets and R.P. Van Duyne, Annu. Rev. Phys. Chem. **58**, 267 (2007).

[132] M.L. Brongersma, N.J. Halas, and P. Nordlander, Nat. Nanotechnol. **10**, 25 (2015).

[133] J. Li, S.K. Cushing, P. Zheng, F. Meng, D. Chu, and N. Wu, Nat. Commun. **4**, 1 (2013).

[134] S. Linic, P. Christopher, and D.B. Ingram, Nat. Mater. **10**, 911 (2011).

[135] M. Achermann, J. Phys. Chem. Lett. **1**, 2837 (2010).

[136] A.K. Sivan, L. Di Mario, D. Catone, P. O'Keeffe, S. Turchini, S. Rubini, and F. Martelli, Nanotechnology **31**, 174001 (2020).

[137] G. V. Hartland, Chem. Rev. **111**, 3858 (2011).

[138] Y. Zhang, S. He, W. Guo, Y. Hu, J. Huang, J.R. Mulcahy, and W.D. Wei, Chem. Rev. **118**, 2927 (2018).

[139] S.K. Cushing, J. Li, F. Meng, T.R. Senty, S. Suri, M. Zhi, M. Li, A.D. Bristow, and N. Wu, J. Am. Chem. Soc. **134**, 15033 (2012).

[140] X.C. Ma, Y. Dai, L. Yu, and B.B. Huang, Light Sci. Appl. **5**, e16017 (2016).

[141] J. Li, S.K. Cushing, F. Meng, T.R. Senty, A.D. Bristow, and N. Wu, Nat. Photonics **9**, 601 (2015).

[142] Y. Tian and T. Tatsuma, J. Am. Chem. Soc. **127**, 7632 (2005).

[143] C. Clavero, Nat. Photonics **8**, 95 (2014).

[144] L. Di Mario, Realization of Nanowire-Based Structures and Their Investigation by Optical and Electronic Spectroscopies, Universita degli Studi di Roma (2016).

[145] A. Convertino, M. Cuscunà, F. Martelli, M.G. Manera, and R. Rella, J. Phys. Chem. C **118**, 685 (2014).

[146] L. Di Mario, T.O. Otomalo, D. Catone, P. O'Keeffe, L. Tian, S. Turchini, B. Palpant, and F. Martelli, Phys. Rev. B **97**, 115448 (2018).

[147] V. Zannier, F. Martelli, V. Grillo, J.R. Plaisier, A. Lausi, and S. Rubini, Phys. Status Solidi - Rapid Res. Lett. **8**, 182 (2014).

[148] L. Tian, L. Di Mario, V. Zannier, D. Catone, S. Colonna, P. O'Keeffe, S. Turchini, N. Zema, S. Rubini, and F. Martelli, Phys. Rev. B **94**, 1 (2016).

[149] W.Y. Liang and A.D. Yoffe, Philos. Mag. A J. Theor. Exp. Appl. Phys. **16**, 1153 (1967).

[150] A. Saxena, Q. Pan, and H.E. Ruda, Nanotechnology **24**, (2013).

[151] D. Nesheva, M.J.ˇ S´cepanovi´c, S. Aškrabic, Z. Levi, I. Bineva, and Z. V Popovi´c, *Raman Scattering from ZnSe Nanolayers* (2009).

[152] Y. Jiang, X.-M. Meng, W.-C. Yiu, J. Liu, J.-X. Ding, C.-S. Lee, and S.-T. Lee, J. Phys. Chem. B **108**, 9, 2784–2787 (2004).

[153] S.K. Ghosh, S. Nath, S. Kundu, K. Esumi, and T. Pal, J. Phys. Chem. B **108**, 13963 (2004).

[154] T.P. White and K.R. Catchpole, Appl. Phys. Lett. **101**, 073905 (2012).

[155] M. Schnippering, M. Carrara, A. Foelske, R. Kötz, and D.J. Fermín, Phys. Chem. Chem. Phys. **9**, 725 (2007).

[156] M. Vos, F. Xu, S.G. Anderson, J.H. Weaver, and H. Cheng, Phys. Rev. B **39**, 10744 (1989).

[157] W.F. Krolikowski and W.E. Spicer, Phys. Rev. B **1**, 478 (1970).

[158] C.Y. Fong, J.P. Walter, and M.L. Cohen, Phys. Rev. B **11**, 2759 (1975).

[159] B.K. Meyer, H. Alves, D.M. Hofmann, W. Kriegseis, D. Forster, F. Bertram, J. Christen, A. Hoffmann, M. Straßburg, M. Dworzak, U. Haboeck, and A. V. Rodina, Phys. Status Solidi Basic Res. **241**, 231 (2004).

[160] Reynolds D. C., Look D. C., Jogai B., Litton C. W., G. Cantwell, W.C. Harsch, and B. Jogai, Phys. Rev. B - Condens. Matter Mater. Phys. **60**, 2340 (1999).

[161] D.G. Thomas, J. Phys. Chem. Solids **15**, 86 (1960).

[162] Z.L. Wang, J. Phys. Condens. Matter **16**, R829 (2004).

[163] A. Janotti and C.G. Van de Walle, Reports Prog. Phys. **72**, 126501 (2009).

[164] J. Kegel, I.M. Povey, and M.E. Pemble, Nano Energy **54**, 409 (2018).

[165] J.M.D. Coey, M. Venkatesan, and C.B. Fitzgerald, Nat. Mater. **4**, (2005).

[166] P. Gopal and N.A. Spaldin, Phys. Rev. B - Condens. Matter Mater. Phys. **74**, 094418 (2006).

[167] M. Wang, F. Ren, G. Cai, Y. Liu, S. Shen, and L. Guo, Nano Res. **7**, 353 (2014).

[168] P.S. Xu, Y.M. Sun, C.S. Shi, F.Q. Xu, and H.B. Pan, Nucl. Instrum. Meth. B, **199**, 286–290 (2003).

[169] K.J. Kim and Y.R. Park, Appl. Phys. Lett. **81**, 1420 (2002).

[170] Y.R. Lee, A.K. Ramdas, and R.L. Aggarwal, Phys. Rev. B **38**, 10600 (1988).

[171] A. Galan-Gonzalez, A. Gallant, D.A. Zeze, and D. Atkinson, Nanotechnology **30**, 305602 (2019).

[172] X. Li, S. Liu, K. Fan, Z. Liu, B. Song, and J. Yu, Adv. Energy Mater. **8**, 1800101 (2018).

[173] W.W. Zhan, Q. Kuang, J.Z. Zhou, X.J. Kong, Z.X. Xie, and L.S. Zheng, J. Am. Chem. Soc. **135**, 1926 (2013).

[174] A. Janotti and C.G. Van De Walle, Appl. Phys. Lett. **87**, 1 (2005).

[175] M.D. McCluskey and S.J. Jokela, J. Appl. Phys. **106**, (2009).

[176] B. Ullrich, A.K. Singh, M. Bhowmick, P. Barik, D. Ariza-Flores, H. Xi, and J.W. Tomm, AIP Adv. **4**, 123001 (2014).

[177] F. de la Peña, E. Prestat, V.T. Fauske, P. Burdet, P. Jokubauskas, M. Nord, T. Ostasevicius, K.E. MacArthur, M. Sarahan, D.N. Johnstone, J. Taillon, J. Lähnemann, V. Migunov, A. Eljarrat, J. Caron, T. Aarholt, S. Mazzucco, M. Walls, T. Slater, F. Winkler, pquinn-dls, B. Martineau, G. Donval, R. McLeod, E.R. Hoglund, I. Alxneit, D. Lundeby, T. Henninen, L.F. Zagonel, and A. Garmannslund, Zenodo (2019).

[178] C. Bauer, G. Boschloo, E. Mukhtar, and A. Hagfeldt, Chem. Phys. Lett. **387**, 176 (2004).

[179] S.W. Jung, W.I. Park, H.D. Cheong, G.C. Yi, H.M. Jang, S. Hong, and T. Joo, Appl. Phys. Lett. **80**, 1924 (2002).

[180] A. Janotti and C.G. de Walle, Phys. Rev. B **76**, 165202 (2007).

[181] L.S. Vlasenko and G.D. Watkins, Phys. Rev. B, **71**, 125210 (2005).

[182] B. Pal and P.K. Giri, J. Appl. Phys. **108**, 084322 (2010).

[183] X. Liu, X. Wu, H. Cao, and R.P.H. Chang, J. Appl. Phys. **95**, 3141 (2004).

[184] B.D. Yuhas, D.O. Zitoun, P.J. Pauzauskie, R. He, and P. Yang, Angew. Chemie Int. Ed. **45**, 420 (2006).

[185] P. Koidl, Phys. Rev. B **15**, 2493 (1977).

[186] Y. Caglar, J. Alloys Compd. **560**, 181 (2013).

[187] Y. Liu, Q. Fang, M. Wu, Y. Li, Q. Lv, J. Zhou, and B. Wang, J. Phys. D. Appl. Phys. **40**, 4592 (2007).

[188] J. Wang, Z. Wang, B. Huang, Y. Ma, Y. Liu, X. Qin, X. Zhang, and Y. Dai, ACS Appl. Mater. Interfaces **4**, 4024 (2012).

[189] S. Basu, D. Y. Inamdar, S. Mahamuni, A. Chakrabarti, C. Kamal, G. Ravi Kumar, S. N. Jha, and D. Bhattacharyya, J. Phys. Chem. C **118**, 9154 (2014).

[190] Y. Zheng, C. Chen, Y. Zhan, X. Lin, Q. Zheng, K. Wei, J. Zhu, and Y. Zhu, Inorg. Chem. **46**, 6675 (2007).

[191] X. Long, F. Li, L. Gao, Y. Hu, H. Hu, J. Jin, and J. Ma, ChemSusChem **11**, 4094 (2018).

[192] P. Li, J. Li, X. Feng, J. Li, Y. Hao, J. Zhang, H. Wang, A. Yin, J. Zhou, X. Ma, and B. Wang, Nat. Commun. **10**, 1 (2019).